Development of Physical Models for the Simulation of Optical Properties of Solar Cell Modules

Von der Fakultät für Mathematik und Physik
der Gottfried Wilhelm Leibniz Universität Hannover
zur Erlangung des Grades

Doktor der Naturwissenschaften
Dr. rer. nat.

genehmigte Dissertation

von

M. Sc. Malte Ruben Vogt

geboren am 07.11.1986, in Langenhagen

2015

Abstract

More than 5% of the electrical power in Germany were gained by photovoltaic energy conversion for the first time in 2013. Consequently, solar energy research now focuses on improving not only the cells but also the solar cell modules.

The experimental part of this thesis develops methods for measuring the optical properties of materials used in solar cell modules. A Monte-Carlo analysis is developed as a tool for quantifying measurement uncertainties of spectroscopic ellipsometry data. This method is utilized to systematically determine the optical properties of the most commonly used PV module components more specifically or, in case of new materials such as UV transmitting EVA, for the first time. The results are tabulated in the appendix B.

Special emphasis is given on characterizing the extinction coefficient k of soda-lime glass in dependence of iron content nearly two orders of magnitude lower than found in literature but widely used in the industry. Moreover, a semi-empirical model is developed for the extinction coefficient of soda-lime glasses as a function of iron content and wavelength.

Reflection measurements of back sheets of PV modules, which are covered with an EVA layer, as is the case in the module, are conducted. The reflectivity at such an EVA/back sheet interface turns out to be higher than at the traditionally measured air/back sheet interface.

In the simulation part, ray tracing is extended and utilized to predict the performance of various solar cell modules at standardized testing conditions (STC). The measurements obtained in the first part of this thesis are used as input. The results for a typical reference module, producing 290.6 W electrical power output, reveal that the module is improved by 2 W due to UV transmitting EVA, 8 W due to the white back sheet and 5 W due to the antireflection coating on the fron glass. Module output power declines between 4 W, for an iron content in the front glass equivalent to $0.1‰$ Fe_2O_3, and 40 W for $1‰$ Fe_2O_3.

The optical loss analysis conducted in this thesis predicts that the components with the biggest potential for future efficiency gain are: the front glass and its ARC; the back sheet; the front side metallization; and the cell's rear side reflectivity.

The cell's rear side reflectivity may be improved by plasmonic nanoparticles, whose scattering angles are investigated by solving the Maxwell equations with a finite-element model (FEM) aproach.

However, module power output in the field is lower than at STC due to the elevated operating temperatures influencing the semiconductor properties. Consequently, a new FEM model is developed that solves the thermal equations coupled with the semiconductor equations.This simulation model reproduces the measurement data from an outdoor module test very well.

This simulation model reveals that replacing the full rear side metalization with a SiN_x mirror lowers the module operating temperature by 3°C, which is equivalent to an 5 W increase in output power. These results demonstrate that it is advantageous to take the module's thermal properties into account when optimizing solar cells modules.

Key words: Simulation of PV modules; PV module optical properties; Soda-lime glass;

Kurzzusammenfassung

Im Jahr 2013 wurde erstmals mehr als 5% des elektrischen Stroms in Deutschland aus Solarenergie gewonnen. Daher fokussiert sich die Solarenergieforschung nun vermehrt darauf, nicht nur die Zelle, sondern auch die Module zu optimieren.

Im experimentellen Teil dieser Arbeit werden Messmethoden entwickelt, welche die optischen Eigenschaften von PV-Modulen genauer bestimmen. Um die Messunsicherheit von spektral aufgelöster Ellipsometrie zu quantifizieren, wird eine auf der Monte-Carlo-Simulation basierende Datenanalysemethode entwickelt. Diese Methode wird eingesetzt, um die komplexen Brechungsindizes der Solarmodulkomponenten genauer - oder im Fall von UV-transmittierendem EVA erstmalig - zu bestimmen. Die Ergebnisse finden sich als Tabellen im Anhang B.

Der Extinktionskoeffizient und der Eisengehalt von eisenarmem Kalk-Natron-Glas werden erstmals für ein und demselben Probensatz gemessen. Darauf aufbauend wird ein semi-empirisches Modell entwickelt, welches den Extinktionskoeffizienten dieser Gläser als Funktion von Eisengehalt und Wellenlänge bestimmt.

Reflexionsmessungen von mit EVA beschichteten Rückseitenfolien werden erstmalig so ausgewertet, dass die höhere Reflektivität dieser Grenzschicht bestimmt wird.

Im Simulationsteil wird die geometrische Strahlenverfolgung auf PV-Modulebene erweitert und genutzt, um die elektrische Leistung kompletter Solarmodule bei Standardtestbedingungen (STC) zu berechnen. Als Referenz wird so an einem Hochleistungsmodul mit 290.6 W elektrischer Leistung exemplarisch gezeigt, dass das UV-transmittierende EVA für 2 W, die Glasantireflexschicht für 5 W und die Rückseitenfolie für 8 W Leistungserhöhung bei STC verantwortlich sind.

Die Verlustanalyse ergibt, dass die größten Verbesserungspotentiale bei der Reduktion von Absorption im Glas sowie Reflexion am Glas und der Vorderseitenmetallisierung und der Verbesserung der Reflexionseigenschaften von Rückseitenfolie und Zellrückseite liegen.

Darauf aufbauend wird mit einem auf der Finite-Elemente-Methode basierendem Modell die Streucharakteristik von Plasmonischen Nanopartikeln an der Zellrückseite untersucht.

Ungekühlt im Feld erreichen Solarmodule aufgrund der Temperaturabhängigkeit der Halbleitereigenschaften und Betriebstemperaturen von 50°C und höher praktisch nie ihre STC-Leistung. Um dies zu untersuchen, wird ein weiteres Modell entwickelt, welches die Halbleitergleichungen gekoppelt mit den thermischen Gleichungen löst. Dieses Simulationsmodell reproduziert Messungen von Solarmodulen im Feld mit hoher Genauigkeit. Zusätzlich ermöglicht es Vorhersagen, dass bestimmte Zell- und Modultypen etwas kühlere Betriebstemperaturen und dadurch einen höheren Ertrag im Feld haben werden. Dies zeigt, wie vorteilhaft es ist, nicht nur wie herkömmlich bei Raumtemperatur zu untersuchen, sondern auch die thermischen Eigenschaften zu beachten.

Schlagwörter: Simulation von PV-Modulen; Optische Eigenschaften von PV-Modulen; Kalk-Natron-Glas;

Contents

CHAPTER 1

Introduction

The solar cell "may mark the beginning of a new era, leading eventually to the realization of one of mankind's most cherished dreams-the harnessing of the almost limitless energy of the sun for the uses of civilization" was a commentary in the New York Times on April 26th, 1954. This was in reaction to scientists Daryl Chaplin, Calvin Fuller and Gerald Pearson presenting a new type of silicon solar cell powering a radio transmitter and a toy ferris wheel on the day before [Bel].

This cell converted the energy from sun light to electricity with an efficiency of about $\eta = 6\%$ [Bel]. Since 1954 cell efficiency has steadily increased due to research and technical development. Today the most efficient solar cell produced in the laboratory has an efficiency of 46% [Soi14]. However, there are many different types of solar cells and each has their own world record [NRE15]. For example, the most efficient non-concentrator cell on a silicon wafer has reached 25.6% [Mas14]. This is especially relevant since more than 90% of all produced solar cells are still silicon wafer based [ISE14].

In recent years solar energy has become economically and socially relevant. In 2013 more than 5% of the electrical power in Germany was produced by solar energy [ISE14] and world wide there is a capacity of photovoltaic energy production of 134 GWp per year [ISE14]. Solar cell based electricity production has had an experience curve of about 20% over the last 30 years. Hence, it is expected to become more important in the future.

As solar energy becomes more widely used, it is paramount to better understand the light interaction within the solar cell module (Sec. 1.1). While the optical properties of some module components have already been characterized [Mci09; Rub85] others such as UV transparent ethylene vinyl acetate (EVA) or the back sheet materials are still unknown. Moreover, until recently [Hol13] ray tracers were not capable to handle the ray tracing of an entire photovoltaic module.

This work aims to fill gaps in both the experimental determination of the optical properties of module materials and in the simulation of entire silicon wafer based modules.

In the experimental part I data analysis methods are developed to determine the refractive index of materials more accurately. Moreover, a method to determine the reflectivity of a diffuse reflector covered with another medium is developed. Those methods help to systematically determine the optical properties of the most commonly used photovoltaic (PV) module components.

In the simulation part II geometric ray tracing is utilized to predict a solar cell module's performance in standardized testing conditions (STC) on the basis of the material measurements. Additionally, the Finite-Element-Method (FEM) is applied to characterize the angular scattering distribution of plasmonic nanoparticles, which have the ability to improve the near infrared (NIR) collection efficiency of the next generation of solar cells.

Finally, another FEM based model solving self-concistently the thermal equations coupled with the semiconductor equations is introduced. This numerical model predicts the performance of PV modules in the field and is in good agreement with measurements from the field. Moreover, the model makes it possible to recognize effects conventional simulations with a fixed temperature do not detect. Predictions on how to further improve solar cell modules in the field are made based on this model.

1.1 Components of a typical solar cell module

A typical industrial type silicon wafer based solar cell module consists of the following layers shown in Fig. 1.1, listed from top to bottom:

- Soda-lime float **glass** with low iron content and a thickness between 3.2 mm and 4 mm as well as an area of 1.6 m × 1 m. Some of the glasses are covered with an anti-reflective coating (ARC) on top.

- The **module front encapsulant material** laminated between the glass and the cells top side. The most commonly used material is ethylene vinyl acetate (EVA) with a thickness around 450 µm.

- The **front side metallization** consists of typically around 85 fingers, three busbars and cell interconnectors.

- The **cell's ARC** typically is silicon nitride SiN_x, which also serves as a passivation layer to reduce surface recombination.

- There are typically 10 × 6 **cells** assembled in series in a module. They are made from a 156 mm × 156 mm wafer with a thickness of about 170 µm. Sometimes, the wafers have a pseudo squared shape resulting in an area of about 239.7 cm^2 each. Mono crystalline wafers have a top side with a texture of random pyramids, while multi crystalline wafers have an isotextured surface.

- A **rear side reflector** is at the bottom of the cell. In most industrial cells this is realized via a full area rear side aluminium metallization serving as both reflector and rear contact.
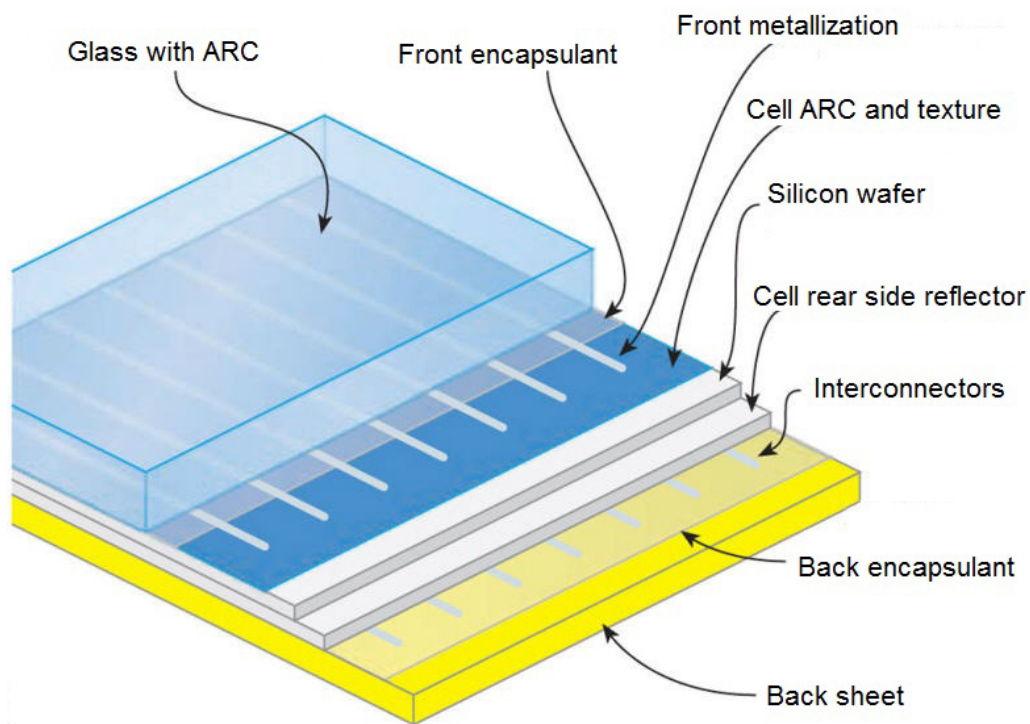
Figure 1.1: Layers of a typical industrial type solar cell module (this illustration is taken from [Pvm]). Please note that the material dimensions are not to scale.

- Mostly, the **module back encapsulant material** laminated between the cells and the back sheet is the same as at the front of the cells.

- The **back sheet** serves as a diffuse reflector, while covering the rear side of the module with a protective layer.

The description above is the most widely used module set-up, which will be assumed in this work unless specified otherwise.

PART I

Optical Measurements

CHAPTER 2

Measurement theory and methods

In order to accurately describe the interaction between a soler cell module and the incoming light one needs to know the geometry of the module, as well as each material's refractive index $\hat{n}(\lambda)$ in the relevant wavelength λ range:

$$\hat{n}(\lambda) = n(\lambda) - ik(\lambda), \tag{2.1}$$

which consists of the real part $n(\lambda)$ and the imaginary part or extinction coefficient $k(\lambda)$. Both parts are related to each other via the Kramers-Kronig relations, which state that $n(\lambda)$ at one wavelength depends on $k(\lambda)$ integrated over all wavelengths, and vice versa.

The extinction coefficient $k(\lambda)$ is directly proportional to the absorption coefficient $\alpha(\lambda)$ via [Bor99, Sec. 4.11]

$$\alpha(\lambda) = 4\pi \frac{k(\lambda)}{\lambda}. \tag{2.2}$$

Both characterize a material's ability to absorb light: $\alpha(\lambda)$ in respect to depth x, hence it has dimension 1/length; k in respect to λ, hence it is dimensionless.

While the imaginary part governs the absorption within a medium, the interaction at the interface between two media with $\hat{n}_1$ and $\hat{n}_2$ is determined according to the Fresnell theory by both parts of the refractive index and the angle of incidence as well as the light's polarization. The interface between two media is assumed to be infinitesimally thin and non-absorbing. The Fresnel equations [Mac01, Ch. 2] describe the interaction at the interface mathematically. A more detailed description of these equations can be found in German in my masters thesis [Vog11]. A more general discussion can be found in standard literature e.g. [Bor99; Mac01].

Knowing an anti-reflective-coating's (ARC) $\hat{n}(\lambda)$ is sufficient (together with its thickness and the light's properties) to describe the results of interference in an ARC during ray tracing [Mac01, Ch. 4].

Only in the case of scattering, $\hat{n}(\lambda)$ is insufficient for describing a PV module component's optical behavior, since information on the direction in which light is scattered, is required. Techniques for characterizing scattering will be discussed in section 2.2.5.

This chapter introduces the measurement and data analysis methods used to determine $\hat{n}(\lambda)$. For clarity, wavelength dependencies will often be omitted in the following.

2.1 Spectroscopic ellipsometry

Ellipsometry measures the change of polarization of light after oblique reflection (or transmission) at a sample. More specifically, it measures the ratio of amplitudes Ψ and the phase difference Δ between s- and p-polarized light [Fuj03; Tom05; Woo10]. The pair Ψ and Δ depends sensitively on $\hat{n}$, or in terms of Fresnel theory and its amplitudes r_p and r_s, there holds:

$$\frac{r_p(\theta_0)}{r_s(\theta_0)} = \tan\left(\Psi(\theta_0)\right) e^{i\Delta(\theta_0)} \tag{2.3}$$

where i is the imaginary number and θ_0 the angle of incidence. For the simplest case in which just the reflection at one interface is measured one can directly use the Fresnel equations [Fuj03, Ch. 5]:

$$\frac{r_p(\theta_0)}{r_s(\theta_0)} = \left(\frac{\hat{n}_1/\cos(\theta_1) - \hat{n}_0/\cos(\theta_0)}{\hat{n}_1/\cos(\theta_1) + \hat{n}_0/\cos(\theta_0)}\right) \Big/ \left(\frac{\hat{n}_0\cos(\theta_0) - \hat{n}_1\cos(\theta_1)}{\hat{n}_0\cos(\theta_0) + \hat{n}_1\cos(\theta_1)}\right), \tag{2.4}$$

where $\theta_1 = \arcsin\left(\hat{n}_0/\hat{n}_1 \sin(\theta_0)\right)$ is the refraction angle. For materials which transmit a significant fraction of light ($n >> k$) one can see (using Eq. 2.1) that ellipsometry is more sensitive to n than to k. To compensate for this, ellipsometry measurements are often combined with transmission measurements, which depend more sensitively on k.

The amount of light a sample transmits $I(\lambda, x)$, when light travels a distance $x = d$ within the sample with $\alpha(\lambda)$, can be calculated with the Lambert-Beer law [Bor99, Sec. 4.11]:

$$I(\lambda, d) = e^{-\alpha(\lambda)d}. \tag{2.5}$$

where the absorption coefficient α can be converted to k via Eq. 2.2. In subsection 2.1.2 it will be explained how a data analysis can be used to extract the complex refractive index from a series of different measurements via fitting techniques.

In practice, the sample often consists of various layers, and a model containing the layer structure needs to be employed to convert Ψ and Δ into $\hat{n}$ of each layer. In that case, more assumptions are made, and more uncertainties arise.

Moreover, ellipsometry is applied over many wavelengths, called spectral or spectroscopic ellipsometry. As both n and k are measured, often the Kramer-Kronig relations are used in the data evaluation of Ψ and Δ, where assumptions on $\hat{n}$ outside of the measured wavelength range are made.

For these reasons, ellipsometry involves a great deal of data evaluation procedures and is not as straight-forward as its simple measurement principle may suggest.

In the following the focus is on the details specific to the measurements described in this work; a general discussion of ellipsometry and data analysis can be found in the literature such as [Fuj03; Tom05; Woo10].

2.1.1 The spectroscopic ellipsometer

The spectroscopic ellipsometry and transmission measurements are conducted here with the commercially available Woollam M-2000UI rotating compensator ellipsometer (RCE) [Woo10]. The RCE is a ellipsometry configuration which was first introduced by [Hau75] and is illustrated in Fig. 2.1.
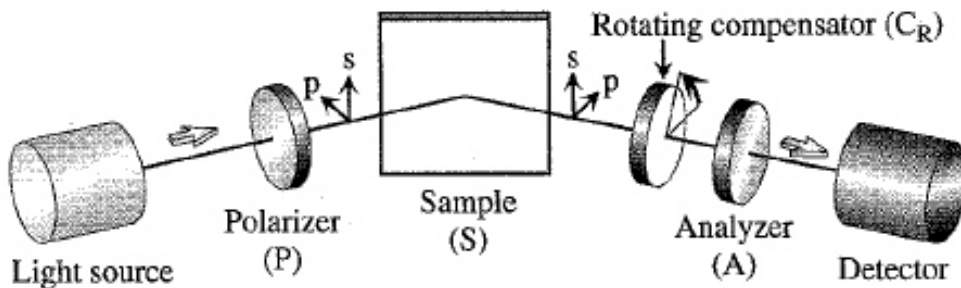
Figure 2.1: The Woollam M-2000UI rotating compensator ellipsometer configuration (the illustration is taken from [Fuj03, p. 88]). It consists of a lights source, a polarizer, the sample, a rotating compensator (which is a retarder), an analyzer (for determining the polarization of the reflected light), and a detector of light intensity.

This ellipsometry configuration consists of a light source, a polarizer, the sample, a rotating compensator (which is a retarder), an analyzer (for determining the polarization of the light) and a detector of light intensity. The advantage of the RCE-configuration is that it can measure Δ over the complete range from [0°-360°], which simpler setups (such as rotating polarizer ellipsometer or rotating analyzer ellipsometer) can only do from [0°-180°] [Fuj03, Ch. 4].

To control the ellipsometry measurement the WVASE32 software from the manufacturer is used. The wavelength range of the measurements performed here is between 250 nm and 1690 nm, switching from a silicon CCD-detector to an InGaAs detector at 970 nm. The light source is a halogen lamp. The Woollam M-2000UI measures at 583 different wavelengths, the silicon CCD measures every 1.6 nm while the InGaAs detector measures every 6.1 nm. Typically, the ellipsometry measurements are conducted for three different angles of incidence ($\theta_0 = 50°, 60°, 70°$), but this may sometimes vary for sample specific reasons (and will be mentioned in the discussion of the results). For each measured wavelength, several measurement values are obtained (one from transmission and two for each ellipsometry angle). Each value x_{exp} is an average from 250 rotation cycles of the compensator. WVASE32 determines the measurement uncertainty $u(x_{\mathrm{exp}})$ as interval

around x_{exp}, that includes 90% of the 250 single measurements from each compensator rotation.

2.1.2 Data analysis

For data acquisition and analysis, the Wvase32 software from the manufacturer is used. As mentioned above, the results of ellipsometry measurements are Ψ and Δ, and are evaluated here with the modeling and model verification process illustrated in Fig. 2.2.
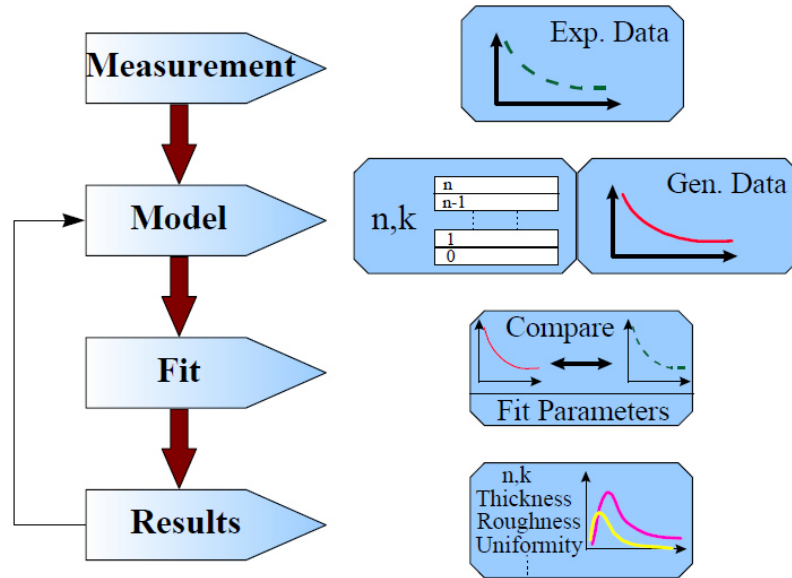
Figure 2.2: Since ellipsometry measures Ψ and Δ, one has to use a model to determine the optical constants of the sample. If a model can accurately explain Ψ and Δ, then it can be used to extract the samples optical properties as results. Often multiple steps of fitting and improving the model are necessary (this illustration is taken from [Woo10, Sec. 2.3]).

After the measurement the first step in data analysis is to construct a model describing the sample as a stack of layers with different optical properties. Each layer is characterized by a thickness d and a complex refractive index $\hat{n}$. In WVASE32 the model can consist of up to one incoherent substrate layer and as many coherent layers as needed. In a so called coherent layer the layer's thickness d is smaller than the length over which the light's phase is coherent. Thus interference effects occur and are considered in the calculation of the layer's optical properties. In the incoherent layer no interference effects are considered, because the layer thickness is assumed to be bigger than the length over which the light phase is coherent. The incoherent layer is typically used to describe a bulk material, while the coherent layers are used for thin-film surface layers such as oxides or anti-reflection-coatings (ARCs).

The WVASE32 then calculates the model specific $\Psi_{\mathrm{mod}}(\lambda_i, \theta_j, \vec{p})$, $\Delta_{\mathrm{mod}}(\lambda_i, \theta_j, \vec{p})$ and if needed $\tau_{\mathrm{mod}}(\lambda_i, 0°, \vec{p})$, where λ_i is the wavelength , θ_j is the angle of incidence, and $\tau_{\mathrm{mod}}(\lambda_i, 0°, \vec{p})$ the calculated transmission through the sample. Additionally $\vec{p}$ consists of

all layers thickness, refractive indexes (and parameters of other physical properties included in the model) which are open for fitting and not assumed to have a set value. Then a fit is used to find the best agreement between the measured values of $\Psi_{\mathrm{exp}}(\lambda_i, \theta_j)$, $\Delta_{\mathrm{exp}}(\lambda_i, \theta_j)$ and, if measured, $\tau_{\mathrm{exp}}(\lambda_i, 0°)$ and the modeled values by varying the fit parameters $\vec{p}$. The different methods used for the fitting are described in the following subsections.

If the fit between measurement and model is satisfactory, the layer's optical properties (e. g. thickness d and a complex refractive index $\hat{n}$) can be extracted from the model. For indicators of fit accuracy see the fitting procedures in the following subsections. If the user is not satisfied by the accuracy of the fit, the model is adapted and the fitting process is started again. Please note that more plausible results can be achieved, if the properties of only a single layer are determined (fitted) per measurement.

Wavelength by wavelength fit

The most basic fit approach is to fit one measured wavelength at a time, referred to as wavelength-by-wavelength-fit. The Levenberg-Marquardt algorithm [Pre92, Ch. 15.5] is used to minimize the following figure of merit $\chi^2(\lambda_i)$

$$\chi^2(\lambda_i) = \sum_{j=1}^{N} \left(\frac{\frac{(\Psi_{\mathrm{exp}}(\lambda_i,\theta_j) - \Psi_{\mathrm{mod}}(\lambda_i,\theta_j,\vec{p_i}))^2}{u^2(\Psi_{\mathrm{exp}}(\lambda_i,\theta_j))} + \frac{(\Delta_{\mathrm{exp}}(\lambda_i,\theta_j) - \Delta_{\mathrm{mod}}(\lambda_i,\theta_j,\vec{p_i}))^2}{u^2(\Delta_{\mathrm{exp}}(\lambda_i,\theta_j))}}{2N - P} \right), \qquad (2.6)$$

for each wavelength λ_i, where $u(x_{\mathrm{exp}})$ is the uncertainty of the measured value x_{exp}, N is the number of measured angles of incidence θ_j and P is the number of fit parameters in $\vec{p_i}$. In this work P usually equals two because the intension is often to determine a tabulated list of $n(\lambda_i)$ and $k(\lambda_i)$.

The main advantages of this method are that it converts the measurement very directly into refractive data and that it is not time consuming. The main disadvantage is that it does not necessarily satisfy the Kramers-Kronig relations, which relate n and k on a fundamental base, and also that it does not result in a continuous function of the wavelength, which most material have, but in a scattered set of data points.

Function fit

In the model- or function-fit, a mathematical function (dependent on global parameters) is fitted to measured data considering all wavelengths at once. Such a function consists of a sum of oscillators whose superposition is describing the refractive index $\hat{n}(\lambda)$ function. An overview of all the different types of oscillators implemented in the WVASE32 software can be found in [Woo10, Ch. 8]. The function-fit also uses the Levenberg-Marquardt algorithm [Pre92, Ch. 15.5] to minimize a different figure of merit the MSE:

$$\mathrm{MSE} = \sum_{i=1}^{M} \sum_{j=1}^{N} \left(\frac{\frac{(\Psi_{\mathrm{exp}}(\lambda_i,\theta_j) - \Psi_{\mathrm{mod}}(\lambda_i,\theta_j,\vec{p}))^2}{u^2(\Psi_{\mathrm{exp}}(\lambda_i,\theta_j))} + \frac{(\Delta_{\mathrm{exp}}(\lambda_i,\theta_j) - \Delta_{\mathrm{mod}}(\lambda_i,\theta_j,\vec{p}))^2}{u^2(\Delta_{\mathrm{exp}}(\lambda_i,\theta_j))}}{2NM - P} \right), \qquad (2.7)$$

for the whole wavelength range at once. Here, M is the number of wavelengths λ_i measured and $\vec{p}$ includes the parameters of the different oscillators. A MSE$>>$ 1 indicates that the model does not agree with the measured data, while MSE$\approx$ 1 indicates that the model describes the measurement well. Please note that MSE$\approx$ 1 does not necessarily indicate that the model is correct.

The advantages of the function-fit is that it produces a continuous refractive index function $\hat{n}(\lambda)$ that satisfies the Kramers-Kronig relations. The draw back of the function-fit is the uncertainty in the choice of the oscillators. For example, the oscillators may be chosen at the peaks of $n(\lambda)$ and $k(\lambda)$, but if there are no pronounced peaks, the oscillators must be chosen outside the measurement range, particularly in the UV.

Monte Carlo based data analysis

The wavelength-by-wavelength-fit in the WVase32 software does not show the uncertainty of the fitted parameters. Additionally the function fit only provides the uncertainties in terms of the global parameters used in the fit, which do not necessarily resemble the uncertainty of $\hat{n}(\lambda)$ at each wavelength. Therefore a data analysis technique according to the Guide to the Expression of Uncertainty in Measurement (GUM) [Joi08] is developed.

The GUM suggests that a numerical approach for calculating the uncertainty of the $\hat{n}(\lambda)$ data is most suitable, because a fitting procedure is used to calculate them. The numerical approach has the advantage that there is no need to find an analytical relationship between the measurement parameters and $n(\lambda)$ or $k(\lambda)$.

The averaging over 250 measurement cycles gives an uncertainty interval for each measured value. Assuming a normal distribution of values within those intervals, then the Monte Carlo method is used to generate a new set of random values within those intervals [Pre92, Ch. 7]. To account for the uncertainty in the angle of incidence, the Monte Carlo method is also used to vary the angle of incidence θ_j by up to $\pm 0.02°$ globally for all N values of j and by up to $\pm 0.01°$ in each θ_j individually.

This set of values is then loaded into the used data analysis set-up as new measurement data and fitted using the wavelength-by-wavelength-fit method, as described two sections above, resulting in new $n(\lambda_i)$ and $k(\lambda_i)$ values. Then a new set of values is generated and the process is repeated for the desired number of iterations. From all $n(\lambda_i)$ and $k(\lambda_i)$ values of each wavelength and all iterations, the average and the standard deviation are calculated. According to the GUM the average represents the value and the standard deviation represents the uncertainty of the value.

The Monte Carlo approach is not implemented in the Wvase32 software, it is realized in Excel, then the data is loaded into Wvase32, run in an automated fashion using AutoIt, the new $n(\lambda_i)$ and $k(\lambda_i)$ values are exported back into Excel, etc. In a test running 10000 iterations for one sample, it was determined that 1000 iterations offer a good compromise between accuracy and processing time. This process typically takes about 10 hours for 1000 iterations. Therefore it is only applied to some of the samples measured in Ch. 3. This

Monte Carlo based method for ellipsometry data analysis was newly developed together with C. Schinke [Sch15; Vog15b].

2.2 Reflection and Transmission measurements

The reflection measurements and some of the transmission measurements are carried out with a commercially available Varian Cary 5000 two-channel spectrophotometer (some other transmission measurements were conducted with the Woollam M2000UI spectroscopic ellipsometer in transmission set-up [Woo10]). The Cary is equipped with an integrating sphere. The reflection and transmission measurements of this instrument cover a spectral range from 250 nm to 2500 nm.
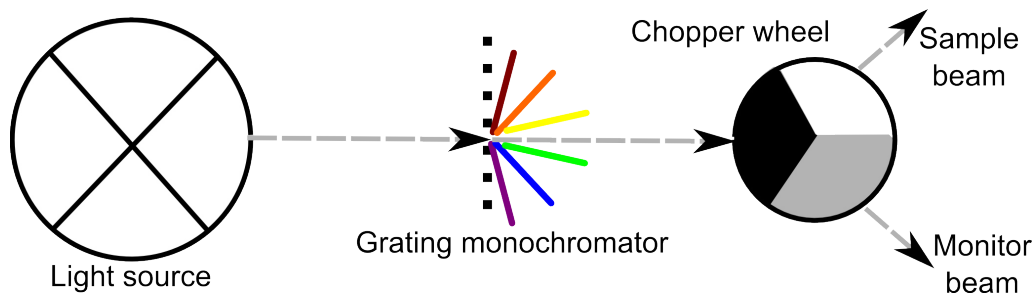
Figure 2.3: The monochromatic light beam preparation for both channels of the Varian Cary 5000 spectrophotometer. The light source is a halogen lamp in combination with a grating monochromator. Behind the monochromator, a chopper wheel sends the light beam into one of three possible states.

The preparation of the monochromatic light beam for both channels is shown in Fig. 2.3. The light source is a halogen lamp in combination with a grating monochromator. Behind the monochromator, a chopper wheel sends the light beam into one of three possible states:

1. The light beam is guided into the sample channel for a measurement of the sample S_S.

2. The light beam is guided into the monitor channel for a measurement for the light sources intensity S_M. This accounts for changes in the light source.

3. The light beam is blocked for a measurement of the dark signal S_0. In order to eliminate detector noise and light scattered into the detector from other sources.

The chopper wheel rotates with a frequency of 30 Hz, each rotation leads to a measurement of S_S, S_M and S_0. The detection setup with integrating sphere is shown in Fig. 2.4. The light beam of the sample channel (red) hits the sample either at the transmission port before entering the sphere or after crossing the sphere for the first time at the reflection port. The light beam of the monitor channel (green) travels a different way into the sphere and hits the calibration standard with a reflectivity $R_{Std}(\lambda)$ known from the "Physikalisch-Technische Bundesanstalt" (PTB). The objects in the reflection or monitor port are hit

at an angle of 8°, so that specular reflected light doesn't exit after on reflection via the transmission port or the hole through which the monitor beam enters the integrating sphere. For detection of the signals a photomultiplier in the UV-Vis and a PbS-detector in the NIR spectral range are used.
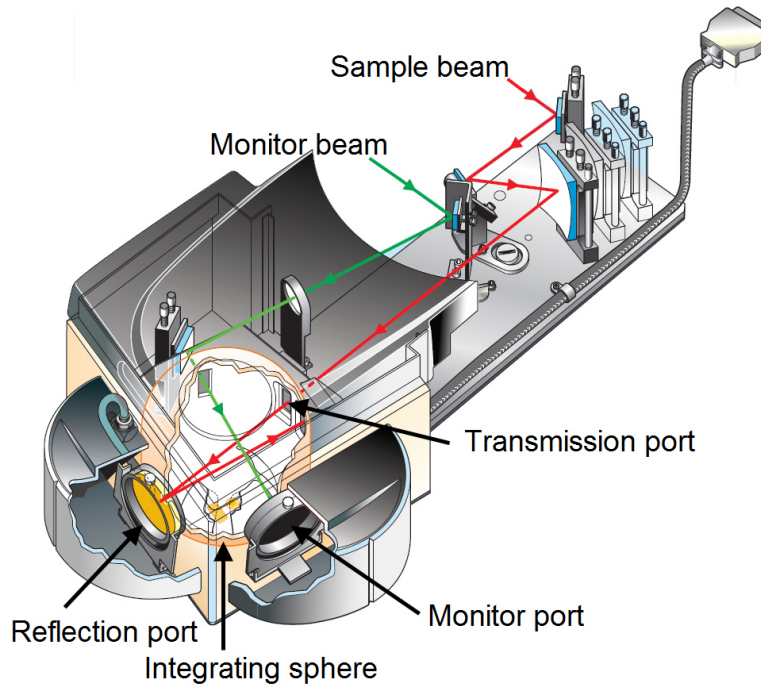
Figure 2.4: The integrating sphere of the Varian Cary 5000 spectrophotometer (the illustration is taken from [AT13]). The light beam of the sample channel (red) hits the sample either at the transmission port before entering the sphere or after crossing the sphere for the first time at the reflection port. The light beam of the of the monitor channes is shown in green.

From those three signals one measurement signal $S(\lambda)$ is calculated as follows:

$$S(\lambda) = \frac{S_S(\lambda) - S_0(\lambda)}{S_M(\lambda) - S_0(\lambda)}. \tag{2.8}$$

This equation corrects systematic measurement errors of dark signal noise of the detector S_0 as well as errors due to changes in the light source over time. All measurement signals in the following are measured according to eq. 2.8, since the Varian Cary only sends $S(\lambda)$ and not S_0, S_S, S_M to the computer controlling it and collecting the data.

2.2.1 Reflection measurement

To determine the absolute value of the reflection $\rho(\lambda)$ of a sample three measurements with different objects in the reflection port (Fig. 2.4) are necessary [Pee14]:

  1. A zero baseline $\rho_{0\%}(\lambda)$ measurement with air in the reflection port. This is necessary,

since not all light from the sample channel leaves the integrating sphere through the empty reflection port.

2. A one hundred percent baseline $\rho_{100\%}(\lambda)$ measurement with a reflection standard sample (the standard is reflecting either diffuse or specular) in the reflection port, so that all light from the sample channel is detected.

3. A measurement $\rho_{\mathrm{rel}}(\lambda)$ with the sample in the reflection port. (If several samples are measured in a row only this third step has to be repeated for each sample.)

From those measurements the absolute reflection $\rho(\lambda)$ follows from

$$\rho(\lambda) = \frac{\rho_{\mathrm{rel}}(\lambda) - \rho_{0\%}(\lambda)}{\rho_{100\%}(\lambda) - \rho_{0\%}(\lambda)} \rho_{\mathrm{Std}}(\lambda), \tag{2.9}$$

where $\rho_{\mathrm{Std}}(\lambda)$ is the reflection of the standard used for the $\rho_{100\%}(\lambda)$ measurement, as calibrated at the PTB.

2.2.2 Transmission measurement

To determine the absolute transmission value $\tau(\lambda)$ of a sample two measurements with different setups in the transmission port (Fig. 2.4) are necessary. For both measurements a diffuse reflection standard made of spectralon is mounted in the reflection port:

1. A one hundred percent baseline $\tau_{100\%}(\lambda)$ measurement with only air in the transmission port, so that as much light as possible from the sample channel is detected.

2. A measurement $\tau_{\mathrm{rel}}(\lambda)$ with the sample in the transmission port.

From those measurements the absolute transmission $\tau(\lambda)$ follows from:

$$\tau(\lambda) = \frac{\tau_{\mathrm{rel}}(\lambda)}{\tau_{100\%}(\lambda)}. \tag{2.10}$$

It is assumed that $\tau_{\mathrm{Std}}(\lambda) = 1$, since air is used to acquire the one hundred percent baseline (air does not absorb light in the wavelength range from 250-2500 nm). It is unnecessary to place a zero baseline $\tau_{0\%}(\lambda)$ measurement with an intransparent object in the transmission port, because this already happens when the chopper wheel blocks the sample beam channel [Pee14].

Further discussion and an uncertainty analysis of measurements conducted with this instrument can be found in [Pee14].

2.2.3 Extracting the refraction index from reflection and transmission measurements

When measuring the reflection of materials that transmit light, one has to consider the reflection at its rear side due to multiple internal reflections. Just as the change of the transmission measurement through multiple internal reflections has to be accounted for.

To avoid misunderstandings, the reflectivity $R(\lambda)$ and transmitivity $T(\lambda)$ at an interface is denoted in capital roman letters, while the reflection $\rho(\lambda)$ and transmission $\tau(\lambda)$ of a slab including multiple internal reflections is denoted in Greek letters. For clarity, the wavelength λ or angle of incidence is not always noted for the remainder of this chapter.

2.2.4 Reflection and transmission of one planar slab

The situation for one planar slab is illustrated in fig. 2.5. The light is incoming from a surrounding front side medium with $\hat{n}_0$ and an angle of incidence θ_0. It subsequently interacts with the slab with $\hat{n}_1$ and a thickness of d_1. In case of transmission at the first interface it also interacts with the surrounding rear side medium with $\hat{n}_2$.
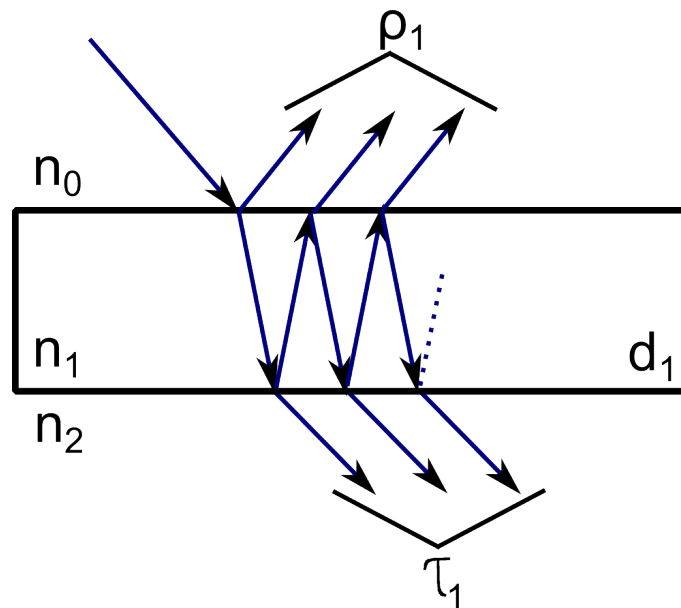
Figure 2.5: The light is incoming and interacting with a planar slab with $\hat{n}_1$ and a thickness of d_1. Various light paths to reflection and transmission are illustrated.

In this case the reflection ρ_1 from the slab consists of the reflection when the light hits the interface R_{01} (as an abbreviation of $R_{01}(\hat{n}_0, \hat{n}_1, \theta_0)$), when it is internally reflected once, $T_{01}e^{-2\alpha_1 d_1/\cos(\theta_1)}R_{12}T_{10}$ with $\theta_1 = \arcsin(\frac{\hat{n}_0 \sin(\theta_0)}{\hat{n}_1})$, and in case of multiple internal reflections a factor of $R_{10}e^{-2\alpha_1 d_1/\cos(\theta_1)}R_{12}$ describes the light passing through the first

slab. Following this iteration ρ_1 resulting in

$$\rho_1 = R_{01} + T_{01}e^{-2\alpha_1\breve{d}_1}R_{12}T_{10} + T_{01}e^{-2\alpha_1\breve{d}_1}R_{12}T_{10}R_{10}e^{-2\alpha_1\breve{d}_1}R_{12} + ... \tag{2.11a}$$

$$= R_{01} + T_{01}e^{-2\alpha_1\breve{d}_1}R_{12}T_{10}(1 + R_{10}e^{-2\alpha_1\breve{d}_1}R_{12} + ...) \tag{2.11b}$$

$$= R_{01} + T_{01}e^{-2\alpha_1\breve{d}_1}R_{12}T_{10}\sum_{i=0}^{\infty}(R_{10}e^{-2\alpha_1\breve{d}_1}R_{12})^i \tag{2.11c}$$

$$= R_{01} + \frac{T_{01}e^{-2\alpha_1\breve{d}_1}R_{12}T_{10}}{1 - R_{10}e^{-2\alpha_1\breve{d}_1}R_{12}}, \tag{2.11d}$$

where $\breve{d}_1 = d_1/\cos(\theta_1)$ is used as an abbreviation. In the last step the property of an infinite geometrical series is used: $\sum_{i=0}^{\infty}x^i = \frac{1}{1-x}$ for $|x| < 1$. For the transmission τ_1 of the slab the following can be derived with the same reasoning:

$$\tau_1 = T_{01}e^{-\alpha_1\breve{d}_1}T_{12} + T_{01}e^{-\alpha_1\breve{d}_1}T_{12}R_{12}e^{-2\alpha_1\breve{d}_1}R_{10} + ... \tag{2.12a}$$

$$= T_{01}e^{-\alpha_1\breve{d}_1}T_{12}(1 + R_{12}e^{-2\alpha_1\breve{d}_1}R_{10} + ...) \tag{2.12b}$$

$$= T_{01}e^{-\alpha_1\breve{d}_1}T_{12}\sum_{i=0}^{\infty}(R_{12}e^{-2\alpha_1\breve{d}_1}R_{10})^i \tag{2.12c}$$

$$= \frac{T_{01}e^{-\alpha_1\breve{d}_1}T_{12}}{1 - R_{12}e^{-2\alpha_1\breve{d}_1}R_{10}} \tag{2.12d}$$

Note that in both equations 2.11 b, c and 2.12 b, c there is one term which describes the entry and the exit of the light in the slab and a second term which is identical for both reflection and transmission because it describes the internal reflection between both sides.

2.2.5 Calculating diffuse reflectance between two media

In the previous section only specular reflection was discussed, where the angle of incidence equals the angle of reflection. However, there are also surfaces that have a diffuse reflection where the angle of reflection is distributed. In this section the following system is considered, as depicted in Fig. 2.6, where the surrounding is a non absorbing medium (typically air) with n_0, the slab (typically EVA) with $\hat{n}_1$ and thickness d_1, and a reflector with a surface reflection R_{12}^* below the slab (typically a back sheet).

This approach assumes R_{12}^* to be the reflected fraction, and for the directional distribution of the reflected light an ideal diffuse reflection according to equation 2.13. Lambert's cosine law [Lam60] states that the product of reflected intensity $I_R(\theta_R)$ and the viewed surface area A^* is constant:

$$\text{const} = I_R(\theta_R)A^*(\theta_R) . \tag{2.13}$$
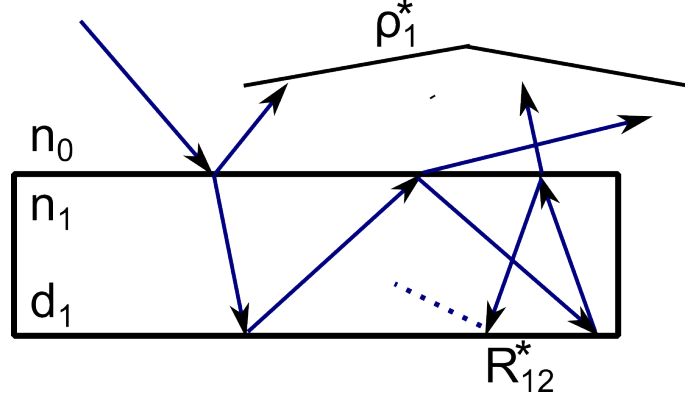
Figure 2.6: The light is incoming and interacting with a system of one planar slab having a lambertian reflection at the rear. Various light paths to reflection ρ_1^* are illustrated considering multiple internal reflections.

A good example of this is a white sheet of paper, which looks always equally bright no matter from which angle one looks at it. Since the area viewed by an observer increases with $1/cos(\theta_R)$, where θ_R is the angle between the normal of the surface and the observer, the reflected intensity of such an ideal $I_R(\theta_R)$ has to decrease with $cos(\theta_R)$. Under these assumptions, the reflection at the rear surface of the slab $R_{12}(\theta_R)$ can be described as:

$$R_{12}(\theta_R) = R_{12}^* cos(\theta_R). \tag{2.14}$$

Note that in this case the reflection is completely independent of the angle of incidence. In this section the more complex system shown in Fig. 2.6 is considered. The reflexion ρ_1^* of this system can be described as:

$$\rho_1^* = R_{01} + T_{01}e^{-\alpha_1 \breve{d}_1} R_{12}^* B_{esc} \left(1 + B_{int}R_{12}^* + (B_{int}R_{12}^*)^2 + ...\right) \tag{2.15a}$$

$$= R_{01} + T_{01}e^{-\alpha_1 \breve{d}_1} R_{12}^* B_{esc} \sum_{i=0}^{\infty} (B_{int}R_{12}^*)^i \tag{2.15b}$$

$$= R_{01} + \frac{T_{01}e^{-\alpha_1 \breve{d}_1} R_{12}^* B_{esc}}{1 - B_{int}R_{12}^*} \, , \tag{2.15c}$$

where R_{01} is the reflection at the front surface, T_{01} determines what fraction of the light enters the slab, $e^{-\alpha_1 \breve{d}_1}$ determines what fraction gets absorbed before the interaction at the rear, R_{12}^* is the reflection at the rear side and B_{esc} describes what fraction of the light reflected at the rear side escapes the slab at the front after a single pass – while considering the distribution of the reflected light and the absorption in the media. The term $B_{int}R_{12}^*$ describes the fraction of light that remains after one diffuse reflection at the rear, a specular reflection at the front and the absorption in between. For the light that gets reflected

internally B_{int} can be calculated as follows:

$$B_{int} = 2 \int\limits_{0}^{\pi/2} d\theta_R \cos(\theta_R) \sin(\theta_R) e^{-2\alpha_1 d/\cos(\theta_R)} R_{10}(\theta_R) \; , \qquad (2.16)$$

where $\cos(\theta_R)$ describes a diffuse reflection according to Lambert (Eq. 2.13), $e^{-2\alpha_1 d/\cos(\theta_R)}$ the absorption for crossing the slab twice and $R_{10}(\theta_R)$ is the fraction of reflected light at the front. In case of total reflection ($\theta_R > \arcsin(\frac{n_0}{n_1})$) reflection is set to one $R_{10}(\theta_R) = 1$. For $\theta_R \leq arcsin(\frac{n_0}{n_1})$, $R_{10}(\theta_R)$ is calculated with the Fresnel equation:

$$R_{10}(\theta_R)) = \frac{1}{2} \left(\left| \frac{n_1 \cos(\theta_R) - n_0 \cos(\theta_R)}{n_1 \cos(\theta_R) + n_0 \cos(\theta_R)} \right|^2 + \left| \frac{n_1/\cos(\theta_R) - n_0/\cos(\theta_R)}{n_1/\cos(\theta_R) + n_0/\cos(\theta_R)} \right|^2 \right), \; (2.17)$$

where it is assumed that no polarization state is favored. The light reflected at the rear side that escapes the slab at the front side, B_{esc}, is calculated via

$$B_{esc} = 2 \int\limits_{0}^{\pi/2} d\theta_R \cos(\theta_R) \sin(\theta_R) e^{-\alpha_1 d/\cos(\theta_R)} T_{10}(\theta_R), \qquad (2.18)$$

where $T_{10}(\theta_R) = 1 - R_{10}(\theta_R)$ since it is assumed that no absorption happens at the infinitesimal thin interfaces. Note how both B_{esc} and B_{int} are only dependent on the material properties of the slab $\hat{n}_1, d_1$ and on the medium surrounding the front n_0. This enables one to solve Eq. 2.15c for R_{12}^* and describe it as a function of $(n_1, k_1, d_1, n_0, \theta_0, \rho_1^*)$:

$$R_{12}^*(n_1, k_1, \breve{d}_1, n_0, \rho_1^*) = \frac{\rho_1^* - R_{01}}{\rho_1^* B_{int} - R_{01} B_{int} + T_{01} e^{-\alpha_1 \breve{d}_1} B_{esc}}, \qquad (2.19)$$

where $\breve{d}_1 = d_1/\cos(\arcsin \frac{n_0}{n_1} \sin(\theta_0))$ with the angle of incidence θ_0. This means the reflectivity R_{12}^* of a solar module back sheet can be derived, while it is encapsulated with EVA, from the reflexion measurement ρ_1^* with an integrating sphere described in section 2.2.1. The only assumptions are that $n_1 >> k_1$ and that the backsheet has a diffuse reflection distribution according to Lambert (Eq. 2.14). Of course one has to know the EVA's material properties (see Sec. 3.3) and thickness as well as the angle of incidence θ_0.

This is relevant for two main reasons: First the reflection at the rear side of the PV module in the simulation takes place at the exact same interface but with more interactions in front of it, and second because most back sheets already have a thin EVA layer on top of it after manufacturing to increase the adhesion after lamination.

2.3 Conclusion

For determining the refractive index $\hat{n}(\lambda)$ of a material, this chapter introduced a measurement method based on spectroscopic ellipsometry and transmission, as well as a method based on reflection and transmission. The first one is more precise, but also requires a sample surface with very little roughness so that the phase can be detected. The second method is also capable of measuring samples with diffuse reflection characteristics.

The data analysis for ellipsometry, based on Monte-Carlo, and the technique for measuring a diffuse reflector through another layer were both newly developed during this thesis.

The results of the measurement techniques and data analysis methods introduced here are presented in the next chapter.

CHAPTER 3

Measurement results: Determining the optical parameters of all solar cell module components

This chapter presents and discusses the measurement results of the optical constants of soda-line glass, anti reflection coatings (ARC) for glass, the most common encapsulation materials EVA and silicone, the back sheets reflection as well as the cell components: silicon, silicon nitride (which is commonly used for passivation and cell anti-reflection properties) and the aluminium rear reflector. The best values measured or available in literature are given in the appendix B in tabulated form for further use.

3.1 Optical properties of glass

The front glass covering standard solar cell modules is typically the thickest medium the light passes before reaching the solar cells. Hence, it is very important to reduce the parasitic absorption losses in this glass sheet. Most commonly, soda-lime glass is taken, which contains from its raw materials a number of contaminants acting as coloring agents.

The most important agent is iron. It exists in the two oxidation states Fe^{2+} and Fe^{3+} with their corresponding chemical formula of FeO and Fe_2O_3, whose redox ratio $[Fe^{2+}]/[Fe]_{tot}$ or $[Fe^{3+}]/[Fe]_{tot}$ depends on the fabrication process [Dun12]. The Fe^{3+} state absorbs mainly UV light and is less important in terrestrial photovoltaic modules. Whereas, the Fe^{2+} state is the primarily responsible for a very broad absorption band in the near infrared, hence gives the glass the characteristic green color and reduces module efficiency considerably.

Additives like Ce and Sb could be used to shift the redox ratio towards Fe^{3+}. However, most photovoltaic module glasses are fabricated with the floating technique commonly using tin, which reacts strongly with additives like Ce and Sb, hence, these additives cannot be used. For these reasons, raw materials with very low iron content are used for photovoltaic applications, and a residual iron concentration is not avoided. Therefore predictions of how strongly iron reduces module power are in demand.

Determining the optical constants of different soda-lime glasses has been a topic of scientific research for many years. Rubin [Rub85] published a widely used data set of five different

types of soda-lime glasses with varying extinction coefficients $k(\lambda)$, but did not quantify their iron content. There have been publications [Tra92; Uch00] that measured the iron concentration of different glass samples and linked it to the absorption coefficient at certain wavelengths. However, no study is known to me which not only quantified the iron content but related it to measured k spectra as a function of wavelength and iron content.

In [Vog15b] the measurements of the optical constants and the iron concentration is described for nine different commercially available glass samples. From these, two semi empirical models are derived for the extinction coefficient of glass as a function of wavelength and iron concentration. In the following the development and results of [Vog15b] are given.

A total of nine different float soda-lime glass samples were bought from commercial suppliers and analyzed. The sample thickness ranges from 1.03 mm to 3.84 mm. The transmittance of the nine glass samples is measured at perpendicular incidence.

For the spectral ellipsometry measurements (for details see Sec. 2.1), the angles of incidence are 50°, 60° and 70°. The samples are oriented with the tin layer at the rear because the tin layers are known to have slightly different optical properties than the bulk glass [Syn11]. The reflection at the tin side is prevented from reaching the detector using a light trap at the rear side of the glass samples.

In the data analysis, each sample was modeled with a 1–2 nm thin surface layer to mimic surface roughness [She80; Syn11]: the surface layer's optical constants are determined by using an effective medium approach (EMA) [Woo10] assuming 50% glass from the bulk and 50% air. This surface layer leads to better agreement between the measured data and the fits. Finally, the refraction index n and the extinction coefficient k of the glass bulk layer are fitted wavelength-by-wavelength (for details see Sec. 2.1.2) to the measured data.

The resulting dependence of the measured $k(\lambda, x)$ on wavelength and on iron content x is depicted in Fig. 3.1 (see section 3.1 for a description of the measurement of the iron content). Our wavelength range shows two of the three main wavelength zones:

1. The absorption edge in the UV. It is attributed to transitions from electrons orbitals of oxygen ions to those of the ions Fe^{2+} and Fe^{3+} [Ade90]. At 320 nm, a linear relationship between k and the total iron concentration – independent of oxidation state – was reported [Ade90; Tra92]. At wavelengths below 400 nm, Fe^{3+} plays a more important role than Fe^{2+} [Bin07; Tra92; Uch00]. Because interatomic transitions (d → d) are forbidden, k is small in the range between about 400 nm and 700 nm.

2. A very broad absorption band, centered at 1064 nm, is attributed to the Fe^{2+} ion [Ade90] in an octahedral state [Bin99], and a proportionally relationship of k with the corresponding Fe^{2+} concentration is found [Ade90].

3. The third zone is situated beyond 2.15 µm wavelength caused by molecular bond transitions (above 3.2 µm wavelength, these glasses are almost opaque [Cle66; Rub85]).
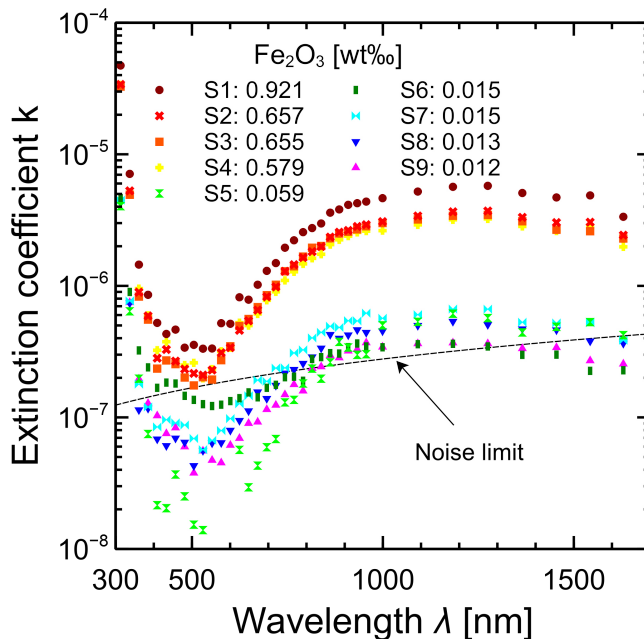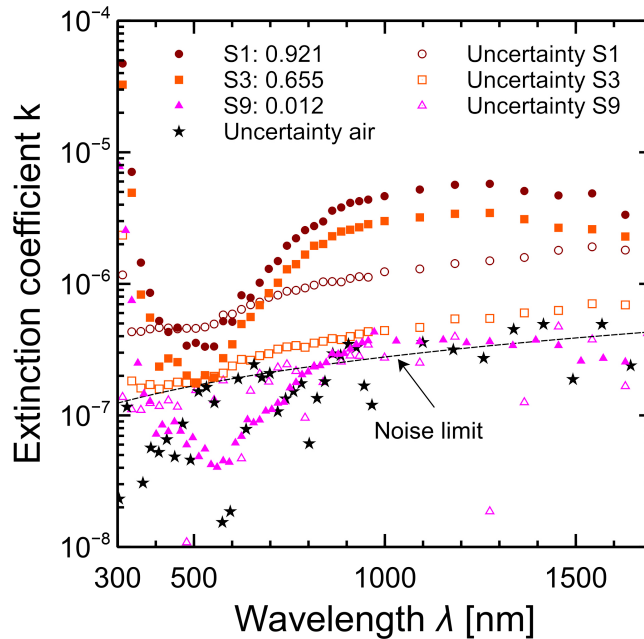
Figure 3.1: The extinction coefficient k in nine soda-lime float glass samples, having the indicated iron concentrations (in units of Fe_2O_3 total weight ‰), derived from spectroscopic ellipsometry and transmission measurements. The noise limit is derived using the Monte Carlo method indicated in Fig. 3.2.

Note that the samples were bought from various manufacturers, so the redox radio between Fe^{2+} and Fe^{3+} ions may vary. Because different parts of the k-spectrum are influenced to various degrees by the Fe^{2+} or Fe^{3+} ions, the k-spectra should not be expected to be strictly parallel to each other. Indeed, there are small cross-overs, like between S2 and S4.

Below about 2×10^{-7}, the k-values show considerable scatter. To determine the uncertainty, the Monte-Carlo procedure introduced in Sec. 2.1.2 is used. The results for three samples with significant different iron concentrations are shown in Fig. 3.2. For S1 and S3 the uncertainties (empty symbols) are below the k values (filled symbols) expect for the minimum around 500 nm. For S9 the uncertainty is very discontinuous and mostly above the k values.

To investigate the high uncertainty of S9, air is measured with the spectral ellipsometer in the transmission set-up. To convert the air measurement noise level from transmission data into k, a model with a single layer, a thickness of 3 mm (which is the thickness of the samples with the lowest k-values), $n = 1$ for all wavelengths is build. Next this model is fitted using 1000 iterations of the Monte Carlo method procedure. The uncertainty of the air measurement is indicated as black stars in Fig. 3.2; it reaches from about 1×10^{-7} at 300 nm to 4×10^{-7} at 1600 nm as indicated by the black line. Consequently, all k values shown in Fig. 3.1 have at least this uncertainty. In case of samples five through nine, the

Figure 3.2: The extinction coefficient k of some of the samples in Fig. 3.1 (filled symbols). Their uncertainty values (empty symbols) are generated by an analysis based on Monte-Carlo. The noise limit (dashed line) is derived from a transmission measurement of air (stars).

lowest k values have an uncertainty over 100% relative.

Figure 3.3 shows the real part of the refractive index n of the nine glass samples. The average has a standard deviation below 1 % for each wavelength and is in very good agreement with the model-fit through the average data of all samples obtained by spectroscopic ellipsometry. Only S3 deviates noticeable out of the range of the standard deviation, but this might be due to the fact that this sample is from a different manufacturer. Thus the real part of the refractive index appears to be independent of the iron concentration, as is expected from the Krames-Kronig relationship in case of low absorption.

Determining the iron concentration with ICP-OES

The ICP-OES measurement to determine the iron concentration is a three step process [Azz02]:

1. The glass samples are dissolved by hydrofluoric acid digestion, supported by heating via microwaves.

2. A small part of the solution is vaporized in a graphite tube at a temperature of about 3000°C. Using microwave radiation, the sample's gas is turned into a plasma with temperatures around 10000°C.
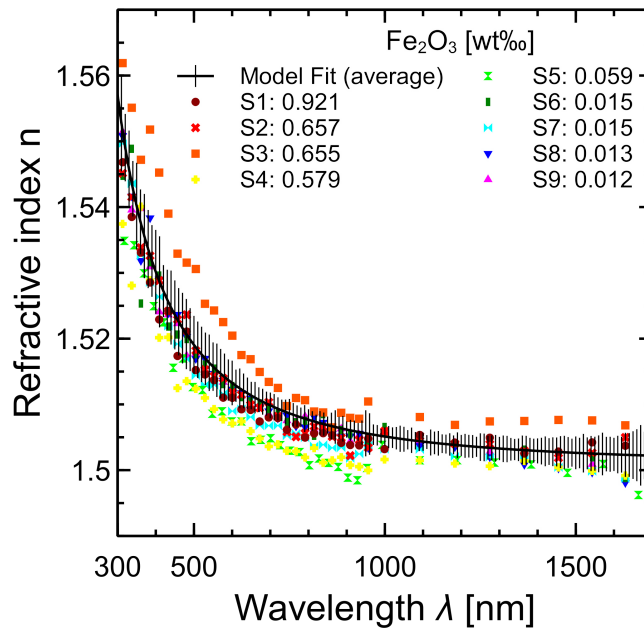
Figure 3.3: Measurements show the real part of the refractive index of the nine glass samples appears to be independent of the iron concentration. The average has a standard deviation below 1 % for each wavelength and is in very good agreement with the model-fit through the average of all samples' spectroscopic ellipsometry data.

3. Finally, a spectrometer is used to detect the plasma's characteristic radiation and to compare it to a reference measurement of a solution with known iron concentration.

Because the iron content is determined in a plasma, it is not possible to distinguish between Fe^{2+} and Fe^{3+} ions, hence the values indicate the total amount of iron. In the literature, it is customary to relate the total amount of iron as weight total percentage of Fe_2O_3, which corresponds to a factor of $(2m_{Fe} + 3m_O)/(2m_{Fe}) \approx 1.43$. The results are shown in Figs. 3.1 through 3.4 in units of Fe_2O_3 weight total per thousand. The values vary over nearly two orders of magnitude from sample 1 (S1) with 0.921‰ ± 0.005‰ to S9 with 0.012‰ ± 0.0005‰.

Semi-empirical model

According to [Tra92], there is a linear dependency between the total amount of iron in glass and its extinction coefficient at the wavelength of 320 nm. Our measurements are, as shown in Fig. 3.4, in good agreement with this linear dependency. The error bars calculated by the Monte Carlo method are smaller than the symbol size. Thus, this linear trend is the basis of the two semi-empirical models introduced in the following. Both models are in good agreement with S1 through S4, but differ from the samples with iron weight total below 0.1 ‰.
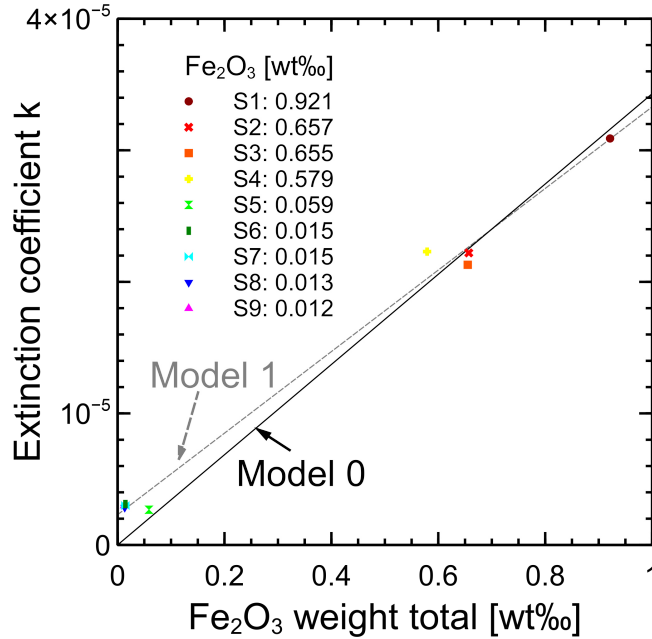
Figure 3.4: The extinction coefficients from Fig.3.1 at a wavelength of 320 nm, plotted versus the Fe_2O_3 concentration in weight total material per thousand. The data suggests a linear dependency. Model 1 is the best linear fit through all measured values, while Model 0 is the best linear fit through the origin.

Model 0 assumes that the entire absorption in the glass is due to iron. Consequently, the linear fit though all measurement points is pin-pointed at the origin in Fig.3.4 and is:

$$k_{320}^{M0}(x) = 3.43 \times 10^{-5} \times x, \tag{3.1}$$

where k_{320}^{M0} is the extinction coefficient at 320 nm and x is the Fe_2O_3 weight total per thousand.

Model 1 is based on the realistic assumption that there is some absorption in the glass not due to the iron, but from other impurities or from the intense UV bands characteristic of the vitreous matrix [Ade90]. Therefore, the best linear fit though all measurements is used without restrictions:

$$k_{320}^{M1}(x) = 3.10 \times 10^{-5} \times x + 2.3 \times 10^{-6}, \tag{3.2}$$

where k_{320}^{M1} and x have the same meaning as above. Model 1 assumes an absorption not caused be the iron of about 2.3×10^{-6} at 320 nm. Model 1 agrees better with our data than model 0, with least square fit R^2 values of 0.992 (M1) and 0.968 (M0). However, this distinction may not be significant, because the Fe^{2+} to Fe^{3+} concentration ratios could not be measured separately, and they may vary among the nine samples and affect the k-spectra in different parts by different amounts.

So far, two linear models at 320 nm were derived. Now, a suitable k-spectrum is extracted to pin-point it to 320 nm via Eqs. (3.1) and (3.2). For this, the average extinction coefficient $k_{avg}(\lambda)$ of all samples with more than $0.1‰$ of Fe_2O_3 is taken, which has an average iron concentration $x_{avg} \approx 0.7‰$. Through averaging over those samples, the impact of different oxidation ratios is reduced, so is the measurement noise and the impurities in a single sample. The measurement set-up gathers data at 583 different wavelengths. To obtain more suitable values for further calculations the number of wavelengths of $k_{avg}(\lambda)$ is reduced to one every 10 nm by a cubic-spline interpolation. It is listed in the appendix table B.2. Hence, the model for the k-spectrum is:

$$k_Z(\lambda) = k_{avg}(\lambda)\frac{k_{320}^Z(x)}{k_{320}^Z(x_{avg})},$$

(3.3)

where Z is either M0 or M1, depending which model one likes to use.
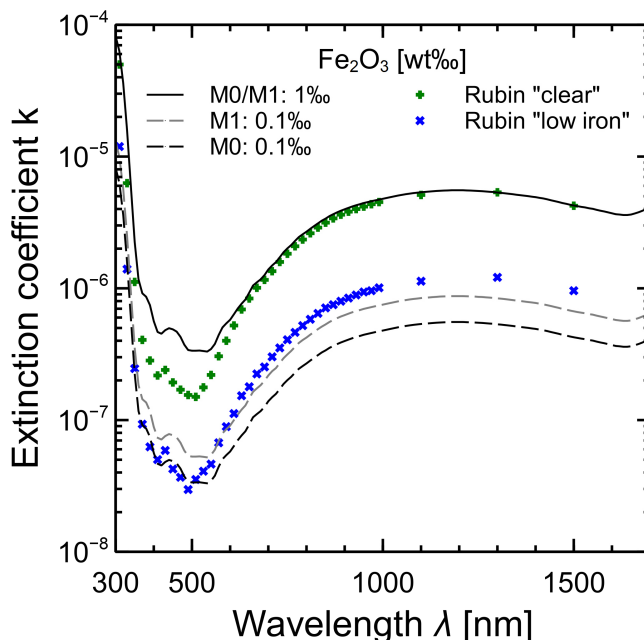
Figure 3.5: The two soda-lime glass samples from [Rub85] with the lowest extinction coefficient, compared to the models developed here. The "clear" sample is similar to $Fe_2O_3=1‰$, while the "low-iron" sample is similar to M1 with $Fe_2O_3=0.1‰$ or to M0 with $Fe_2O_3=0.2‰$.

Comparison with literature values

Figure 3.5 shows a comparison between our two models and the two samples with the lowest extinction coefficient from Rubin [Rub85] denoted there as "clear" and "low-iron" soda-lime glass. The "clear" sample is similar to sample 1 from this work as well as to both models for $x = 1‰$ (both models are very similar for these high iron concentrations). The biggest difference between our models and the "clear" sample is below 600 nm, indicating that the "clear" sample has a lower Fe^{3+}/Fe^{2+} ratio than the samples used for our model.

The shape of the k-spectrum of the "low-iron" sample also indicates that Rubin's samples have a lower Fe^{3+}/Fe^{2+} ratio, however, their k-values above 600 nm are very similar to M1 with $x = 0.1‰$ or M0 with $x = 0.2‰$.

3.2 Optical properties of antireflective coatings for glass

An anti-reflective coating (ARC) reduces the reflectivity at the air/glass interface at the module front side. This is important, since the front side surface reflection is typically the highest optical loss in a Si-wafer based solar module.

Figure 3.6 depicts the transmission measurement of low-iron solar float glass (according to DIN EN 572-2) with ARC on one side (blue squares) and without ARC (purple triangles). The ARC increases the transmission at all measured wavelengths (between 300 nm and 1700 nm) by on average of 0.014, and by 0.019 for the wavelength range between 300 nm and 1200 nm, with the highest increase of 0.026 at 570 nm. The measurements were conducted with the spectroscopic ellipsometer as described in sec. 2.1.1.
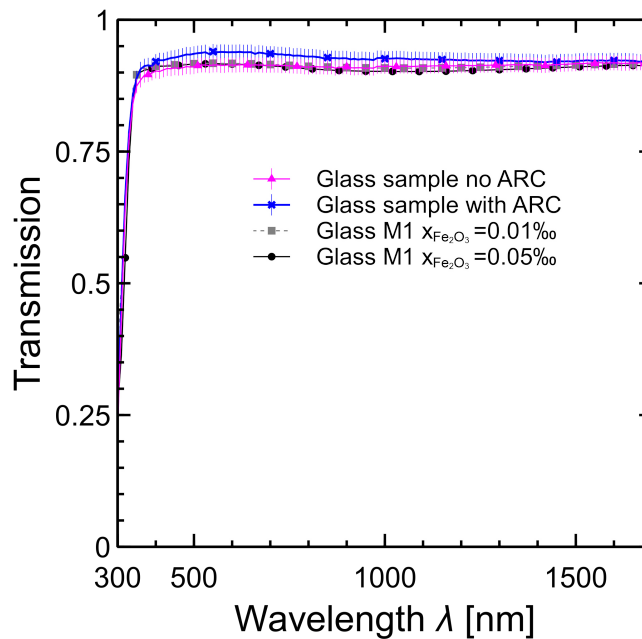
Figure 3.6: Colored symbols: transmission of a glass sample, measured with the spectroscopic ellipsometer described in sec. 2.1.1, with and without antireflective coating. Grey symbols: as calculated with equation 2.12 and the model 1 in sec. 3.1.

The other two curves (with grey symbols) in Fig. 3.6 are calculated using the refractive index data n and $k^{M1}(\lambda, x_{Fe_2O_3})$ of glass using model 1 from sec. 3.1 and the equation 2.12 for transmission of one planar slab with a thickness of 3.2 mm. Both calculated curves are within the error bars of the glass sample with no ARC; the better agreement around 1000 nm indicates that the sample has an iron weight total concentration of $x_{Fe_2O_3} \approx 0.01‰$.

Additionally one can see some difference within the error bars between both models and the sample in the wavelength range from 350 nm to 450 nm.

The refractive index of the samples is obtained by combining the transmission measurement with ellipsometry measurements. The results are shown in Fig. 3.7. The glass bulk values (purple triangles) are determined from the sample with no (ARC) oriented with the tin layer at the bottom. The tin-layer was determined by measuring the sample with no (ARC) but oriented with the tin layer at the top and assuming a substrate of 3.2 mm glass bulk below the tin-layer, whose thickness and real part of the refractive index $n_{\mathrm{Tin}}(\lambda)$ were fitted assumed that $k_{\mathrm{Tin}}(\lambda) = 0$. In both cases the reflection at the bottom side was prevented by using a light trap in form of a quartz wedge and liquid paraffin. The resulting thickness of the tin layer is 170 nm and the $n_{\mathrm{Tin}}(\lambda)$-values are shown as red circles. The glass bulk values are about a factor of 0.01 below the $n_{\mathrm{Tin}}(\lambda)$-values for the tin layer. This is about half the difference determined by [Syn11]. Without measuring the same samples it is hard to determine whether the difference is due to the samples or due to different measurement procedures.
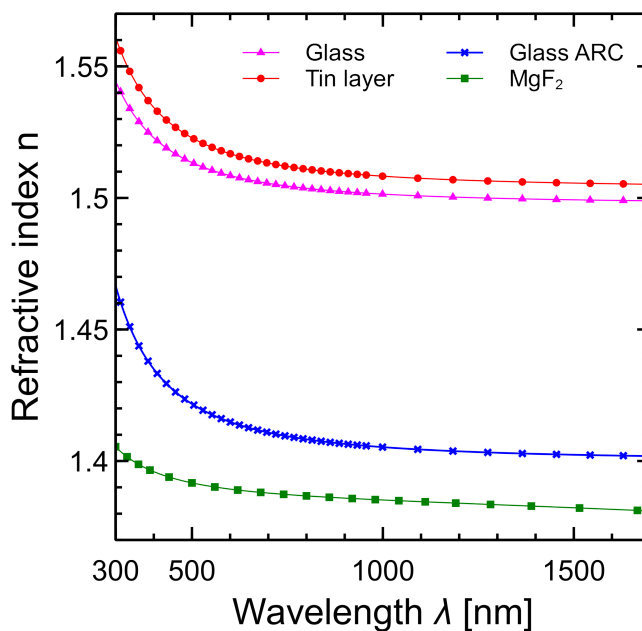
Figure 3.7: The refractive indices of bulk glass, its tin layer, and its anti-reflection coating, obtained from a combination of the transmission measurement and ellipsometry measurements. Literature values [Pal85] for MgF_2 are shown for comparison.

The ARC of the glass sample is placed on top of the tin-layer, which is why in contrast to the previous section one needs to know the tin layer's optical properties. I assume in accordance with the description from the manufacturer that the glass itself including the tin-layer are the same in both samples. The sample with an ARC is placed in the ellipsometer with the ARC on top. From the measurement I then determine the ARC layer's thickness and real part of the refractive index $n_{\mathrm{ARC}}(\lambda)$ via fit (assuming that the ARC and the glass itself

including the tin-layer are the same in both samples $k_{ARC}(\lambda) = 0$). The resulting ARC thickness is 99 nm and the $n_{ARC}(\lambda)$-values are shown as blue crosses in Fig. 3.7 and listed in table B.1. They are about 0.1 below the glass bulk values. Comparing the measured ARC to the literature values for magnesium fluoride (MgF_2, green squares) [Pal85], which is often used as an ARC for glass, it is obvious that the measured ARC has an 0.05 higher refractive index in the UV at 300 nm and a 0.02 higher refractive index in the VIS-NIR. This indicates that no a magnesium fluoride based ARC was measured here, but an ARC that may be made of a porous glass layer.

3.3 Optical properties of encapsulant materials

In a typical industrial type silicon solar module there are two layers of encapsulation one directly above the cells and below the glass, the other below the cell and above the backsheet. The encapsulation material is applied via a lamination process. The encapsulation material serves the following purposes:

- Be flexible buffer between the glass and the cells to protect the cells from breaking.

- Allow space for the cell interconnections to be placed within, which are necessary to extract the electrical power from the module.

- Have a refractive index n as close to glass as possible to reduce reflection loss at the glass/encapsulation material interface and absorb as little light as possible.

- Electric isolation of the cells and the cell interconnectors.

- Have high thermal conduction to reduce the cells operating temperature as much as possible (see Ch. 6).

Ethyl vinyl acetate (EVA) is the most common encapsulant material. Silicone is an alternative material reported the have several advantages [Ket08] such as less degradation over time, better electrical isolation and also higher transmission in the UV wavelength range than conventional UV absorbing EVA_{UV-A}.

A couple of years ago industrial solar cells had very low conversion efficiencies for UV light, therefore it was less important for encapsulation materials to transmit UV-light, but nowadays solar cells with better UV light conversion rates have entered mass production. Thus an emphasis on more transmission in the UV was placed for the encapsulation material.

In this section three sample are measured one made of EVA_{UV-A} with a thickness of (9.85 ± 0.25) mm, another made of EVA_{UV-T} with a thickness of (10.2 ± 0.2) mm and the third another made of $silicone_{UV-T}$ with a thickness of (9.4 ± 0.4) mm. The samples are laminated from 25 layers of each respective material, at each end is a foil, which is removed without damage to the surface.

Each samples transmission is determined with the method described in Sec. 2.2.2 and afterwards a spectroscopic ellipsometry measurement (Sec. 2.1.1) is conducted for angles of incidence of 50°, 60° and 70°. The reflection at the bottom side was prevented using a light trap in form of a quartz wedge and liquid paraffin.

For data analysis all samples are modeled as a substrate, whose $n(\lambda)$ and $k(\lambda)$ have to be determined and a the surface layer's modeling the roughness in the order of about 1 nm. The surface layer's optical constants are determined by using an effective medium approach (EMA) [Woo10] assuming 50% substrate from the bulk and 50% air. All three fit-methods (Sec. 2.1.2) show good agreement.
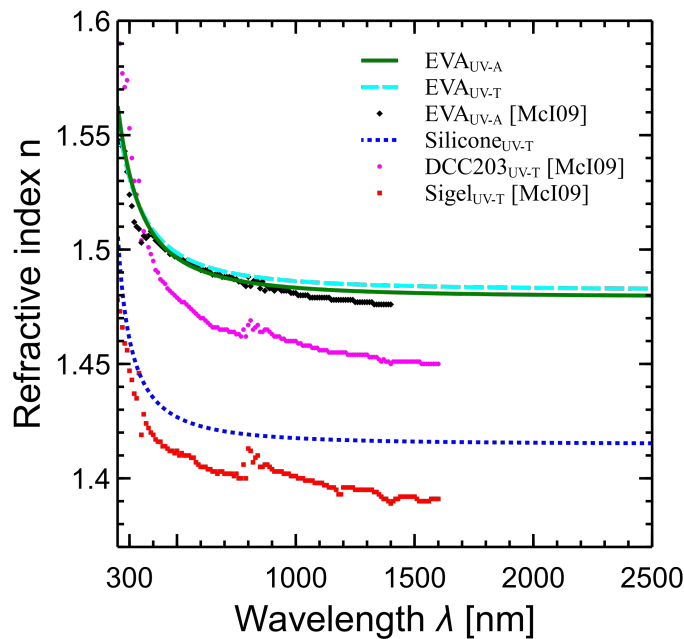
Figure 3.8: The real part of the refractive index n of the different samples compared to literature values [Mci09]. While all EVA samples' values are very similar, all silicone samples' values differ noticeably from sample to sample.

Figure 3.8 shows the real part of the refractive index n of the different samples compared to literature values [Mci09]. One can clearly see how ellipsometry enables smother curves than the ones derived from reflection and transmission measurements of encapsulants between two slabs of glass. (The same can be seen in the appendix A for the reflection and transmission measurements of encapsulants between two slabs of glass conducted in this work.)

All EVA samples' values are very similar, declining from $n(250\,\text{nm}) \approx 1.56$ to $n \approx 1.48$ in the NIR where it is nearly constant up to at least 2500 nm. All silicone samples' values differ noticeably from sample to sample. The reason for this is that each sample is a different type of silicone and in contrast to EVA they also differ in the real part of the refractive index.
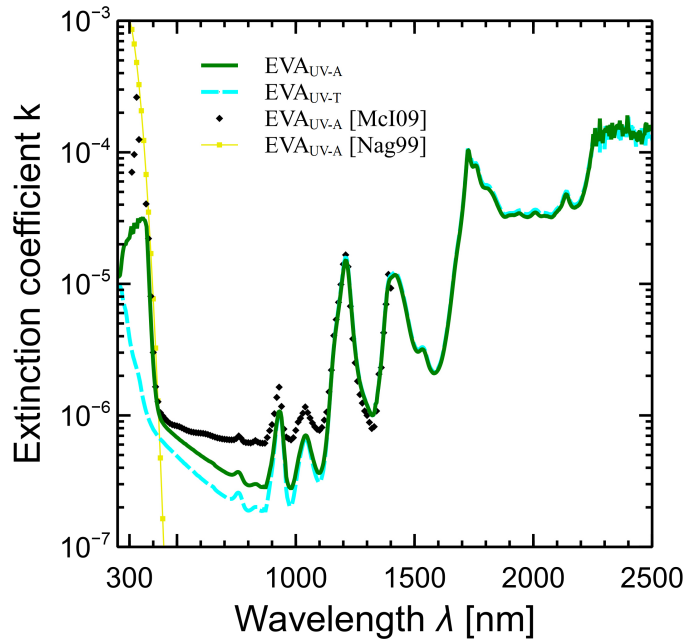
Figure 3.9: The extinction coefficient k of the different EVA samples compared to literature values [Mci09; Nag99]. All UV absorbing EVAs (EVA$_{UV-A}$) have a similar increase at 380 nm. UV transparent EVA (EVA$_{UV-T}$) has lower absorption until 1150 nm.

Figure 3.9 shows the extinction coefficient k of the different EVA samples compared to literature values [Mci09; Nag99]. The new UV transparent EVA (EVA$_{UV-T}$) has lower absorption until 1150 nm, above that wavelength EVA$_{UV-T}$ has the same extinction coefficient as EVA$_{UV-A}$. All UV absorbing EVAs (EVA$_{UV-A}$) have a similar increase at 380 nm. Above that our samples have the same absorption peaks as [Mci09], indicating good agreement.

Figure 3.10 shows the extinction coefficient k of the different silicone samples compared to literature values [Mci09]. As for the real part of the refractive index all three silicone types differ significantly, expect for the three peaks between 1100 nm and 1600 nm. The silicone$_{UV-T}$ measured in this work has a higher extinction coefficient than the values from literature the most likely explanation is that the silicone types are simply different in their optical properties.

Again all the values can be found tabulated in the appendix B.3.

3.3.1 Reflectivity of colored silicone back encapsulation materials

There is growing interest in having PV modules in different colors to accommodate architectural design wishes or regulatory compliances for historically relevant town building. One concept for coloring PV modules [Vog14] adjusts the cells ARC to let the cells appear
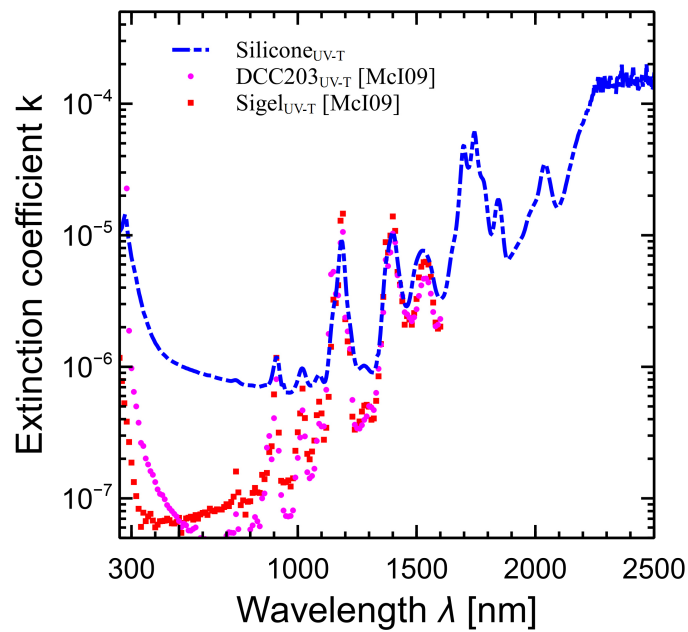
Figure 3.10: The extinction coefficient k of the different silicone samples compared to literature values [Mci09]. As for the real part of the refractive index all three silicone types differ significantly.

in the desired color in combination with colored encapsulation materials, which are placed below the cells, to color the inter cell gaps.
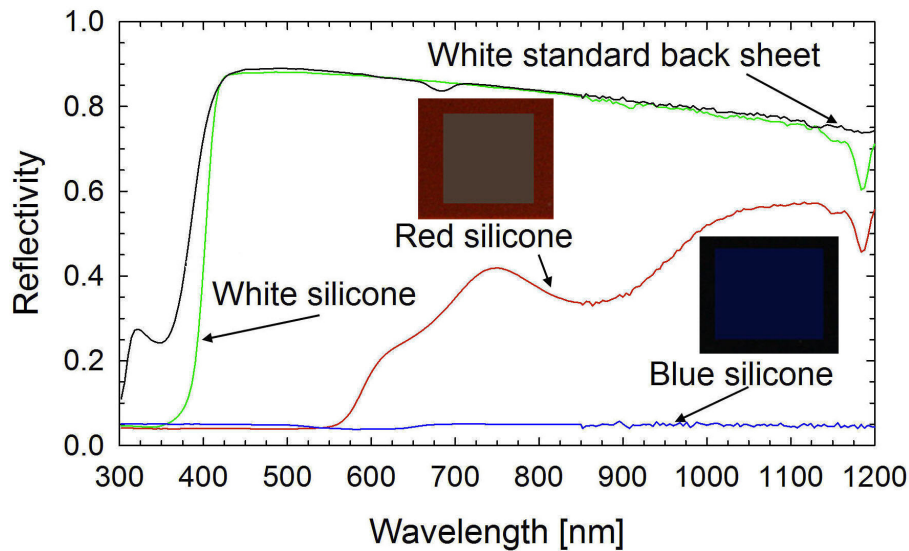
Figure 3.11: Measured reflectivity of colored SilTRUST® encapsulation materials, which are placed below the cells, to control the change the color of the inter cell gaps

Such silicone based colored SilTRUST ® encapsulation materials are measured with the reflection measurement method from sec. 2.2.1. The results are displayed in Fig. 3.11. The white silicon has reflectivity similar to a white standard back sheet. While the blue-black silicone reflects around 5% of the incoming light for all wavelength, the red silicone reflects about 40% of the light between 700 nm and 900 nm and increases up to 60% around 1100 nm.

An advantage white back encapsulation materials have is that the reflection happens on the same level as the cell's rear side and not about 450 µm as with the back sheet and transparent back encapsulation materials.

3.4 Optical properties of silicon

One of the main goals when creating a silicon (Si) solar cell is to absorb as much light as possible with in the Si. In order to determine how to achieve that goal it is indispensable to determine the optical properties of Si. In literature, e. g. [Gre08; Her98; Jel92], there were many measurements of Si absorption coefficient (α_{Si}), which varied up to 30% and most measurements lacked measurement uncertainties. During my Ph.D. I collaborated with many other authors to determined the Si absorption coefficient (α_{Si}) with five different measurement techniques and its uncertainty [Sch15]. My part in this collaboration was to provide spectroscopic ellipsometry measurements of k_{Si}, which is directly related to α_{Si} via
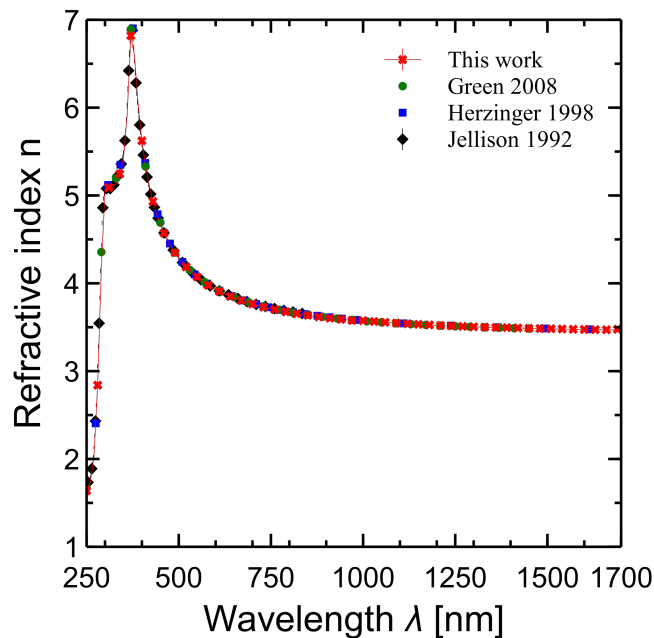
Figure 3.12: The real part of the refractive index n has a very distinct peak at about 373 nm. The biggest relative uncertainty is 0.4%, which is why the error bars are too small to be visible in this plot.

eq. 2.2. In the following I will introduce the measurements I conducted and give a very brief summary of the results gathered by our collaboration.

The ellipsometry measurements are conducted as described in sec. 2.1 for angles of incidence of 60°, 65°, 70°, 75° and 80°. The sample had a polished top side with a 1.6 nm thick thermal SiO$_2$ layer, which was modeled with data from [Her98]. The bottom side was roughened to prevent a signal from the bottom side. The thickness was determined to be 1284 μm ± 2 μm. A transmission measurement of an identical sample except for the bottom side, which was polished, was conducted by [Pee14] the results are used to increase the accuracy for wavelengths above 930 nm. All data is fitted by the Monte Carlo method based data analysis approach developed in sec. 2.1.2.

The real part n of the refractive index (see Fig. 3.12) is in very good agreement between our measurements and literature. It increases in the UV from 1.64 at 250 nm to the peak of 6.87 at 373 nm, followed by a steep decrease in the VIS, which slows down considerably in the NIR where it is 3.68 at 800 nm and 3.48 at 1600 nm.

The imaginary part k of the refractive index is illustrated in Fig. 3.13. Jellison [Jel92] (black diamonds) only provides data below 840 nm, where the uncertainties he determined are at 75% relative. The relative uncertainties our ellipsometry measurements also increases from below 10% at 750 nm to about 30% at 850 nm before reaching 80% at 950 nm before the sample transmits enough light for the transmission measurement data to decrease

Figure 3.13: The imaginary part k of the refractive index. he relative uncertainties our ellipsometry measurements also increases from below 10% at 750 nm to about 30% at 850 nm before reaching 80% at 950 nm before the sample transmits enough light for the transmission measurement data to decrease the uncertainty rapidly at 980 nm.

the uncertainty rapidly at 980 nm. At 1200 nm or $k \approx 2 \times 10^7$ the relative measurement uncertainty increases again, here the measurement is limited by the uncertainty of the transmission measurement. Here, electro and photo luminescence can be used to gather more accurate data (cyan pentagons) as described in [Sch15]. Therefore the collaborated k-values and the n-values of this work (since n-values are not determined by the collaboration) will be used in the following, both are in the appendix table B.6.

## 3.5 Optical properties of silicon-nitride

The silicon cell's operates more efficiently, if it's surface is passivated to reduce surface recombination and if the surface has low reflectivity due to an ARC. Plasma-deposited silicon nitride films (SiN) are the most commonly used material for this, since it offers very good surface passivation combined with a refractive index tunable between $n = 1.9 - 2.9$ at 633 nm, which is the wavelength usually used for optimizing the SiN layer [Dos97; Dut12; Nag99].

In this section, the measurement results of three different SiN layers are presented and discussed.

The samples consists of a SiN layer on the polished top side of a Si wafer with a roughened bottom or rear side. Spectroscopic ellipsometry measurements (details see sec. 2.1.1) were conducted for angle of incidence of 65°, 70° and 75°. Transmission measurements are not conducted for two reasons first the Si is only transmitting light above 980 nm and second the rough rear side changes the transmission angle. However, the roughness of the rear side prevents the specular reflection at the rear, which is helpful with the ellipsometry measurement, since only light reflected at the front of the wafer is detected.

The sample with $n(633 \text{ nm}) = 2.09$ is analyzed with all three data analysis techniques (details see sec. 2.1.2) to find the one most suitable. The wavelength-by-wavelength fit (yellow crosses) and the Monte-Carlo method based fit (green squares) surround the model fit (green solid-line) for the real part of the refractive index shown in Fig. 3.14. The model-fit has an MSE of 1.4 using the Tauc-Lorentz Oscillator model as proposed by [Jel96] for this material. All three data analysis methods are in good agreement with each other for the real part of the refractive index, while the Monte-Carlo based method provides error bars. Our measurement results are similar in shape and value to the literature data [BF11; Dut12].

For the extinction coefficient k shown in Fig. 3.15, however, the methods result in different k-values. The wavelength-by-wavelength fit (yellow crosses) and model fit (green solid-line) both start at $k(300\text{nm}) \approx 0.1$ and decline similar to $k(450\text{nm}) \approx 0.01$, after this wavelength the model fit declines faster than the wavelength-by-wavelength fit. Additionally, the wavelength-by-wavelength fit suggest $k \approx 0.004$ above 900 nm, while the model fit has $k = 0$. The newly developed Monte-Carlo based method agrees with the slower decline of the wavelength-by-wavelength fit at shorter wavelengths, but also shows that the measured extinction coefficient values in the NIR region have more than 100% measurement
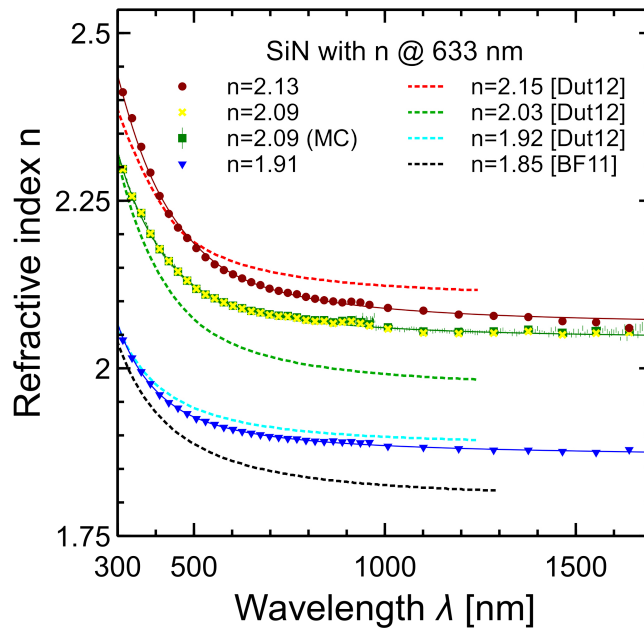
Figure 3.14: Compares the real part of the refractive index of the measured SiN samples(symbols and solid lines) with values from literature(dashed lines). The SiN layers are named after their refractive index value at 633 nm.

uncertainty. Mr. Baker-Finch kindly told me, that he is not certain in the increase of the extinction coefficient above 500 nm.

Thus in future work transmission measurements are necessary to determine the SiN extinction coefficients more accurately. Until then I use the Tauc-Lorentz Oscillator based model fit according to [Jel96] to determine n and k, but employ the wavelength-by-wavelength fit as an indicator for the starting values. This prevents an cross over as between the k-values $n = 2.15$(red dashed-line) and $n = 2.03$(green dashed-line) from [Dut12]. In my experience such cross overs are a result of suboptimal model fits due to high measurement uncertainties for k-values, which signifies the need for more accurate measurements, e.g. transmission measurements on a different substrate.

The overall trend of all values shows, that a higher n-value is coupled to a higher k-value for SiN layers. Therefore, one has to find a compromise between minimizing parasitic absorption in the SiN layer and the anti reflective properties tied to the n value, when optimizing a solar cells optical properties.

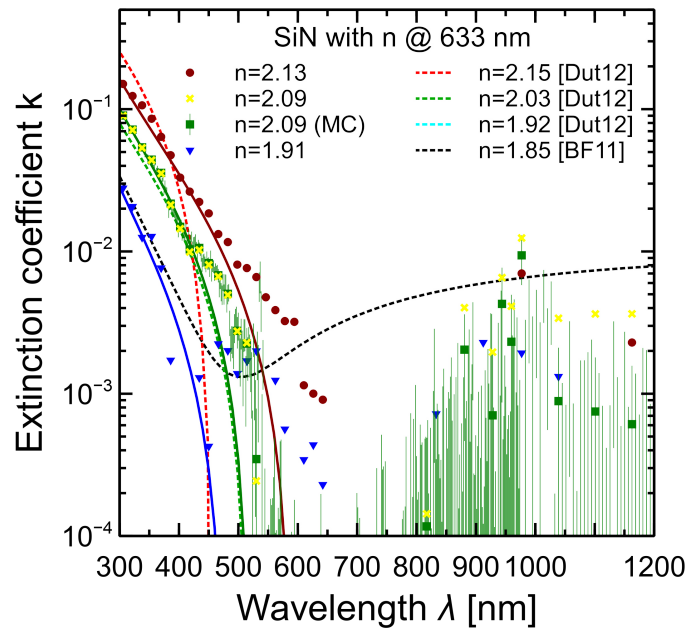The values of the model-fit data can be found in tabulated form in the appendix B.5.

Figure 3.15: Compares the extinction coefficient of the measured SiN samples(symbols and solid lines) with values from literature(dashed lines). The newly developed Monte-Carlo based method(green squares) shows that the measured extinction coefficient values in the NIR region have more than 100% measurement uncertainty. A higher n-value is linked to a higher k-value for SiN layers.

3.6 Optical properties of aluminum-silicon-eutectic as rear reflector in solar cells

Most industrial type solar cells use a full area aluminum rear side. It serves two purposes: first, it is the rear contact and second, it is a reflector for the light, thus enhances the light trapping. In newer cell concepts such as "PERC"-cells, where localized rear contacts are used to reduce recombination at those contacts, there is often an full area aluminium mirror behind the contacts and a passivation layer to increase the reflectivity at the rear side. In the following the optical constants of this rear side are determined.

The Al is fired onto the Si at temperature between 840-900°C [Nag02, Ch. 11.2], this leads to a Ai-Si-eutectic at the interface of both media. This eutectic is a major factor when describing the rear side of solar cells, which is very important for cell properties above 950 nm, where the Si starts to transmit light (see Sec. 3.4). The Ai-Si-eutectic is difficult to measure directly, since the Si is on top of it, but in literature it is known [Gra05; Jag10], that the eutectic consists of about 12% weight total of Si and 88% weight total of Al. The optical properties, however, are dependent on the volume fraction which is $c_{Si} = 13.6\%$ volume fraction for Si and $c_{Al} = 86.4\%$ volume fraction for Al.
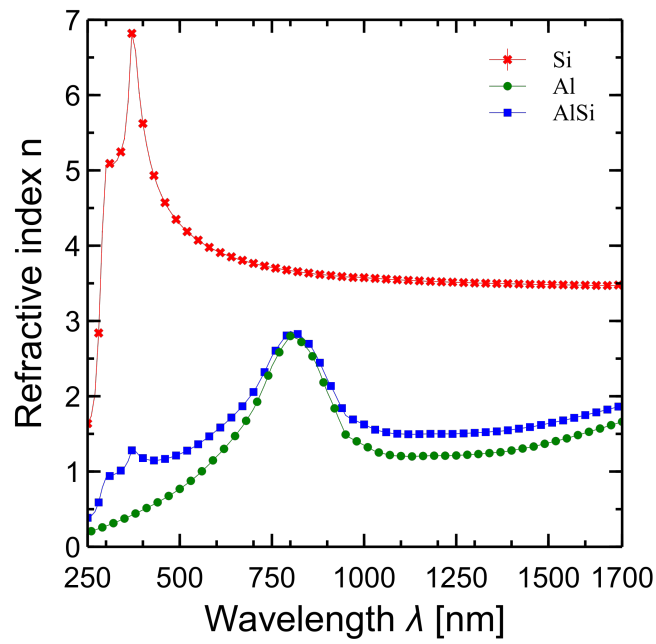
(a) The real part of the refractive index of Si, Al and the Al-Si-eutectic.
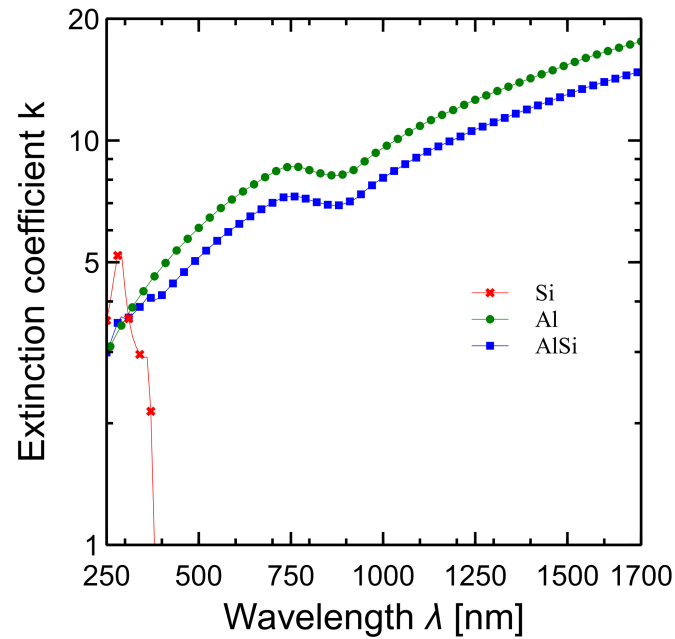
(b) The extinction coefficient of Si, Al and the Al-Si-eutectic.

Figure 3.16: The optical properties of the Al-Si-eutectic, are dependent on the volume fraction, which is $c_{Si} = 13.6\%$ for Si and $c_{Al} = 86.4\%$ for Al. An effective medium approach is used to determine the Al-Si-eutectics optical properties.

Hence an effective medium approach is used to determine the Al-Si-eutectic's optical properties from

$$\hat{n}_{\text{AlSi}} = c_{\text{Si}} \times \hat{n}_{\text{Si}} + c_{\text{Al}} \times \hat{n}_{\text{Al}}. \tag{3.4}$$

The results are shown in Fig. 3.16 as blue squares. The aluminum optical data (green circles) was taken from [Shi80]. While the silicon optical data (red crosses) is from table B.6 as described in the previous section.

The real part of the refractive index of the Al-Si is similar in shape to the Al, but always higher than the Al refractive index, but well below the Si. Both have their maximum at 800 nm with $\hat{n}_{\text{AlSi}} \approx 2.86$ and $\hat{n}_{\text{Al}} \approx 2.8$. In the UV Al-Si has a secondary peak, which corresponds in wavelength with the Si peak at 373 nm.

In contrast to all other materials presented in this chapter Al and Al-Si have a higher extinction coefficient k than real part of the refractive index n, which means that the extinction coefficient has to be included in any calculation of the Al-Si surface reflective. Below 300 nm Si has the highest absorption, thus in this region Al-Si has a slightly higher k_{AlSi} than Al. Above 300 nm k_{AlSi} is always slightly below k_{Al} above 450 nm in wavelength $k_{\text{Si}} < 0.1$ which means that the Al-Si extinction coefficient is mainly determined by c_{Al} and k_{Al}.

Therefore $\hat{n}_{\text{AlSi}}$ will be used to describe the optical properties of the Al rear side of a solar cell, the values depicted here are in the appendix table B.7 for further use.

3.7 Optical properties of back sheets

The back sheet is the bottom layer of a typical industrial type PV module. Its main purposes are protection of the cells from external forces, electrical isolation and reflection of light onto the cells.

The last goal is best achieved if back sheet reflects the light such that the light is reflected by the back sheet in an angle $\theta_R > 41.8° \approx \arcsin(n_{air}/n_{glas})$ to cause total reflection at the air-glass interface at the front side of the module to be internally reflected onto the cells. Additionally a high surface reflectivity for all wavelengths between 300 nm and 1200 nm is desired, which let's most used back sheets appear white to the human eye.

Figure 3.17 shows the reflection of various commercially available white back sheets versus the wavelength in nm. The measurements are conducted with a Varian Cary as described in sec. 2.2. All back sheets in Fig. 3.17 have reflectivity below 0.1 in the UV and above 0.7 in the VIS-NIR region.

The straight forward approach is to measure the back sheets as fabricated in surrounded by air, which was done for the "PYE 3000" (blue circles), "T2441" (red diamonds) and for the "PV2111" (purple triangles) where the values where extracted from a plot in [RG07]. Below about 600 nm the "PYE 3000" has the highest reflectivity, above this wavelength the "PV2111" has the best reflectivity.
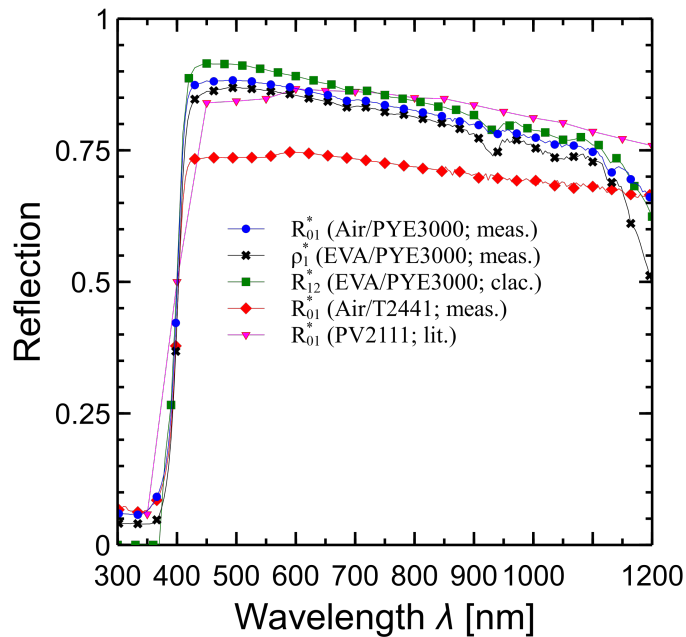
Figure 3.17: Due to the non-specular reflection an integrating sphere is used. Note that most measured back sheets are surrounded by air, while one sample (black crosses) is covered by an EVA layer of about 500 µm and the reflectivity of the EVA/back sheet interface is extracted using eq. 2.19. The literature comparison was extracted from a plot in [RG07].

However, in the solar cell module the reflection at the back sheet happens surrounded by encapsulation material (usually EVA) and not air. To determine the influence of the EVA, one back sheet sample has an about 500 µm thick EVA (UV-absorbing) layer on top of the back sheet. The reflection of the two layer system (black crosses) is lower than the same back sheet surrounded by air (blue circles). The reflectivity of the EVA/back sheet interface R_{12}^* (green squares) is extracted using eq. 2.19. The result shows that the reflectivity at the relevant EVA/back sheet interface is higher than the reflectivity of the usually measured air/back sheet interface (for the PYE 3000 back sheet) by about 0.04 in the VIS-NIR. Consequently, a back sheets optical performance should be evaluated with a known encapsulation material on top, so that the interfaces performance can be evaluated. For the further use there is a table with the values of the EVA/PYE 3000 interface in the appendix B.9.

3.8 Conclusion

In this chapter the optical constants of the most optically relevant components of a typical Si wafer based solar cell module were determined applying the measurements methods from Ch.2. The final results can be found in a set of tables B in the appendix.

In comparison with the knowledge available in literature the most significant additions are the two semi-empirical models for the extinction coefficient of soda-lime glasses as a function

of iron concentration, the characterization of UV transparent EVA and determining the back sheets reflectivity with in the EVA.

The all results of this chapter are important input parameters for the simulation models discussed in part II of this thesis.

PART II

Simulations of complete solar cell modules

CHAPTER 4

Ray tracing of entire solar cell modules and optical loss analysis

The schematic and the geometrical details of the standard module simulated in this chapter is shown in Fig. 4.1. It consists of a 4 mm thick float glass, having an anti-reflection-coating (ARC) on top, with 450 µm EVA encapsulant above and below the 10×6 monocrystalline standard Si cells, and with a rear side covered with a white back sheet. The gap between neighboring cells is 3 mm, between the outermost cells and the frame edge it is 10 mm. Each cell has a standard SiN_x ARC layer, a random pyramid texture, a pseudo-square shaped wafer with an area of 239 cm^2, a full-area Al back contact, and is 170 µm thick.
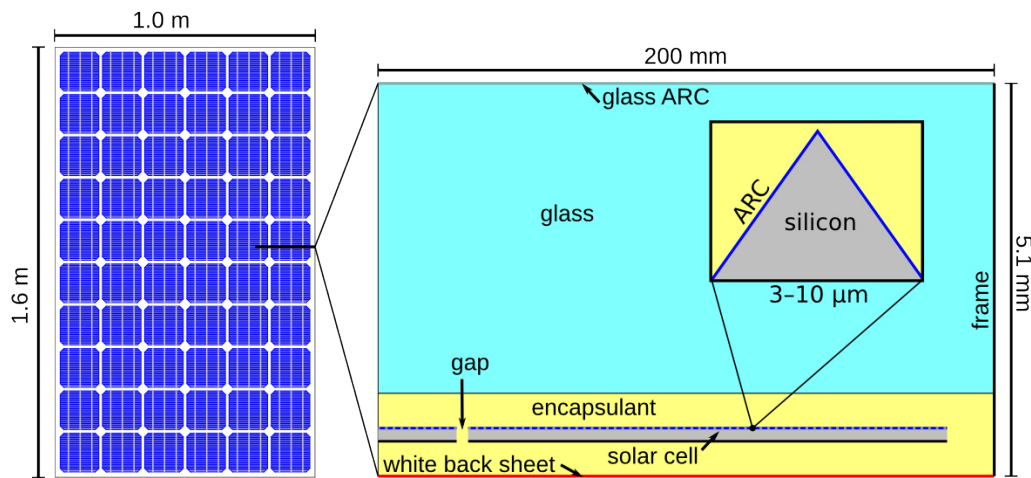
Figure 4.1: Schematic and dimensions of a standard PV module: top view (left) and a cross section (right). This illustration is taken from [Win15].

The optical properties of a complete module are too complicated to be described analytically. Therefore a ray tracing approach with a good compromise between accuracy and speed is chosen. The ray tracing is done in three dimensions using the ray tracing framework DAIDALOS [Hol13]. While there exist a number of ray tracers for solar cells such as [Bre93], very few of them are suitable to ray trace geometries of solar cell modules such as the EXCEL based TRACEY [Mci09; Mcl10] and the analytical simulation tool to characterize different

encapsulants [Kra06]. However, DAIDALOS offers the highest flexibility in describing an
actual solar cell module's geometry, because the six orders of magnitude between the
pyramid texture and the glass geometry are handled with a multi-domain approach, where
the ray jumps back and forth as needed.
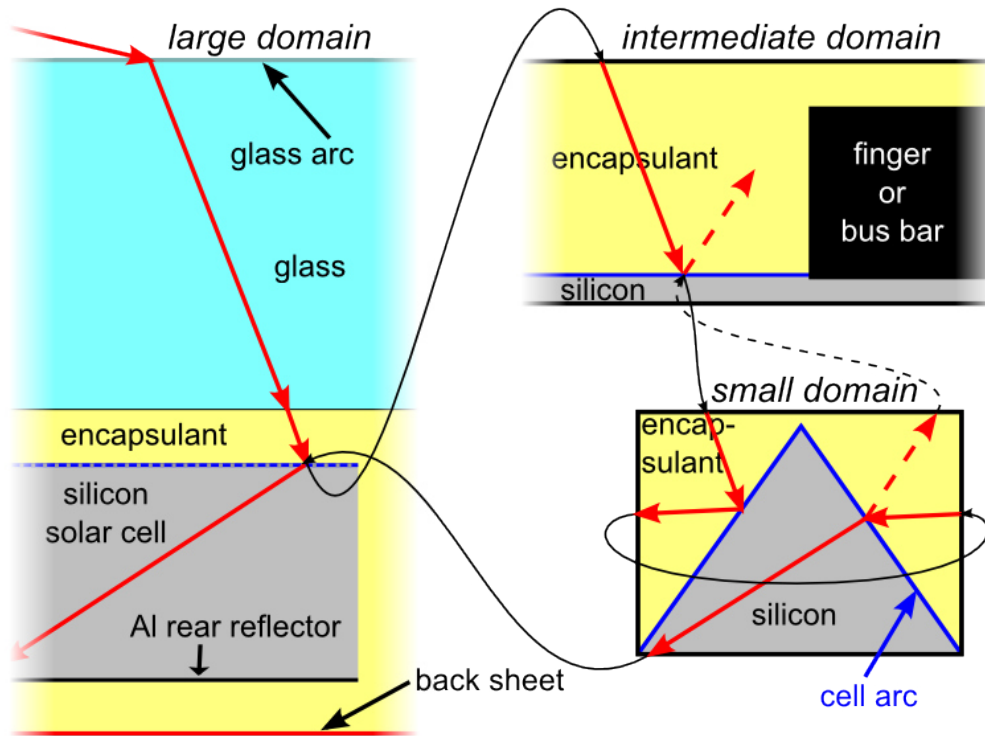
Figure 4.2: Parts of the three domains used for the ray tracing approach in this chapter.
This illustration is not to scale and taken from [Win15]. The exemplary light ray path (red
solid arrows) shows how the rays shift (black thin arrows) between the domains as needed.

The ray is traced alternating between three different simulation domains [Win15], because
a module contains features in very different lengths scales, from meters to micrometers.
The three domains are depicted in Fig. 4.2. The lightrays are generated in the large scale
domain, which is bound by the module frame and the back sheet; it contains the glass cover,
the encapsulant, and the cells. If the ray hits one of the cell interconnectors, busbars or the
five thousand front contact fingers of a module, the ray switches to the intermediate scale
domain that contains a symmetry element of the front metallization. If the ray impinges
on silicon, it is transferred to the small scale domain, which contains a single pyramid
texture of the cell. Because the approximately 10^{10} pyramids have a random distribution
of size and position, the small scale domain is positioned with a random shift, which is a
close approximation to reality [BF11].

Electrical cell properties

The electrical or semiconductor properties of the solar cells are taken into account via the collection efficiency $\eta(\lambda_i)$ of a standard industrial solar cell. A collection efficiency is the probability that an electron-hole pair, generated by a photon with wavelength λ, reaches the cell contacts and is extracted from the cell. The wavelength dependency of the collection efficiency results from the depth, within the silicon wafer, where a photon with this wavelength on average generates its electron-hole-pairs, which is close to the top for shorter wavelengths and further to the bottom for longer wavelengths.

Figure 4.3 depicts two collection efficiencies as numerically modeled with Sentaurus. An older industrial Al-BSF type silicon solar cell (red crosses) and a PERC silicon solar cell with improved blue response (blue circles), which are currently entering mass production.
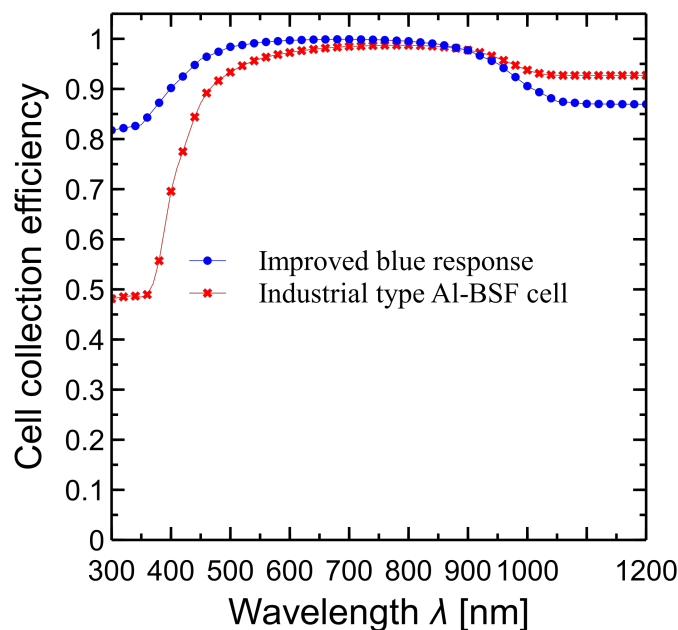
Figure 4.3: Collection efficiencies as numerically modeled with Sentaurus. For the ray tracing simulations the PERC solar cell with improved blue response is chosen, since the new module components investigated in this work most likely will be used in combination with this type of solar cell.

For the ray tracing simulations the PERC cell with improved blue response is chosen, because the new module components investigated in this work (see Ch. 3), most likely will be used in combination with this type of solar cell.

The ray tracing yields the absorption $A_{\mathrm{comp}}(\lambda_i)$ and reflection $R_{\mathrm{comp}}(\lambda_i)$ value for each module component. Multiplying the absorption of the silicon $A_{\mathrm{Si}}(\lambda_i)$ with the standard am1.5g spectrum [Gue01] $J_{\mathrm{am1.5g}}(\lambda_i)$ leads to photo-generated current density $J_{\mathrm{gen}}(\lambda_i)$ of each cell. Each $J_{\mathrm{gen}}(\lambda_i)$ value is then multiplied with the collection efficiency $\eta(\lambda_i)$ of a solar cell, to include the semiconductor properties in computing the short-circuit current

density J_{sc} according to

$$J_{\text{sc}} = \int\limits_{300\ \text{nm}}^{1200\ \text{nm}} A_{\text{Si}}\left(\lambda\right) J_{\text{am1.5g}}\left(\lambda\right) \eta\left(\lambda\right) d\lambda \tag{4.1a}$$

$$\approx \sum_{\lambda_i} A_{\text{Si}}\left(\lambda_i\right) J_{\text{am1.5g}}\left(\lambda_i\right) \eta\left(\lambda_i\right)\ , \tag{4.1b}$$

with $J_{\text{am1.5g}}\left(\lambda_i\right)$ being the solar irradiance in $[\text{mA/cm}^2\ 10\ \text{nm}]$ according to [Gue01] and λ_i the wavelength in 10 nm steps over the interval from 300 nm to 1200 nm.

To compare the simulated losses with the losses in an ideal module, this procedure is repeated with the absorption and reflection of all the other components in the module, however with the cell collection efficiency set to one $(\eta(\lambda_i) = 1)$, in order to investigate the optical losses independent of the cell's electrical properties. The result is the lost generation current density per module area with the photo generation current in the am1.5g spectrum having 46.7 mA/cm^2 in the simulated wavelength range between 300 nm and 1200 nm.

Typical simulation parameters

The light source, simulates the vertical incidence in the wavelength range between 300 and 1200 nm for 10 000 rays every 10 nm wavelength at random positions in all simulations in this chapter. The components material data used as default are listed in table 4.1:

Table 4.1: Default material parameters and references used in this chapter, unless specified otherwise.

Component	Material	Description in	Table
Glass ARC	100 nm porose glass layer	Sec. 3.2	Tab. B.1
Glass	M1: Fe$_2$O$_3$ wt = 0.01‰	Sec. 3.1	Tab. B.2
Encapsulant	EVA$_{\text{UVT}}$	Sec. 3.3	Tab. B.3
Cell ARC	75 nm SiN$_{2.09}$	Sec. 3.5	Tab. B.5
Front metalization	Silver	[Pal85, p. 350-357]	Tab. B.4
Wafer	Silicon	Sec. 3.4	Tab. B.6
Cell rear side	Al-Si-eutectic	Sec.3.6	Tab. B.7
Frame	Aluminum	[Shi80]	Tab. B.8
Back sheet	EVA/Back sheet interface	Sec. 3.7	Tab. B.9

The dimensions of the components are described in Fig. 4.1.

Electrical module properties

Because the cells are connected in series in a standard 60 cell module, the module power is simulated with the circuit simulator LTSPICE IV from Linear Technology, considering all ribbon and interconnector resistances. The cells' J_{sc} values are adjusted according to their position in the module: our ray tracing analysis shows that J_{sc} of the cells at the edge of the module is enhanced by a factor of 1.0126 and by 1.026 in a corner cell, compared to the cells in the interior. This effect is caused by internal reflection from the white back sheet at the corner and edge positions. Due to the series interconnection of the cells, however, only part of these J_{sc}-gains can be exploited in the module.

4.1 Influence of the glass ARC

In this section the antireflection coating (ARC) on top of the glass is varied. The optical losses in [mA/cm^2] are illustrated in Fig. 4.4: The left bar shows the reference module with the measured ARC on top of the glass from section 3.2, the middle bar shows a module with an ARC consisting of MgF$_2$. Both ARCs have a thickness of 100 nm. The right bar shows a module without an ARC on top of the glass.
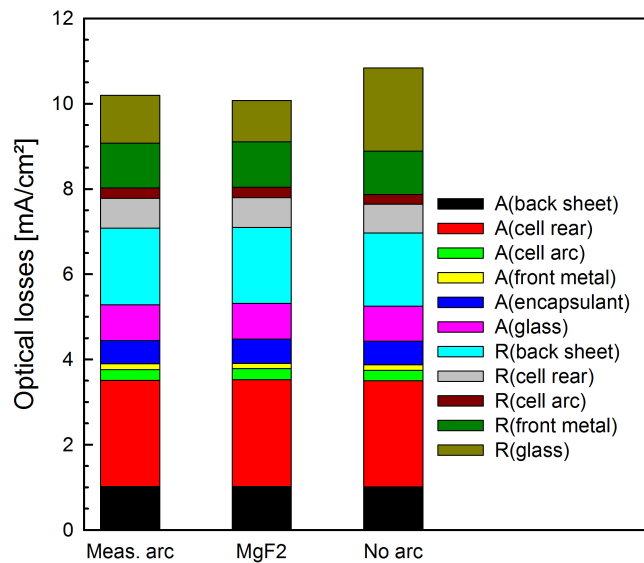
Figure 4.4: Simulated optical losses of the reference module with the measured ARC on top of the glass from section 3.2 (left), with a MgF$_2$ based ARC (middle), without an ARC (right). The reference module has a peak power of 290.6 W, the MgF$_2$ increases the power output by 1 W, and having no ARC lowers the power output by 5.2 W.

The ARC of the glass mainly influences, how much light is reflected from the glass surface, which is shown as the olive area at the top of every bar. The MgF$_2$ based ARC increases a middle cell's current by 0.3%, while having no ARC decreases the cell's current by 1.8%. Note how the other losses in the right bar are all slightly smaller, since all other module

components interact with less light due to the increased reflection at the glasses surface. This demonstrates how the optical losses in a solar cell module are coupled, thus requiring a numerical approach for quantifying the various optical losses.

Using LTSPICE IV, the peak module power output of the reference module is 290.6 W, while the MgF_2 based ARC increases the power output by 1 W, and having no ARC lowers the power output by 5.2 W.

4.2 Loss in the glass

In this section the extinction coefficient of the module's front glass is varied according to the models developed in sec. 3.1. The n-value and the thickness (4 mm) of the glass remain the same for all simulations. Additionally the simulations are conducted with an UV-absorbing EVA, since the results of this section were submitted as paper [Vog15b], before the optical constants of the UV-transmitting EVA were measured.
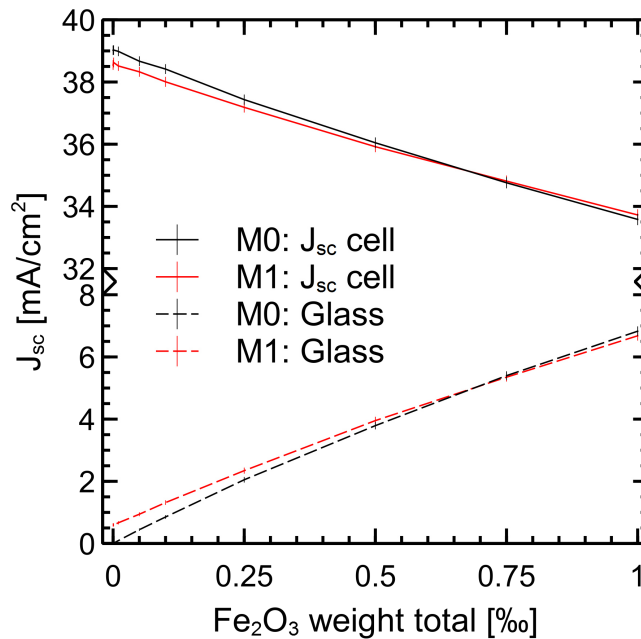
Figure 4.5: Simulated short-circuit current density J_{sc} of a cell in the middle of the standard module in dependence of the amount of iron in the front glass (top), and the current lost by parasitic absorption in the glass (bottom), for both models in sec. 3.1. The difference between Model 0 and 1 is always less than 0.5 mA/cm^2 in J_{sc}.

Fig. 4.5 shows the simulated short-circuit current density J_{sc} of a cell in the middle of the standard module in dependence of the amount of iron in the front glass (top), and the current lost by parasitic absorption in the glass (bottom). Note that, with reduced iron content, the parasitic absorption losses decrease slightly faster than J_{sc} increases. This is a result of increased optical losses in other parts of the module (due to the increased illumination caused by the higher transmission of the glass). The two losses that increase

the most are the absorption in the encapsulant and the reflection at all components below the glass. This non-linear behavior demonstrates that, for obtaining precise results, it is necessary to include all module components into ray tracing simulations.

The J_{sc} difference between model 0 (assuming that all absorption is caused by iron) and model 1 (assuming a background of coloring agents) is always less than 0.5 mA/cm^2. The uncertainty of the simulation due to the Monte-Carlo algorithm is slightly below ±0.2 mA/cm^2 for all simulations shown here, which means that the difference in J_{sc} for Fe_2O_3 below 0.01‰ for both models is below this simulation uncertainty.
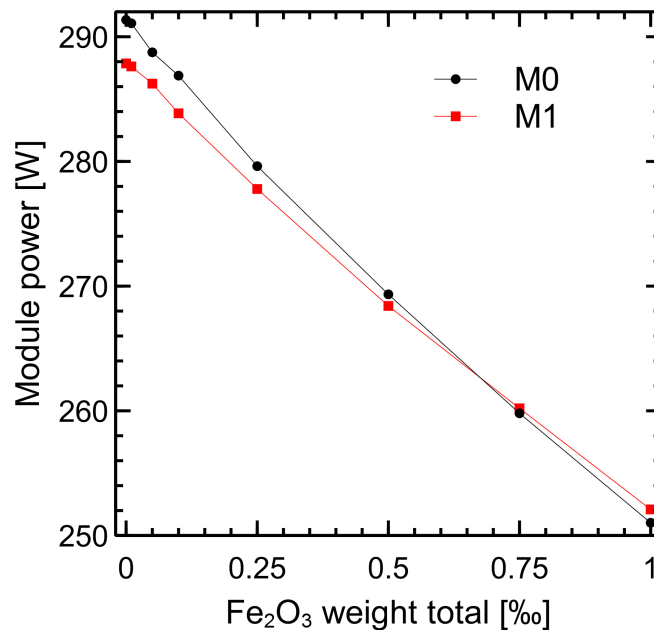
Figure 4.6: The dependency of the module power output on the iron concentration in the glass of the standard module. The decline with increased Fe_2O_3 content is significant, as expected: both models predict an 1.5% or 4 W decrease in module power for Fe_2O_3=0.1‰ and a decrease by about 13% or 40 W for Fe_2O_3=1‰.

Fig. 4.6 shows the dependency of the module power output on the iron concentration in the glass. If the glass does not absorb any light (model 0 and $Fe_2O_3 = 0$), the chosen module produces 291 W. If we assume a background of coloring agents (model 1 and $Fe_2O_3 = 0$), the module produces about 3.5 W less power. The decline in module output power with increased F_2O_3 content is very similar for both models: by about 1.5% (4 W) for $Fe_2O_3 = 0.1$‰ and by about 13% (40 W) for $Fe_2O_3 = 1$‰. The change in the first case, $Fe_2O_3 = 0.1$‰, is very small, because the module power output is limited by other optical losses: mainly by the reflection at the different module components, followed by absorption in the EVA encapsulant and in the rear metallization. These findings may be experimentally verified with the method proposed in [Kho12].

These findings are not only useful for evaluating the module power losses for glasses with

iron contamination, but also for evaluating the necessary resources of high-purity raw materials for photovoltaic soda-lime glass manufacturing. Such high-purity resources are limited and may play a role in global up-scaling of photovoltaic power.

4.3 Influence of the encapsulation

In this section the encapsulation material is varied with the optical properties measured in section 3.3. The encapsulant is placed in between glass and cells, cells and back sheet and in the inter-cell gaps. The optical losses are illustrated in Fig. 4.7. The left bar shows the reference module with the UV-transmitting EVA (EVA_{UV-T}), the middle bar shows a module with the UV-absorbing EVA (EVA_{UV-A}), while the right bar shows a module with the UV-transmitting silicone (Sil_{UV-T}). All three show the optical losses of a middle cell.
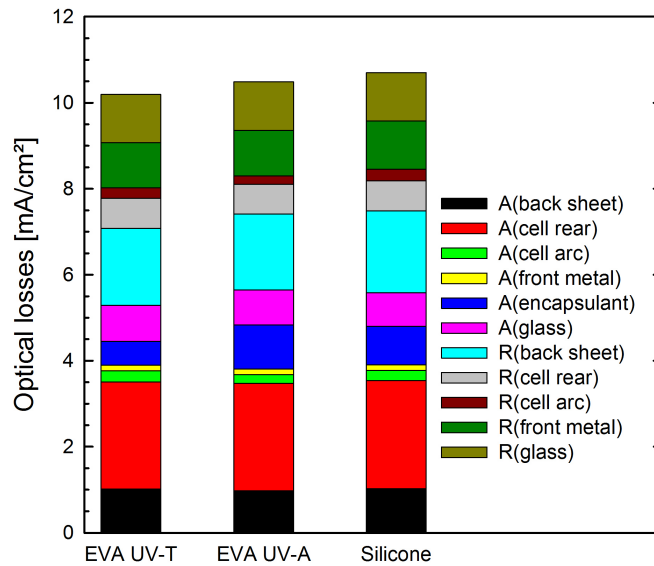
Figure 4.7: Simulated optical losses of a middle cell. Left bar: in the reference module with the UV-transmitting EVA (EVA_{UV-T}). Middle bar: a module with the UV-absorbing EVA (EVA_{UV-A}). Right bar: a module with the UV-transmitting silicone (Sil_{UV-A}).

The encapsulation material mainly influences how much light is absorbed in it, which is shown as the dark blue area in every bar. How well the optical constants of the encapsulation materials match the ones of the glass also determines how much light is reflected at the glass encapsulant interface. However, the simulated materials match sufficiently enough that these reflection losses are only about 0.05 mA/cm² for silicone and about 0.003 mA/cm² for EVA, thus too small to be visible in Fig. 4.7. Compared to the reference module with EVA_{UV-T}, the middle cells in the module with EVA_{UV-A} have 0.7% lower J_{sc} and the ones in the module with Sil_{UV-T} have 1.4% lower J_{sc}. However, some literature references measured different kinds of silicone, some of these would produce better results than the EVA_{UV-T} simulated here [Ket08; Mci09].

Using the LTSpice IV to calculate the peak module power results in a decrease of 2.1 W for a module with EVA_{UV-A} of 4.2 W for a module with Sil_{UV-T}, both in comparison to the reference module with EVA_{UV-T} and a peak power output of 290.6 W.

4.4 Influence of the cell ARC

In this section the optical properties of the silicon nitride coating on top of the solar cells are varied with the materials measured in section 3.5. The optical losses in $[mA/cm^2]$ are illustrated in Fig. 4.8. The left bar shows a module's middle cells with 82 nm $SiN_{1.91}$ (where $1.91 = n(\lambda = 633$ nm$)$), the middle bar shows a cell in the reference module with 75 nm $SiN_{2.09}$ and the right bar a module's middle cells with 73.6 nm $SiN_{2.13}$. The SiN thickness is adjusted to keep the optical thickness $(d \times n)$ constant, thus the reflection minimum at the same wavelength.
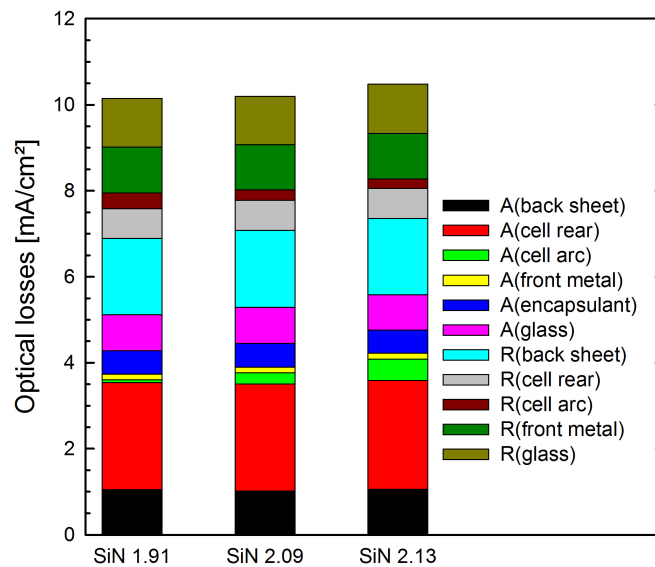
Figure 4.8: Simulated optical losses in a middle cell. Left bar: a module with cells with 82 nm of SiN_x with $n = 1.91$. Middle bar: with 75 nm of SiN_x with $n = 2.09$. Right bar: one with cells with 73.6 nm SiN_x with $n = 2.13$.

The cells' ARC mainly influences the reflection at top side of the cells (brownish-red in every bar) and the absorption in the ARC (light green in every bar). Due to the lowest absorption, the SiN_x with $n = 1.91$ produces 0.1% more J_{sc} than the reference module with a SiN_x with $n = 2.09$, while the SiN_x with $n = 2.13$ lowers the current by 0.8%. However, since the SiN_x also serves as a passivation layer, an SiN_x with about $n = 2.09$ (at $\lambda = 633$ nm) is usually chosen [Dos97; Dut12; Nag99].

Using the LTSpice IV to calculate the peak module power results in a decrease of 2.2 W for a module due only considering optical losses using this SiN_x with $n = 2.13$ instead of the SiN_x with $n = 2.09$.

4.5 Colored PV modules

There is growing interest in having colored PV modules for architectural designs. In addition many countries have legislate regulatory compliances for installing solar panels on roof tops in historically relevant town areas; one of the compliances is requiring modules to be similar in appearance to roof tiles. However, coloring solar cells and the gaps between them is commonly thought to cause considerable performance losses.

In this section PV modules that look either completely dark-blue or completely red as roof tiles are ray traced. This is achieved by placing the cells on colored silicone back encapsulants and adjusting the cell's ARC thickness.

The red cells have an ARC with an increased thickness of 195 nm, all the other modules have blue cells with standard ARC. The calculation of the color of the cell [Che12] is updated by including silicone above the cell instead of air. The higher refractive index n of silicone broadens the reflectance features and thus makes the cells appear brownish instead of bright red. Similar results were published in [Vog14], however since then the ray tracing has been updated to include the front metallization as well as some newly measured materials. To achieve higher cohesiveness in this work, the simulations are redone here with the new materials and the new scheme, therefore the values of the results change slightly. In contrast to the reference module as described in table 4.1 the colored back encapsulants from Sec. 3.3.1 directly below the cells and the silicone from [Mci09] are used as front encapsulant since it performs optically superior to the silicone measured in Sec. 3.3.
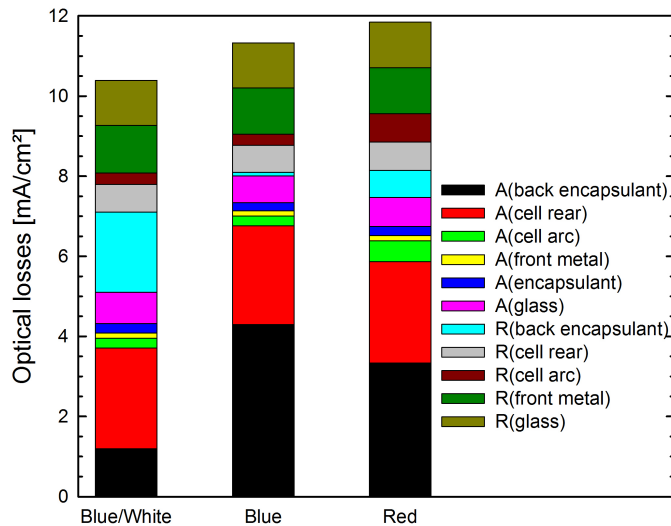
Figure 4.9: Simulated optical losses of a standard module (left bar), of a completely blue module with blue cells and blue back encapsulant (middle bar), were about 2.4% in short circuit current are lost, and of a completely red module with red cells and red back encapsulant (left bar), were about 3.9% in short circuit current is lost.

The left bar in Fig. 4.9 shows the optical losses of a module with blue cells and a white back encapsulant that serves as a reference for the differently colored modules. The middle bar

shows the optical losses of a completely blue module (blue cells and blue back encapsulant) and the right bar shows optical losses of a completely red module (red cells and red back encapsulant).

The completely blue module looses about 2.4% in J_{sc} due to lower reflectivity of the back encapsulant compared to a traditional blue and white module. Whereas the red module looses about 3.9% in J_{sc} due to the low reflectivity of the back encapsulant and also due to the increased reflectivity and absorption at the cell front, caused by the thicker ARC of the cell, which lets the cell appear brownish-red.

Using the LTSpice IV to calculate the peak module power results in a decrease of 6 W for the blue module and about 11 W for the red module. Thus the relative changes to the data published in [Vog14] are less than 1 W, but all absolute power values are decreased by 5 W due to assuming pseudo squared cells with an area of 5 cm^2 less than the full squared wafers assumed in the publication.

4.6 Influence of the back sheet

In this section the back sheet (BS) at the rear of the module is varied. The measurement of the back sheets are described in Sec. 3.7.
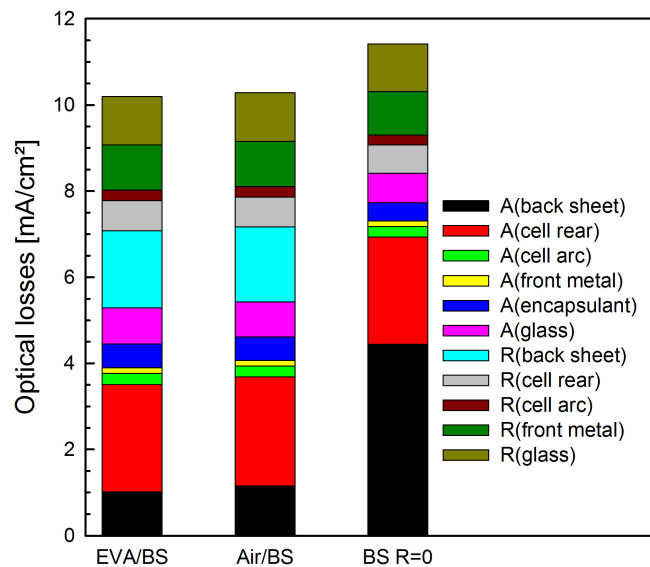
Figure 4.10: The simulated optical losses of a middle cell. Left bar: reference module with the back sheet reflectivity extracted from an EVA/Back sheet interface. Middle bar: the same situation except that this time the reflectivity as measured of the same back sheet interface in air. Right bar: having a back sheet with zero reflectivity.

The simulated optical losses of a middle cell in a module are illustrated in Fig. 4.10: The left bar shows the optical losses in the reference module with the back sheet reflectivity extracted from an EVA/Back sheet interface, while the middle bar shows the same situation

except that this time with the reflectivity as measured of the same back sheet but in air. In both cases a lambertian distribution of the reflected light ray is assumed. These results indicate that a middle cells's short circuit current is underestimated by 0.2% if the back sheet reflectivity is measured at an air interface instead of the more realistic case of an EVA/back sheet interface.

The right bar in Fig. 4.10 depicts the optical losses with the reflectivity set to zero. One can see how the absorption in the back sheet dramatically increases due to the lack of reflection, resulting in a loss of 2.8% in the middle cell's J_{sc}, for cells next to the frame this short circuit current increases even by 4%, and in case of a corner cell by 5.4%. Using the LTSPICE IV to calculate the peak module power output (taking the cell positions into account) this results in a loss of about 8 W compared to the reference module with the white back sheet.

4.7 Discussion of potential for future improvements

The reference module (see Tab. 4.1) looses about 11.7% due to absorption by module components other than silicon and about 10.6% due to light that leaves the module due to reflection. These values are in terms of the photo-current available in the am1.5g spectrum per module area in the wavelength range between 300 nm and 1200 nm.

However, some of those losses are due to the absorption coefficient of silicon being too low in the IR range above about 1000 nm (see Sec 3.4) or the wafer with 170 µm in thickness being too thin to absorb that light. To exclude these losses an idealized module consisting of only a silicon wafer with a thickness of 170 µm, exhibiting no surface reflection and perfect lambertian reflection at the rear side is assumed. Such an idealized module would operate at the so called "lambertian limit" [Yab82]. This idealized module would still loose about 6.9% of the photo current available in the am1.5g spectrum in the wavelength range between 300 nm and 1200 nm.

To exclude these losses from the simulated losses, the following calculation was proposed [Win15]: multiply each lost part of the photo generation current $J_{gen}(\lambda_i)$ with a factor of $[p_0(\lambda_i) - p_{min}(\lambda_i)]/p_0(\lambda_i)$, where $p_0(\lambda_i)$ is the number of rays in the simulation that are not absorbed in the silicon of the cell and $p_{min}(\lambda_i)$ is the number of rays an idealized module would not absorb. The sum of the losses weighted this way shows that the difference between the reference module, as discussed in this chapter, and the idealized module, are 6.9% for the absorption losses and 8.5% for the reflection losses.

Taking a look at the components that cause most of the parasitic absorption, the three biggest contributers are the cell rear metallization with $2\%_{abs}$, the glass with about $1.4\%_{abs}$ and the back sheet with $1.8\%_{abs}$. These losses could be reduced by lowering the absorption in the glass to zero (as Model 0 with Fe_2O_3=0 in section 3.1) and increasing the reflectivity of the cell's rear side and the back sheet to unity.

Taking a look at the components that cause most of this 8.5% of remaining reflection, the three biggest contributers are the back sheet with $3.5\%_{abs}$, the glass ARC with $2.1\%_{abs}$

and the front metallization with $2\%_{abs}$. These losses could be reduced by switching to back contacted cell concepts which do not require front contacts, improving the reflection characteristics of the back sheet so that all light is reflected into the cells via total reflection at the front glass cover, and lowering the refractive index of the glass ARC to about $\sqrt{n_{\text{glass}(\lambda)}}$.

Note that especially the back sheet losses are extremely dependent on the width of the cell gaps, whether or not pseudo squared wafers are used, and the distance to the frame.

4.8 Conclusion

This chapter described how ray tracing is utilized to predict a solar cell module's performance in standardized testing conditions (STC, am1.5g with 46.7 mA/cm^2 and the module cooled to 25°C) with the material measurements from Chapter 3 as inputs; a reference module then produces 290.6 W.

It was shown that having a antireflection coating on the glass increases the module power output to about 5 W compared to a module with no ARC. Having a white back sheet with the measured reflectivity increases the module power output by about 8 W compared to a module with a perfectly black back sheet (reflectivity equal to zero).

The higher UV transparency of EVA$_{\text{UV}-\text{T}}$ compared to EVA$_{\text{UV}-\text{A}}$ leads to a power increase of about 2 W due to lower parasitic absorption. Module output power declines with increasing iron content of the cover glass. Using the developed models the ray tracing analysis shows a decline between 1.5% (4 W) for an iron content equivalent to $0.1\permil$ Fe$_2$O$_3$ and 13% (40 W) for $1\permil$ Fe$_2$O$_3$.

The biggest potential for future power gains are improving the reflectivity and the scattering characteristics of the back sheet, removing or lowering the reflection of the front metalization, lowering the absorption in the glass, and improving the ARC at its surface, as we as improving the cell's rear side reflectivity with a scheme with the potential to exceed the lambertian limit such as the one disscussed in chapter 5.

Simulation of plasmonic nanoparticles

The world's energy demands are increasing rapidly. More efficient cells can considerably lower the cost of photovoltaic electricity and contribute significantly to solving these energy problems. As the optical loss analysis (see Sec. 4.7) revealed today silicon solar cells have two major optical losses the shading of the front metalization and the absorption of the full area rear side metalization. The first loss can be prevented by using back contacted solar cells, while the second loss requires an improved rear reflector which has yet to be developed. Plasmonic nanoparticles are one concept that is discussed to reduce this second loss, this concept is discussed in the following.

As single junction silicon wafer based cells are limited to an efficiency below 30% by the Shockley-Queisser limit [Sho61], third generation photovoltaics aims at surpassing this limit. It utilizes nanostructures or tandem and triple junction cells. For example, recently progress on wafer bonding between GaAs and Si has been made [Ess15]. This has opened new fabrication routes for III-V/Si dual- or triple-junction cells.

These concepts use Si as the bottom cell responsible for absorbing the NIR. However, silicon is only weakly absorptive in the wavelength range above $\lambda = 950$ nm as discussed in section 3.4. Therefore, this chapter deals with improving light trapping by means of placing very small metal particles at the rear surface of Si to enhance backscattering of light by plasmonic effects. The wavelength is set in all simulations presented in this chapter to 1000 nm. Additionally, in wafer bonding, the silicon's front surface has to be planar, thus it is not possible to use textured surfaces making it more important for the rear surface to reflect in a diffuse manner. This increases the need to have excellent light trapping for the rear side of silicon cells.

Plasmonic solar cells have been actively discussed as way to improve light trapping for solar cells e.g. [Cat11; Stu96]. The general principle is that the light hits a metallic nanoparticle (MNP) and excites surface plasmons (SP) in the MNP. SP are collective electron oscillations at a metal surface. The behavior of the SP greatly depends on the wavelength of light, the MNPs' size, shape and material, and on the surrounding media. The two ways of damping the SP are dissipation and irradiation. For particles with more than 10^5 electrons,

irradiation caused by Lorentz friction is the dominating damping channel [Jac11]. If a semiconductor is within the near-field of the MNP, a dipole coupling of the surface plasmons with the free electrons of the semiconductor is achieved. Due to this coupling a MNP on Si can scatter light more effectively than the same MNP in free space [Bec11; Jac11].

In a pioneering experiment more than two decades ago, the photocurrent of a silicon photodetector was increased by placing metal nanoparticles on its surface [Stu96]. Detailed theoretical work [Cat06] suggested that the scattering at long wavelengths is mainly a single particle effect. An investigation of the use of MNP on the front side of solar cells indicated that the cell's photocurrent can be significantly enhanced for wavelength above the SP resonance [Pil07]. However, it was observed that for wavelengths below about 600 nm the light intensity transmitted into the silicon was reduced by the MNP [Lim07]. This opposite behavior is due to a phase shift of the NP's polariability near the wavelength of surface plasmon resonance. The MNPs decrease the photocurrent in the semiconductor for wavelengths below the resonance due to destructive interference between the scattered and transmitted electromagnetic waves and increase it above the resonance due to constructive interference.

To prevent the photocurrent from decreasing at shorter wavelengths, the research in recent years focused on MNP placed on the rear side of solar cells, where all the light with short wavelengths is already absorbed. At the rear the particles serve as a rear reflector or as an addition to a mirror-like rear reflector to make the reflection more diffuse, so that more light is reflected outside of the loss cone. In [Mok11] the angular distribution of light scattered by cylindrical Ag particles surrounded by air was presented. It explains why higher cylinders scatter more light away from the semiconductor than shorter cylinders if placed at the rear. It has been demonstrated that Ag NP placed on the rear side of a solar cell compare favorably to full surface Ag-mirrors [Bec11] and that the combination of both is slightly more effective. Moreover, the combination of Ag nanoparticles and diffuse back reflectors has been reported to be more effective than an ideal Lambertian reflector [Bas12].

In the present work, Cu is chosen as metal, because Ag is expensive and its availability is rather limited. To be more realistic for fabrication, the Cu nanoparticles are placed within a SiN_x layer on the back of an Si layer. To investigate and optimize the shape of the nanoparticles, the finite element method (FEM) is chosen as simulation technique. Emphasis is given to the angle dependency of the scattered light.

5.1 Simulation model

There is no general analytical solution of the Maxwell equations known to the author for non-spherical particles or particles touching a surface of another medium. Therefore, numerical simulations are the most suitable approach to gain a better understanding of the scattering and absorption characteristics of nanoparticles. The model was inspired by [Che09].

As simulation software, the RF-module of the finite element method (FEM) simulation software COMSOL version 4.1.185 or newer is chosen. The FEM gives the freedom to discretize any geometrical shapes in a triangular fashion. The simulation domain is 3D in order to correctly determine the influence of different NP shapes. A series of test simulations revealed that at least five mesh elements per effective wavelength are necessary for sufficiently accurate simulation results. This makes the simulations very demanding on the hardware, so a server with 12 CPUs and 96 GB RAM is used.
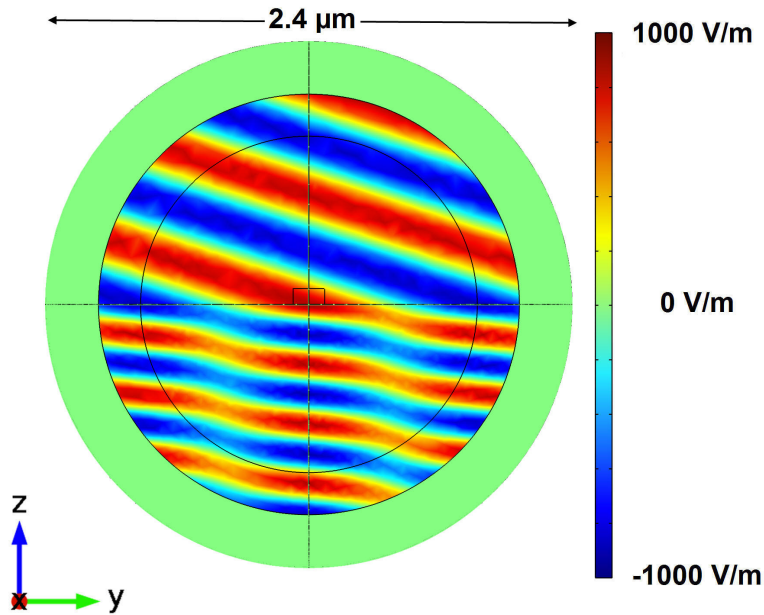
Figure 5.1: Cross-section of the three-dimensional, spherical simulation domain containing a cylindrical nanoarticle (center), Si (lower half) and SiN$_x$ (upper half), surrounded by an absorbing layer (green). Shown is the amplitude of the simulation input: the electrical field of the electromagnetic wave without nanoparticle being present, as calculated analytically by means of the Fresnel theory.

The spherical simulation domain is shown in Fig. 5.1. The nanoparticle is indicated by the small cylinder near the center. The top half is the SiN$_x$ layer, the bottom half the silicon. Light impinges from the bottom. The outer shell of the domain (indicated in green) is an absorbing layer. This prevents non-physical reflections at the outer boundaries. Hence, one single particle is simulated between two infinite half-spaces of silicon and the SiN$_x$ respectively. In this way, particle-particle interactions are neglected, which may occur at very high particle densities, and also reflection at the other surface of the SiN$_x$ layer are neglected, which can be done after the simulations by means of classical Fresnel theory.

A scattered field approach is implemented since it simplifies separating the scattered secondary light waves from the incoming primary light waves [Jin02]. In this method, the propagation of the incoming electromagnetic wave is analytically calculated in the whole simulation domain, without a NP being present, using Fresnel theory (instead of exciting the primary EM wave at the lower boundary). Its electrical field is shown in Fig. 5.1. This

primary electromagnetic wave is called the *background field* E_{back}. It is the input for the simulation.
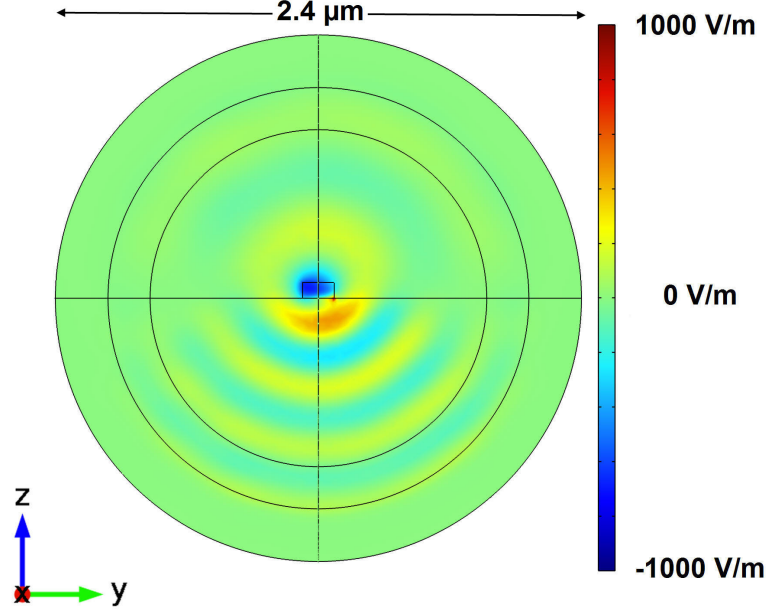
Figure 5.2: The simulation output, which is the electrical field caused by the plasmon excitement in the nanoparticle. It is obtained by solving the helmholz equation, where the incoming wave shown in Fig. 5.1 serves as input.

The coordinate system is chosen such that the wave propagates along the z-axis and that the electrical field oscillates in the direction of the y-axis (except for the special case of s-polarization in section 5.2.2). The simulation is not solved in the time-domain to avoid long computing times for weak absorption. Instead, the Helmholtz equation 5.1 is solved, which splits the excitation in a product of amplitude and frequency $\exp(i\omega t)$; consequently, the secondary excitations can be split in the same way. This makes it sufficient to solve solely the amplitude, given by

$$\nabla \times \left(\frac{\nabla}{\mu_r} \times \vec{E}_{sca} \right) - \left(\varepsilon_r - \frac{i\sigma}{\omega \varepsilon_0} \right) k_0^2 \times \vec{E}_{sca} = 0 \tag{5.1}$$

and add the frequency term afterwards. Specifically, the Helmholtz equation 5.1 is numerically solved for the response of the nanoparticle to the analytically obtained background field. The *scattered field* $\vec{E}_{sca}$ is the simulation output and defined as:

$$\vec{E}_{sca} = \vec{E}_{tot} - \vec{E}_{back} \tag{5.2}$$

An example is shown in Fig. 5.2. The Maxwell equations are linear in respect to the electrical field, so the principle of superposition can be applied, e.g. to the sum of background and scattered field according to Eq. 5.2. It is shown in Fig. 5.3 and called the *total field* $\vec{E}_{tot}$. This field describes the real situation as it would be measured if one could measure the

field strength in such materials.
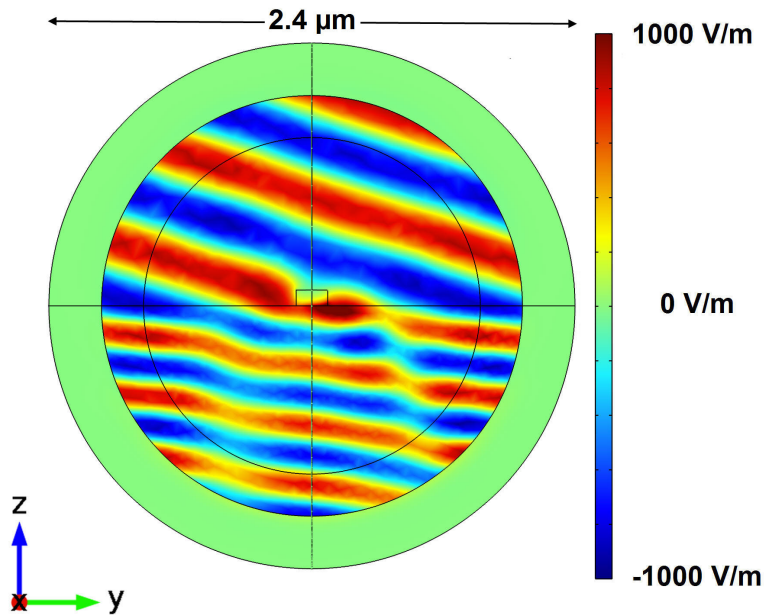
Figure 5.3: The total field is the the sum of the model input shown in Fig. 5.1 and the model output shown in Fig. 5.2. Together they describe the real situation as it would be measured if one could measure the field strength in such materials.

The material properties are defined by the wavelength-dependent complex optical constant, which is taken from [Pal85] for Cu, from [Gre08] for Si, and from [Sin] for SiN$_x$, having a refractive index of 2.01 at 1000 nm wavelength (corresponding to 2.05 at the usually denoted 533 nm wavelength).

The author tested the model on spherical particles [Vog12]. It turned out that the biggest difference between the numerical simulation and the Mie theory was below 4% for both absorption and scattering values. This indicates the accuracy of the results presented in the following. A more datailed description of the simulation model can be found in[Vog11]. However, the results presented in the following were achieved in collaboration with R. Farkas, whom the author supervised during R. Farkas diploma thesis [Far13] .

5.2 Results

5.2.1 Normal incidence

First the scattering and absorption characteristics of differently shaped and differently sized Cu-NP are compared. The aim is to find shapes and sizes where the particles cause most scattering but only little absorption. The interaction of the particle with incoming light is quantified with an area denoted as the extinction cross-section C_{ext}, which can be divided in two different kinds of interactions: scattering C_{sca} and absorption C_{abs}. These cross-sections can be bigger than the geometrical cross-section of the particle. To compare the

effectiveness among particles of different sizes, their C_{sca} and C_{abs} cross-sections are divided by the particle's geometrical cross-section, called (extinction, scattering or absorption) efficiency Q.
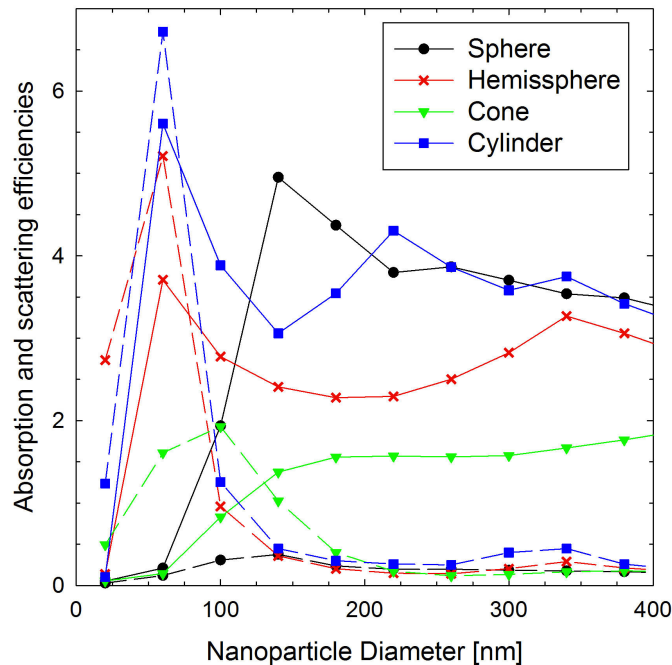
Figure 5.4: The absorpion efficiency Q_{abs} (dashed lines) and the scattering efficiency Q_{sca} (solid lines) of differently shaped NP, simulated with normal incidence of light in the domain shown in Fig. 5.1. Each shape has it's own scattering characteristics and optimum size.

In the following, simulation results of particles whose height equals their radius are considered. Figure 5.4 shows their scattering efficiency Q_{sca} (solid lines) and their absorption efficiency Q_{abs} (dashed lines) in dependence of their diameter for normal incidence. The spherical particles (black circles) have a scattering efficiency maxima at a diameter of (140 ± 20) nm. The hemispherical particles (red crosses) with their flat side on the Si interface have two local maxima in their scattering efficiency: at a diameter of (60 ± 20) nm and at (340 ± 20) nm. The cylindrical particles (blue squares) have local maxima at those sizes as well plus a third at (220 ± 20) nm.

One has to consider that not all of the light radiated by the NP is radiated into the Si. This fact is quantified by the coupling efficiency [Cat08]:

$$F_{sub} = \frac{P_{\mathrm{sca,Si}}}{P_{\mathrm{sca}}}. \tag{5.3}$$

It characterizes which power fraction of the scattered light is scattered into the Si. Figure 5.5 shows the coupling efficiency of the same particles as simulated in the previous Fig. 5.4. The highest coupling efficiencies are achieved at a diameter of (100 ± 20) nm for cone shaped particles and at a diameter of (60 ± 20) nm for the particles of the three other
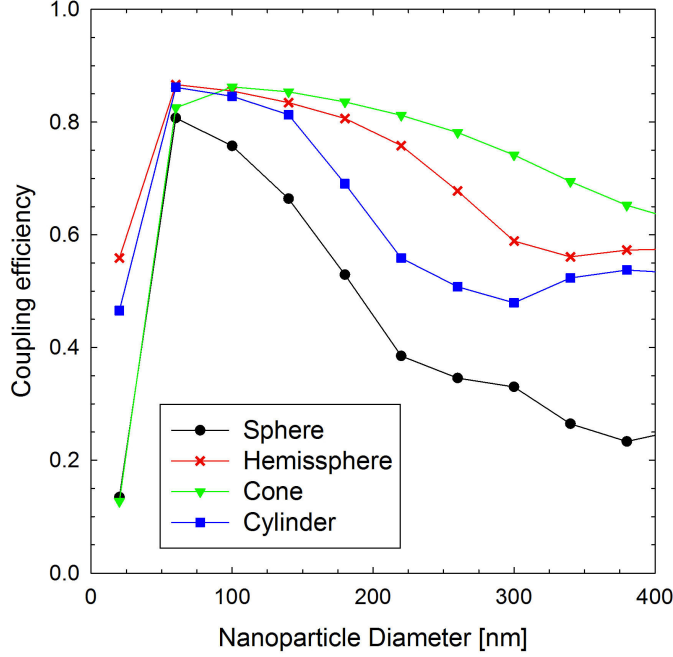
Figure 5.5: The simulated coupling efficiencies, defined by Eq. (5.3), of differently shaped NPs in dependence of their diameter. It is decreasing for particles with diameters larger than 50 nm.

shapes. The lower coupling efficiency for bigger particles is due to the fact that scattering is caused at the particle's surface, and that for bigger particles part of the surface is further away from the Si, therefore less light gets coupled into the Si.

However, the coupling efficiency does not take the amount of absorption into account. The goal is to evaluate the performance of different kinds of NPs for light trapping. Hence, maximizing the coupling efficiency F_{sub} maximizes the scattering into the Si, but one also wants to minimize the absorption and the scattering in other directions than Si at the same time. To do this, a useful measure is the reflectance of the particle

$$R_{NP} = \frac{P_{scat,Si}}{P_{\text{ext}}}. \tag{5.4}$$

Note, however, that this reflectance is not defined as usual in respect to the area of the Si surface, but in respect to the area of the NP particle's extinction cross-section. In order to get traditional reflectance values for the rear side of Si covered with NPs, one needs to consider which fraction of the Si is optically (not geometrically) covered by the NPs.

The reflectance of the particle defined in Eq. (5.4) was used in [Bec11] as the product of the coupling efficiency $F_{sub} = P_{scat,Si}/P_{scat}$ and the radiation efficiency $\eta_{scat} = P_{scat}/P_{\text{ext}}$.

Analogous definitions as in Eq. (5.4) for absorbance and transmittance are $A_{NP} = P_{\text{abs}}/P_{\text{ext}}$ and $T_{NP} = P_{scat,SiN}/P_{\text{ext}}$.
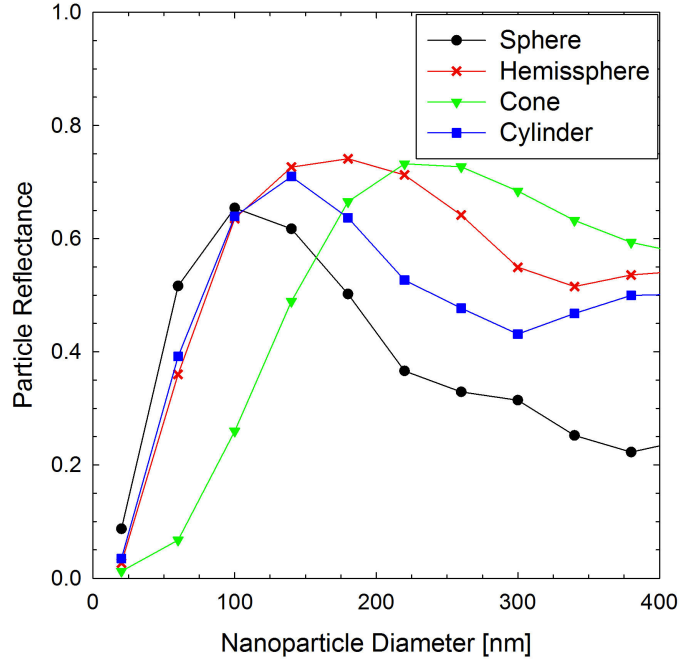
Figure 5.6: The simulated particle reflectance R_{NP}, defined in Eq. (5.4), of differently shaped NPs in dependence of their diamter, for normal incidence. Each shape has its own optimum size.

Figure 5.6 shows the NP reflectance in dependence of their diameter. For every shape there is a different optimum size: a diameter of (100 ± 20) nm for spheres, (140 ± 20) nm for cylinders, (180 ± 20) nm for hemispheres and (220 ± 20) nm for spheres. Every particle shape has only one maxima, which make this a good quantity when optimizing NPs for solar cell applications. The decrease for larger sizes is caused by the fact that they scatter more light away from the Si, whereas particles smaller than the optimum size suffer from higher absorption.

5.2.2 Oblique angle of incidence

In the following the angle of incidence for the incoming light is varied. The NP's size is kept constant at a diameter of $d = 240$ nm and height $h = 120$ nm for the cone shaped particles, and $d = 150$ nm with $h = 75$ nm for hemispherical and cylindrical shaped particles.

Figure 5.7 shows the particle reflectance R_{NP}, as defined in Eq. (5.4), versus angle of incidence. The angle of incidence is defined between the incoming light and the normal of the Si surface. All shapes start with a value between 0.7 and 0.75 for normal incidence, then drop slightly before increasing again for angles above $30°$. The drop is caused by an increase in absorption with a maxima around $20°$. At the Si-SiN$_x$ interface the critical angle for total reflection is near $35°$; the increase above $30°$ is due to an increase in coupling efficiency.
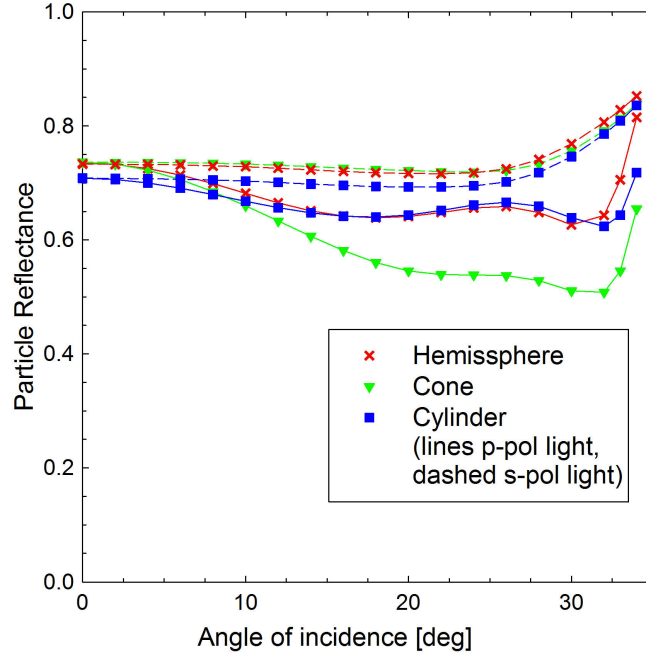
Figure 5.7: The simulated particle reflectance R_{NP}, defined in Eq. (5.4), of differently shaped NPs in dependence of the incident angle of the incoming light. The particle reflectance is higer for p-polarized (dashed lines) than for s-polarized light (solid lines), independently of shape.

For all shapes, the incoming light is simulated either with s-polarization (dashed lines) or p-polarization (solid lines). While they are, as expected, equal at 0° For the other angles, the incoming s-polarized light causes a higher particle reflectance than p-polarized light. There is a similarity between the particle reflectance and the conventional interface reflectance: in both cases s-polarized light reflects more than p-polarzied. For p-polarization the reflectance at the Si-SiN$_x$ interface has a Brewster angle $\alpha_{br} \approx 29.4°$ (at $\lambda = 1000$ nm). The particle reflectance, however, has a secondary minimum at $\alpha = (18 \pm 1)°$ and a primary one at $(31 \pm 2)°$ for the simulated sizes. Additionally the particle reflectance for s-polarized incoming light does not increase continuously with increasing angle of incidence – it has a local minimum near $(18 \pm 1)°$. The difference between s- and p-polarized light is due to the coupling efficency F_{sub} increasing for all simulated shapes from about 0.8 at 0° to about 0.89 at 34° for the s-polarized case, while it remains constant or even decreases under p-polarized light.

Plots of the angular distribution of the scattered light have been used before to explain the NP behavior [Mok11; Vog12]. However, in this work, the angle of incidence is varied. Figure 5.8 shows polar plots of the scatted light intsity in [W/m^2] of the same particles as in Figure 5.7 under s-polarized light for incident angles of .180°, 170°, 160° and 150°.

Normal incidence is shown in Figure 5.8(a), the electrical field is oscillating perpendicular the plotted plane. The majority of the light is scattered backward between 120° and 240°. With s-polarized light incoming from 170° the light is scattered in the area between 150°

(a) Angle of Incidence 180°.

(b) Angle of Incidence 170°.

(c) Angle of Incidence 160°.

(d) Angle of Incidence 150°.
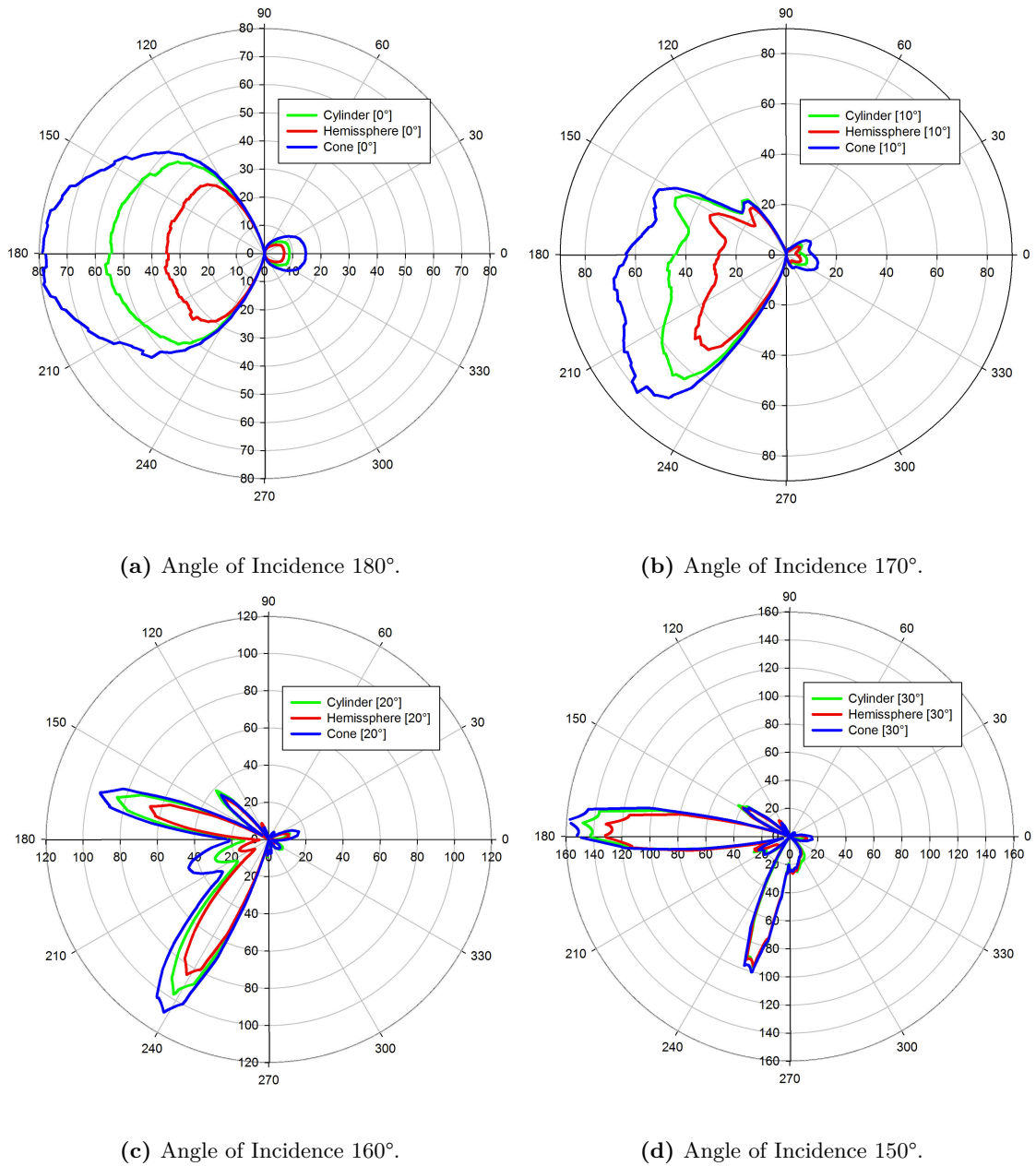
Figure 5.8: Left semicircles Si; right semicircles SiN. The simulated light intensities scattered by NPs with incoming **s-polarized** light from different directions. The scattering characteristics change from one major scattering direction at normal incidence to two major scattering directions at larger angles of the incoming light.

and 240° see Figure 5.8(b). For greater angles of incoming light two peaks with very strong scattering occur, those are around 164° and 238° in Fig. 5.8(c) similar to 176° and 254° in Fig. 5.8(d). The change in the scattering characteristics occurs continuously between 12°

and 18° as angle of incidence .
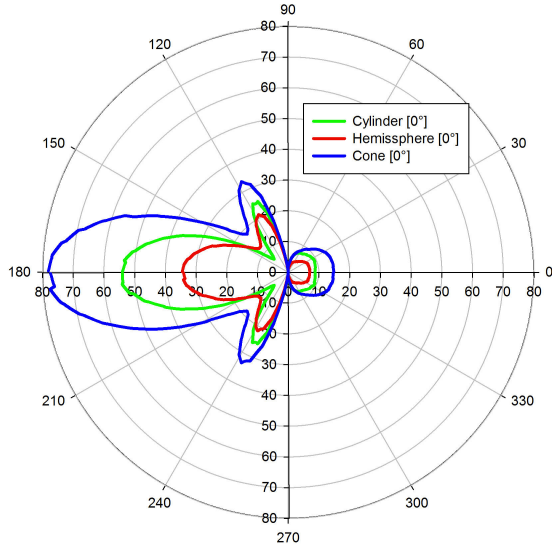
(a) Angle of Incidence 180°.
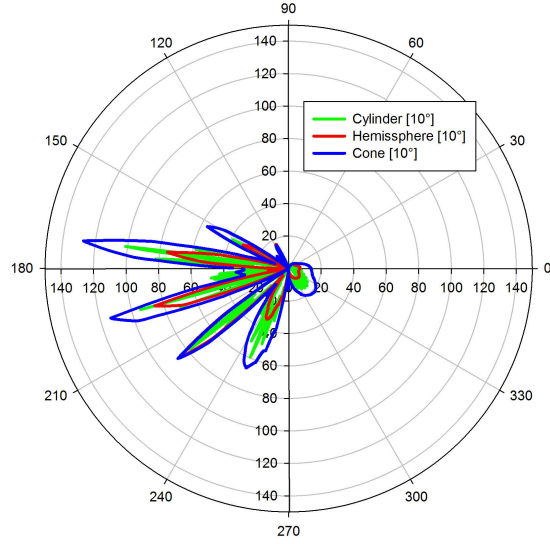
(b) Angle of Incidence 170°.
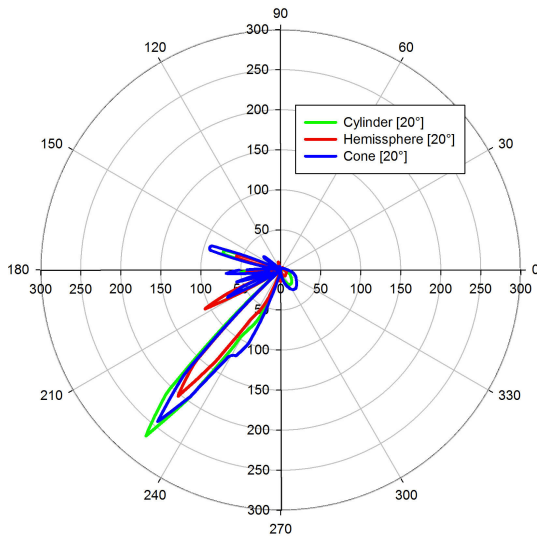
(c) Angle of Incidence 160°.
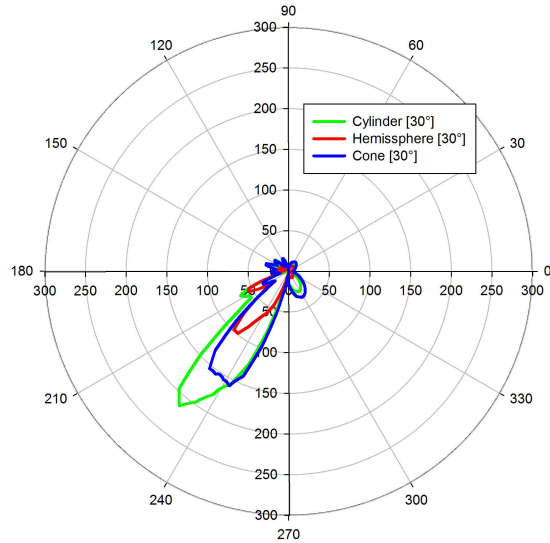
(d) Angle of Incidence 150°.

Figure 5.9: Left semicircles Si; right semicircles SiN. The intensities scattered by NPs as in Fig. 5.8(d) but with **p-polarized** incoming light. The scattering characteristics change from a dipol shape at normal incidence to one major scattering direction at more obligue incedence.

Note that the electrical field of the incoming light in Figure 5.9 is oscillating within the plotted plane. For normal incidence Fig. 5.9(a) shows typical dipole like scattering distributions with higher modes at 120° and 240°. For small angles such as shown in

Fig. 5.9(b) there are 4 to 5 sharp major directions in which the light is scattered. The change between dipole like scattering and the various directions shown in Fig. 5.9(b) occurs already at $(2 \pm 1)°$, whereas for bigger angles such as in Figures 5.9(c) and 5.9(d) the light is scattered in one major direction at around 231°. The major scattering direction shifts slightly for angles between 18° and 30°, but the preferred scattering directions are always similar for all three shapes. The change from 4 to 5 sharp major peaks towards one preferred scattering direction occurs between 14° and 18° with one of the 4 to 5 major peaks growing in intensity while the remaining ones stay at constant intensity.

The loss cone in which light is not totally reflected to the front surface is ≤16°. Figures 5.8(a) and 5.9(a) show that a large portion of light is scattered outside of the loss cone even for light with normal incidence or close to it. This is in good agreement with [Bas12], where it was observed that NP increase the light reflected outside of the loss cone from 30% to 80%.

5.2.3 Shells

Nanoshells are a mixture of nanoparticles and nanovoids, consisting of a dielectric surrounding, a metal shell, and a dielectric core. This offers twice as many surfaces for exciting surface plasmons, since they can occur at the outer as well as the inner metal-dielectric interface. It also introduces an additional degree of freedom (shell thickness). Although one can have two different dielectrics at the outside and inside, in the following results are shown for SiN_x at both sides.

(a) Shell Cu-thickness d=9nm.   (b) Shell Cu-thickness d=20nm.
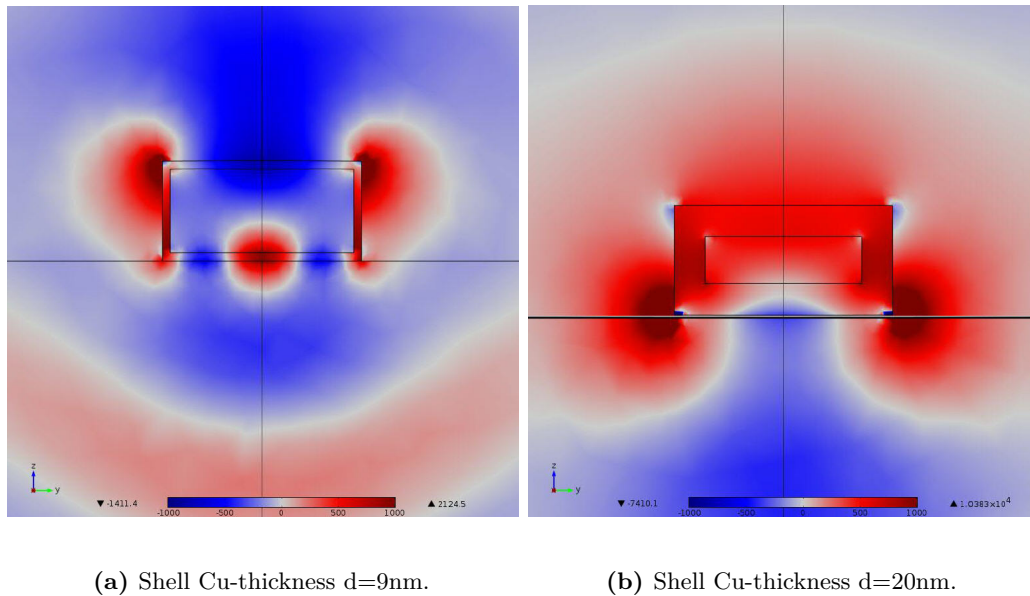
Figure 5.10: Simulation of the scattered (secondary) fields of two nanoshells with different shell thicknesses. The position of the strongest local field depends on shell thickness.

Figure 5.10 shows the scattered (secondary) field surrounding two nanoshells with different
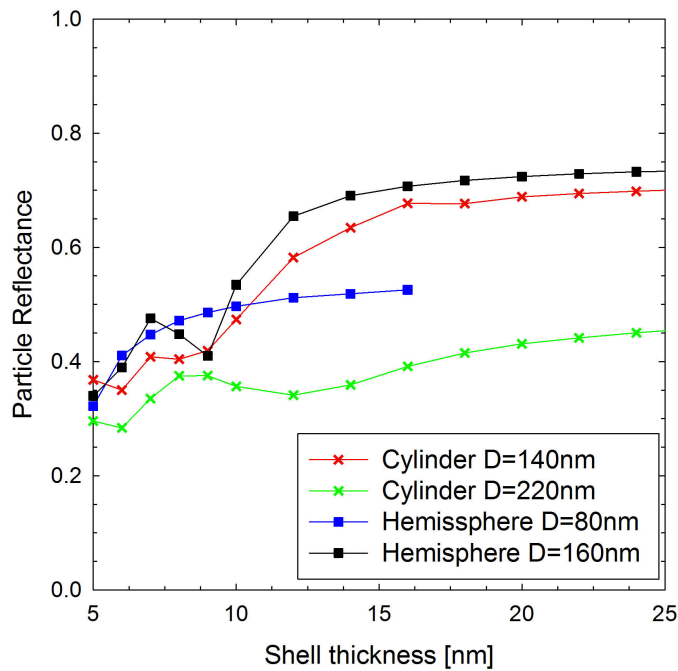
Figure 5.11: Simulated particle reflection for different nanoshells. Is increases with larger shell thickness.

Cu thicknesses. They have different modes. The thinner Cu shell has the strongest local field at the upper corners, while the thicker Cu shell has the strongest local fields at the bottom corners adjacent to Si, which results in better back scattering.

This is the underlying reason for the behavior of the particle reflection shown in Figure 5.11 for two different cylindrically shaped particles (squares) and two different hemispherical particles. For all tested scenarios the weighted scattering increases for higher shell thicknesses. For shell thicknesses above 20 nm the scattering characteristics are nearly identical to filled nanoparticles. Hence, for the scenarios simulated here it is better not to use nanoshells, but to use filled nanoparticles.

5.3 Conclusion

Simulation results for differently shaped and sized nanoparticle where presented. Hemispherical particles with a diameter of (140 ± 20) nm are best suited for scattering at a Si-SiN$_x$ interface at the simulated wavelengths of 1000 nm. Cylindrically and cone shaped particles have similar performance.

While nanoshells offer an additional parameter to optimize their scattering (their shell thickness), no scattering enhancement compared to filled nanoparticles could be found.

Differently shaped nanoparticles react similarly to variations in the angle of incidence. However, there is a difference between the incoming s- and p-polarized light. A change in scattering characteristics occurs in the range between 12° and 18°.

CHAPTER 6

Numerical Modeling of c-Si PV Modules by Coupling the Semiconductor with the Thermal Conduction, Convection and Radiation Equations

Increasing operating temperatures causes the open-circuit voltage V_{oc} of solar cells to decrease in an approximately linear manner, decreasing the efficiency of PV modules. A more general discussion on the thermal behavior of solar cells can be found in standard text books e.g. [Gre92, p.92] or [Wö05, p. 149]. Standard silicon wafer based PV modules have a typical efficiency change between 0.4% and 0.5% per Kelvin near the temperature of the standard testing conditions (STC) at 25°C, where the reference efficiency is measured. A review can be found in [Sko09]. Consequently, evaluating module performance in the field necessitates knowing its temperature behavior.

Next to air temperature and wind speed, an important driver of the module temperature is the sun's irradiation. In the previous Chapter 4 only the part of the solar spectrum was considered that can be absorbed by silicon 3.4, since other parts of the spectrum cannot contribute to the photo generation in the cell. However, light with longer wavelengths is absorbed by other materials than silicon. Together with the thermalization and recombination of photo generated carriers, this parasitic absorption increases the module operating temperature in the field.

Figure 6.1 shows the solar irradiance over wavelength at a location with 48.2° latitude, calculated by SMARTS [Gue01]. About 99% of it is in the wavelength range between 300–2500 nm. Therefore this is the wavelength range considered in the following.

In section 3.4 the measurements showed that silicon hardly absorbs any light with wavelengths above 1200 nm. Therefore it is feasible to reduce the amount of parasitic absorption in a solar module above that wavelength without decreasing the electrical power.

In this chapter ray tracing is used to calculate the heat source in each module component. Furthermore, a simulation model is established in which the semiconductor equations 6.1 are solved coupled with the thermal equations 6.2. This model solves the temperature and the resulting IV curve in a self-consistent manner. The temperature difference to the ambient depends most strongly on wind speed (considered for a given solar irradiation flux),
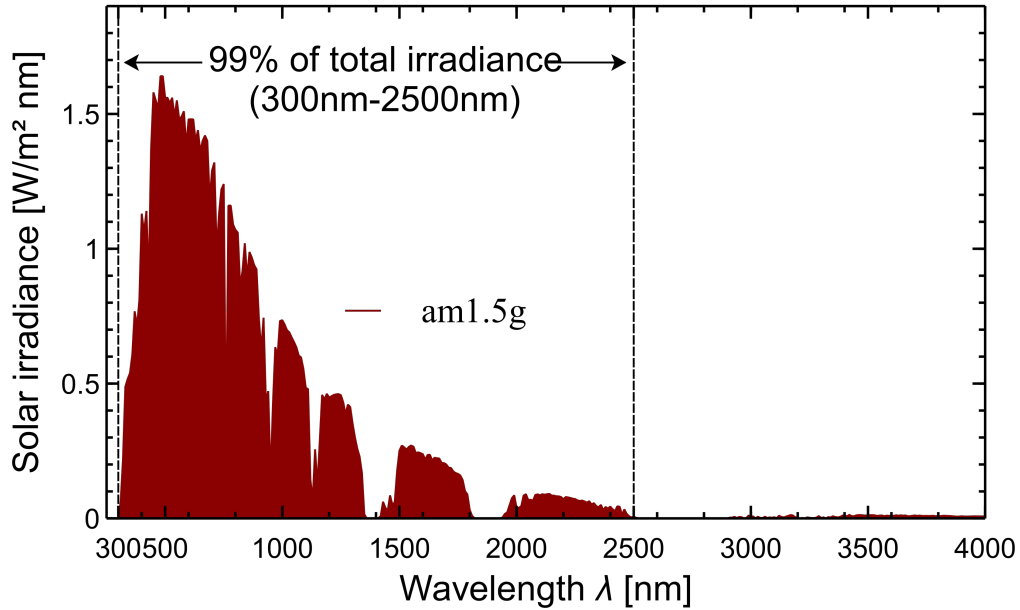
Figure 6.1: The irradiance (intensity) of the am1.5g spectrum. Note that 99% of the irradiance is in the wavelength range between 300 nm and 2500 nm.

and to a smaller extent on the thermal properties of the module, such as heat conduction and emissivity. For validation of the simulation model, experimental data from a solar module in an outdoor test will be used. Finally, suggestions are made for lowering the module's operating temperature based on improving the optical properties of the module. Some figures and results shown in this chapter were first published in [Vog15a].

6.1 Simulation model

Nowadays, excellent software is available for multiphysics simulations, such as the finite-element method (FEM) software Comsol. In a first step, the semiconductor model for c-Si solar cells as used in state-of-the-art simulations [Alt11] is implemented into the 'semiconductor module' of Comsol. Then this model is coupled with Comsol's equations for thermal conduction, thermal radiation, natural convection, and forced convection (by wind). This allows the simulation the IV curves of solar cells for given irradiance, ambient temperature and wind speed, while keeping the cell temperature floating. Fig. 6.2 shows the main information flow in the simulation model.

Heat sources include the parasitic absorption of sunlight throughout the module (in the cell metallization, EVA etc.), thermalization of photo-generated carriers in Si, their recombination, and entropy generation during charge carrier extraction. Parasitic absorption and photo-generation are calculated with sophisticated ray tracing from 300 nm to 2500 nm introduced in the previous chapter. This approach has the advantage that the effects of
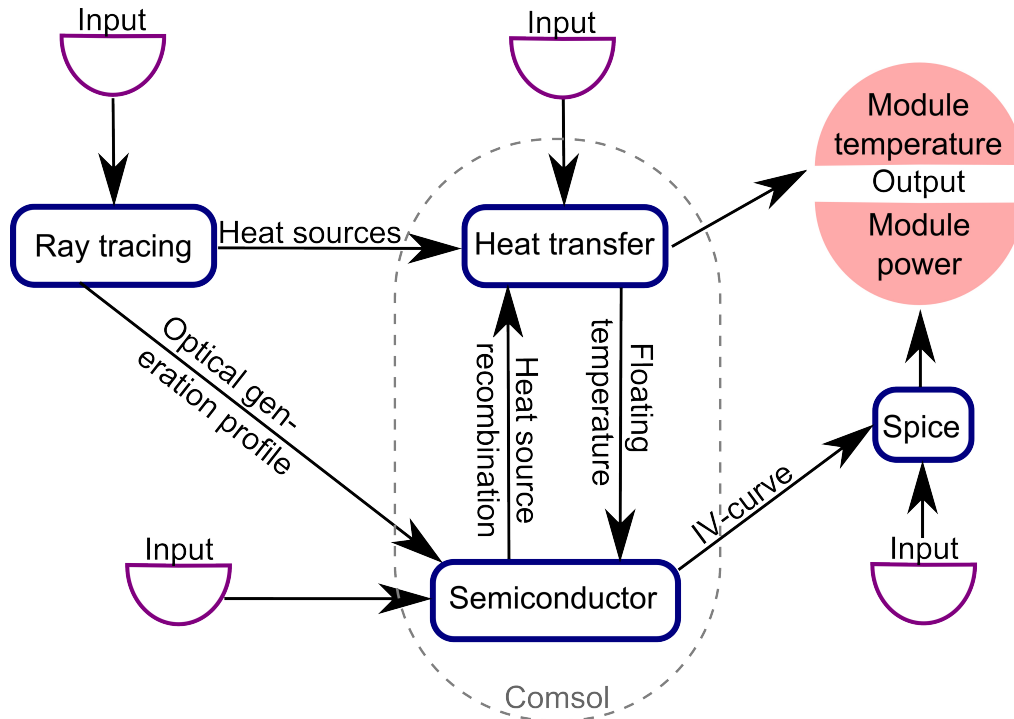
Figure 6.2: Schematic of the simulation model showing the information flow between the different parts of the model.

parasitic absorption on the module temperature are investigated more accurately than previous works on thermal PV module behavior such as:

- S. Krauter's analytical model of the thermal and optical properties [Kra93] and validated it later with experiments [Kra96]. However, his model did not solve the semiconductor equations and also considered only a few different wavelengths.

- A numerical code (TASC-1D-cSi) simulating the optical, electrical and thermal behavior introduced by [Dup14]. However, this model did not include various module components such as glass, encapsulant or parasitic absorption in the rear reflector, which lead to predictions on the optimal thicknesses of solar cells and their ARCs that could not be confirmed. The reason behind this was that a module's front side radiation is governed by the glass [Kra93, p. 89].

- The coupled optical and thermal model introduced by [Hoa14]. This model predicted the power output for PV modules in several cities in Europe. In contrast to this work, the optical properties in [Hoa14] were modeled in 1 dimension and averaged over all wavelengths.

As shown in the schematic of Fig. 6.2, the circuit simulation tool LTSPICE IV is used to calculate the module power resulting from the IV curves of 60 cells.

6.1.1 Semiconductor and cell properties

The semiconductor equations, consisting of the Poisson (6.1a), continuity (6.1b), (6.1c) and transport equations with the drift-diffusion approximation (6.1d), (6.1e) are solved with the temperature kept floating and coupled to the module's thermal simulation:

$$\nabla\left(\varepsilon\nabla\phi\right) = -q\left(p - n + N_{don}^{+} - N_{acc}^{-}\right) \tag{6.1a}$$

$$\frac{\partial n}{\partial t} = \frac{1}{q}\vec{J}_n + G - R \tag{6.1b}$$

$$\frac{\partial p}{\partial t} = -\frac{1}{q}\vec{J}_p + G - R \tag{6.1c}$$

$$\vec{J}_n = -q\mu_n n\nabla\phi + qD_n\nabla n \tag{6.1d}$$

$$\vec{J}_p = -q\mu_p p\nabla\phi - qD_p\nabla p, \ . \tag{6.1e}$$

Here, ε is the dielectric function, ϕ the electrostatic potential, q the electric unit charge, n the electron density, p the hole density, N_{don}^{-} the donor density, N_{acc}^{+} the acceptor density, t the time, $\vec{J}_n$ the electron current density, $\vec{J}_p$ the hole current density, G the generation rate, R the recombination rate, μ_n the electron mobility, μ_p the hole mobility, D_n the electron diffusion constant and D_p the hole diffusion constant.

A well established semiconductor model for c-Si solar cells [Alt11] is implemented into the recently developed 'semiconductor module' of COMSOL. A temperature dependent implementation of the free-carrier mobility [Kla92], band gap narrowing [Sch98], Auger recombination [Alt97], and radiative recombination [Ngu14] is chosen.

An industrial standard c-Si solar cell with an efficiency of η=18.5% at an operating temperature of 25 °C is taken as an example. More specifically a 180 µm thick p-type wafer with a acceptor density N_{acc}^{+} of 1×10^{15} cm^{-3} has a front side emitter with a donor density N_{don}^{-} of 3×10^{20} cm^{-3} at the top and 1×10^{19} cm^{-3} at the tail. The aluminum back surfaces field (BSF) has an acceptor density N_{acc}^{+} of 1×10^{19} cm^{-3} and a thickness of 6 µm. The cell's temperature coefficient turns out in the simulations to be 0.5%$_{rel}$/ °C, which is in good agreement with literature [Sko09]. Please note that this temperature coefficient is not an input parameter, but a consequence of the temperature dependent implementation of the semiconductor properties as listed above.

6.1.2 Heat transfer and module properties

While the ray tracing is done in full-size 3D, the semiconductor/thermal part can be reduced to one dimension with only little error, which enables very fast computation times.

The time to reach a fully-coupled solution in this 1D model is about 3 minutes on a typical desktop computer (4 CPUs, 3 GHz, 8 GB RAM).

In this model, it is assumed that the PV module consists of the following layers, each having different material properties (see table 6.1): A 3.2 mm thick float glass as top cover, 450 µm of encapsulant above and below the cells, and at the rear there is a white backsheet with 350 µm thickness. The cells are made of 180 µm thick Si wafers with a 100 µm thick Al full-area back contact, as can be seen in fig. 6.3.

Each layer has its own heat source Q, which is calculated via ray tracing. In the cell, there is an additional heat source due to thermalization, recombination and entropy generation during current extraction. The simulation for calculating the heat sources are described in section 6.1.3 and the results follow in 6.2.
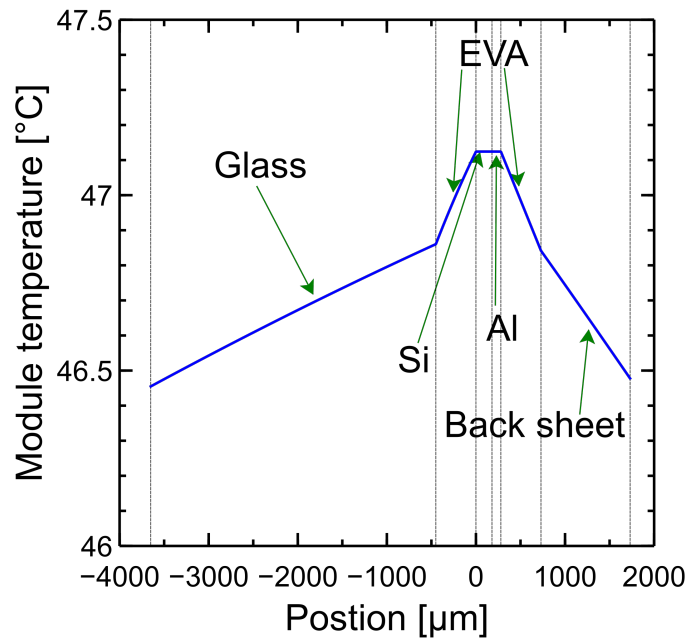
Figure 6.3: A typical temperature distribution simulated with the model having no wind, an ambient temperature of the air of 25°C and 1000 W/m² irradiation. The temperature gradient within the module is less than 0.8°C, which indicates that the cooling is limited by the heat transfer towards the surroundings.

The temperature within the module is governed by three equations. The thermal conduction 6.2a, radiation 6.2b and convection 6.2c equation, implemented as follows:

$$\rho \cdot C_{\mathrm{p}} \cdot \frac{\partial T}{\partial t} = \nabla \cdot (k \cdot \nabla T) + Q \tag{6.2a}$$

$$P = \varepsilon_{\mathrm{sur}} \cdot \sigma \left(T_{\mathrm{amb}}^4 - T^4 \right) \tag{6.2b}$$

$$h \cdot (T_{\mathrm{amb}} - T) = -\vec{n} \cdot (-k \cdot \nabla T) \,. \tag{6.2c}$$

Here, ρ is the material density, C_{p} the heat capacity, T the temperature, k the thermal conductivity, Q the heat source, P the power, $\varepsilon_{\mathrm{sur}}$ the surface emissivity, σ the Stefan Boltzmann constant, $\vec{n}$ the normal to the module's surface and h the heat transfer coefficient. These equations are solved in a fully coupled manner with the semiconductor model, from where heat due to thermalization, recombination, and charge carrier extraction is taken.

Table 6.1 lists the materials' thermal properties of the different layers used in this chapter. Please note that [Arm10; Hoa14; Not05] did not measure the parameters themselves, but gathered them from sources which were not accessible to the author of this work. In terms of thermal conductivity within the PV module the encapsulation material has the lowest value. Therefore, it is the material with the highest temperature gradient in Fig. 6.3, which means it is limiting the temperature equalization within the module. However, the sharpest temperature drop is at the edges of the module, which are assumed to be in contact with air at 25°C. This indicates that the modules cooling is limited by the contact to its surroundings. This is governed by the thermal radiation the module exchanges with the surroundings and the thermal convection due to contact with air.

Table 6.1: Thermal material parameters used for the simulations in this chapter. The surface emisivity is only used for the outermost layers because they are the only materials that emit thermal radiation to the surroundings.

Material	Thermal conductivity k [W m^{-1} K^{-1}]	Density ρ [kg m^{-3}]	Heat capacity C_{p} [J kg^{-1} K^{-1}]	Surface emissivity $\varepsilon_{\mathrm{sur}}$
Glass [Not05]	1.8	2700	750	0.9
EVA [Arm10]	0.32 [Wol05]	960	2090	-
Silicon [Not05]	149	2300	838	-
Aluminum [Arm10]	237	2700	900	-
Backsheet [Hoa14]	0.56 [Wol05]	1370	1760	0.9

For the thermal radiation equation 6.2b, it is assumed that the ground below the module has ambient temperature, and the sky's temperature is calculated by means of the approximation,

$$T_{\mathrm{sky}} = T_{\mathrm{amb}} - 6 \text{ K}, \tag{6.3}$$

which, according to [Kra93, p. 92], originated from [Whi67]. Krauter [Kra93, p. 92]

discusses two further approximations for calculating the sky's temperature. Implementing one of those other two approximations led to this model underestimating the module's temperature in comparison with the field data. This underestimation has the biggest impact when choosing a scenario with low irradiation (100 W/m^2) and no wind. In this case field data suggest a module back side temperature elevated about 1.5°C above ambient temperature (see section 6.3, figure 6.7), which could best be described by equation 6.3.

The thermal convection equation describing the interaction with the air above and below the module is very dependent on the assumed heat transfer coefficient h between module and air. For the module's front side, forced convection 6.4 is assumed to calculate the heat transfer coefficient h, dependent on wind speed. For both, the module's front and back side, natural convection 6.5 of a tilted plate is assumed to calculate the thermal convection between the air and the module's surface, independent of wind speed.

The heat transfer coefficient h in the case of forced convection (dependent on wind) is chosen as [Arm10]:

$$h_{\text{forced}} = 2 \frac{k \cdot 0.3387 \cdot \sqrt[3]{\dfrac{\mu_{\text{vis}} \cdot C_{\text{p}}}{k}}}{L \left(1 + \left(\dfrac{0.0468 \cdot k}{\mu_{\text{vis}} \cdot C_{\text{p}}}\right)^{2/3}\right)} \cdot \sqrt{\frac{\rho \cdot v_{\text{wind}} \cdot L}{\mu_{\text{vis}}}}, \tag{6.4}$$

and in the case of natural convection (independent of wind):

$$h_{\text{forced}} = \frac{k}{L} \cdot \left(0.68 + \frac{0.67 \sqrt[4]{\cos\left(\varphi\right) \cdot R_{al}}}{\left(1 + \left(\dfrac{0.492 \cdot k}{\mu_{\text{vis}} \cdot C_{\text{p}}}\right)^{9/16}\right)^{4/9}}\right), \tag{6.5}$$

where v_{wind} is the wind speed, L the module length, μ_{vis} the air's viscosity, R_{al} the Raleigh number and φ the module tilt angle measured versus a vertical wall. More details on the heat transfer coefficient h between air and a solid plate can be found in [Bej93; The02]. As with the sky's temperature, these formulas are chosen from a range of alternatives [Arm10]. The choice above yielded the best agreement (see section 6.3, figure 6.7) with the experimental data gathered from an outdoor test.

6.1.3 Calculation of heat sources using ray tracing

In contrast to the coupled semiconductor and thermal model the ray tracing is done in three dimensions using the ray tracing framework DAIDALOS [Hol13] as discussed in chapter 4.

However, the spectral range of the light source is extended to 2200 nm, covering the wavelengths between 300 nm and 2500 nm in steps of 10 nm. 10 000 rays are simulated for every step. The incidence is orthogonal to the module's surface. The time for one ray tracing simulation as described is about 20 minutes on a typical desktop computer (4 CPUs, 3 GHz, 8 GB RAM), about 75% of the simulation time is spend on rays above 1200 nm since they typically travel much further within the module.

The results of the ray simulation directly lead to the absorptance of each component $A_{\mathrm{comp}}(\lambda_i)$. These are then used to calculate the heat source of each component $P_{\mathrm{comp}}^{\mathrm{HS}}$,

$$P_{\mathrm{comp}}^{\mathrm{HS}} = \int\limits_{300\ \mathrm{nm}}^{2500\ \mathrm{nm}} A_{\mathrm{comp}}(\lambda)\, I_{\mathrm{am1.5g}}(\lambda)\, d\lambda \tag{6.6a}$$

$$\approx \sum_{\lambda_i} A_{\mathrm{comp}}(\lambda_i)\, I_{\mathrm{am1.5g}}(\lambda_i) \tag{6.6b}$$

with $I_{\mathrm{am1.5g}}(\lambda_i)$ being the solar irradiance in $[\mathrm{W/m^2\ 10\ nm}]$ as shown in 6.4 and λ_i the wavelength in 10 nm steps over the interval from 300 nm to 2500 nm. For silicon a different formula has to be used since part of the power is converted into electrical power and not to heat:

$$P_{\mathrm{Si}}^{\mathrm{HS}} = \int\limits_{300\ \mathrm{nm}}^{2500\ \mathrm{nm}} A_{\mathrm{Si}}(\lambda)\, I_{\mathrm{am1.5g}}(\lambda)\, \frac{E_{ph}(\lambda) - E_{\mathrm{gap}}}{E_{ph}(\lambda)}\, d\lambda \tag{6.7a}$$

$$\approx \sum_{\lambda_i} A_{\mathrm{Si}}(\lambda_i)\, I_{\mathrm{am1.5g}}(\lambda_i)\, \frac{E_{\mathrm{ph}}(\lambda_i) - E_{\mathrm{gap}}}{E_{\mathrm{ph}}(\lambda_i)} \tag{6.7b}$$

where $E_{\mathrm{ph}}(\lambda_i)$ is the photon energy in [eV] and E_{gap} the energy of the silicon band gap (at room temperature $E_{\mathrm{gap}} = 1.12$ eV). This formula is only valid for $E_{\mathrm{ph}}(\lambda_i) \geq E_{\mathrm{gap}}$.

6.1.4 Calculation of module power with SPICE

Because the solar cells are connected in series in a standard 60 cell module, the module power is simulated with the circuit simulator LTSPICE IV from Linear Technology, considering all interconnector resistances. All cells gain part of their J_{sc} from light that is reflected by the backsheet before it is absorbed in the silicon. However, solar cells located next to the frame have 10 mm of backsheet next to them on at least one side, thus they have a higher J_{sc} than cells i the middle of the module with just 3 mm backsheet on every side. Hence the solar cells' J_{sc} values are adjusted according to their position in the module: the ray tracing analysis (details see chapter 4) shows that the cells on the edge of the module add a factor of 1.0126 to each J_{sc} and the corner cells a factor of 1.026. Due to the series interconnection of the solar cells, however, only part of these current-gains are exploited by the module.

In contrast to the ray tracing in the previous paragraph, the results of the semiconductor/thermal model include IV-curves. Thus one can extract the input parameters (J_{sc} adjusted for cell position, J_{01}, J_{02}, R_{shunt}, R_{series}) for the LTSPICE simulation from the IV-curves. The resistances are set to $R_{shunt} = 10\,000\ \Omega\mathrm{cm}^2$ and $R_{series} = 0.7\ \Omega\mathrm{cm}^2$ for all simulated modules, whereas J_{01}, J_{02} are determined via fitting of each combination of module type and module temperature.

6.2 Heat sources

The standard am1.5g spectrum [Gue01] normalized to 1000 W/m^2 between 250 nm and 4000 nm has 99% of it's irradiance between 300 nm and 2500 nm. Therefore one can restrict the simulations to the wavelength range between 300 nm and 2500 nm with little error. As shown in Fig. 6.4, about 20% of the irradiance is in the infrared (IR), where even a cell operating at the Lambertian limit cannot absorb it.
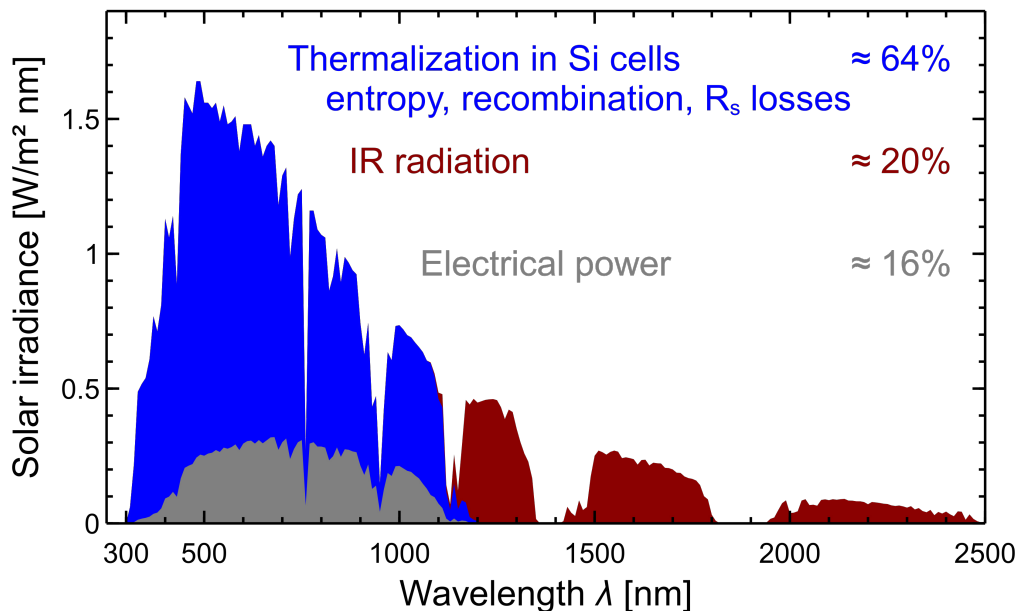
Figure 6.4: Am1.5g spectrum compared to a cells electrical power output when operating at 16% cell efficiency.

In addition to the IR losses, there are also thermalization, recombination, resistance and entropy losses to consider. The last two are only included in this model when calculating the cells IV curves and the modules power, but their impact as heat sources is not included. In table 6.2, a comparison of parasitic absorption and thermalization losses of each module type for different wavelength ranges is shown. Here three module types are considered:

1. EVA$_{UV-A}$ encapsulant and cells with a full-area rear side aluminum metallization (EVA + Al).

2. Silicone$_{\mathrm{UV-T}}$ encapsulant and cells with a full-area rear side aluminum metallization (Sil + Al).

3. EVA$_{\mathrm{UV-A}}$ encapsulant and cells with a full area SiN$_x$ dielectric rear side mirror (EVA + SiN$_x$), imitating PERC cells.

Because the cell's antireflection coating and the front side metallization are not explicitly included in the one dimensional COMSOL model, their parasitic absorption is added to the cell's heat source (HS). Hence, the IR absorbance of the front metallization causes the cells to have a heat source in the IR. Considering the standard module, about 18.9% of the sun's intensity is parasitically absorbed. The aluminum absorbs about 10%, mostly in the IR. Replacing the full-area rear side metallization with an SiN$_x$ dielectric mirror lowers the parasitic absorbance to 11.7%. The SiN$_x$ has a refractive index of n=2.09 at 633 nm and a thickness of 100 nm. It replaces the full aluminum contact of the standard cells.

Table 6.2: Comparison of heat sources (HS) of each module component via parasitic absorption and thermalization of each module type considered here, for the spectrum between 300-2500 nm and the wavelength range between 1200-2500 nm, where silicon is nearly transparent. Encapsulant (Encap.) is either EVA or silicone and the mirror at the rear side of the cell is either aluminum (Al) or silicon-nitride (SiN$_x$).

Module	Wavelength	Cell	Glass	Encap.	Mirror	Backsheet	Reflected
	[nm]	[W/m^2]	[W/m^2]	[W/m^2]	[W/m^2]	[W/m^2]	[W/m^2]
EVA + Al	300-2500	265.4	38.3	43.2	101.8	6.1	148.1
EVA + Al	1200-2500	2.1	14.2	3.2	73.3	3.2	58.3
Sil + Al	300-2500	280.3	35.6	5	104.6	8.1	164.5
Sil + Al	1200-2500	1.9	12	2	75	2.7	60.5
EVA + SiN$_x$	300-2500	266.2	47.5	47.3	0	20.6	217.1
EVA + SiN$_x$	1200-2500	2.5	17.3	5.8	0	16.8	111.8

Switching from an EVA$_{\mathrm{UV-A}}$ to a silicone$_{\mathrm{UV-T}}$ encapsulated module also lowers the parasitic absorbance to 15.3%, however most of that improvement is not in the IR and therefore it was already noticed, when no thermal properties were considered [Mci09; Mcl10; Vog14]. This improvement is also visible by the increase in the cell's heat source by 5.6% for the silicone encapsulated module, due to higher thermalization losses.

6.3 Field measurements

The module performance, the irradiance on the module, module as well as ambient temperatures, and wind speed were collected in an outdoor testing facility near Cologne in Germany by TÜV-Rheinland from 1. August 2011 until 31. August 2012. Measurements were made every 30 seconds in daylight.

In Figure 6.5, the measured data is filtered for an interval of ±1.5 °C around the investigated ambient temperature and an interval of ±15 W/m^2 around each radiation level to have

a sufficient number of data points. The figure illustrates the correlation between module (backside) temperature, wind speed and the impinging irradiance. As expected, the module temperature increases with more incoming radiation and decreases with increasing wind speed in a non linear manner.
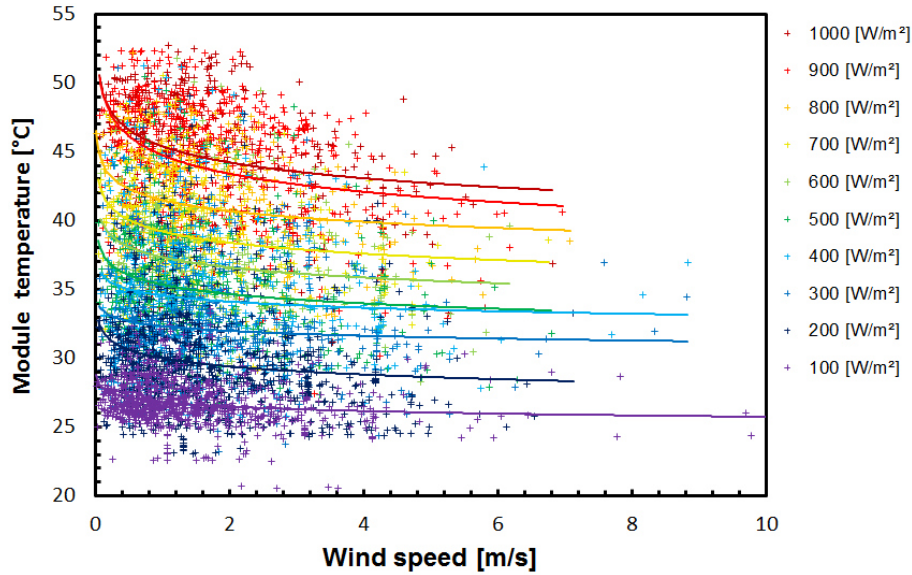
(a) Ambient temperature of 25 °C (±1.5 °C)
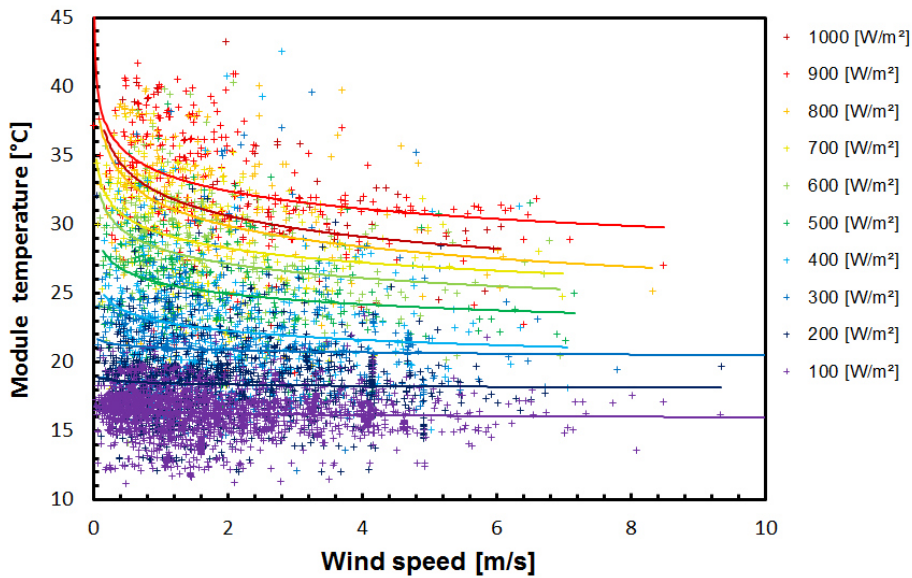
(b) Ambient temperature of 15 °C (±1.5 °C)

Figure 6.5: Symbols: Measured module (backside) temperature and wind speed at the indicated impinging irradiance (in an interval of ± 15 W/m^2), at two typical ambient temperatures. The lines are least-square fits with polynomials of the 2nd degree.

Note in the data at an ambient temperature of 25°C shown in Fig. 6.5(a) that hardly any data points are close to standard testing conditions (ambient temperature 25°C and 1000 W/m^2). Whereas Fig. 6.5(b) shows the data for an ambient temperature of 15°C. Here even more data points are at lower irradiation levels.

Fig. 6.6 shows the distribution of wind speed at daylight during the monitored period of one year. Different colors indicate different levels of incoming irradiation in W/m^2. All daylight includes occurrences that are not within in ±15 W/m^2 of the colored multiples of 100 W/m^2. The most frequent occurrences are for the weakes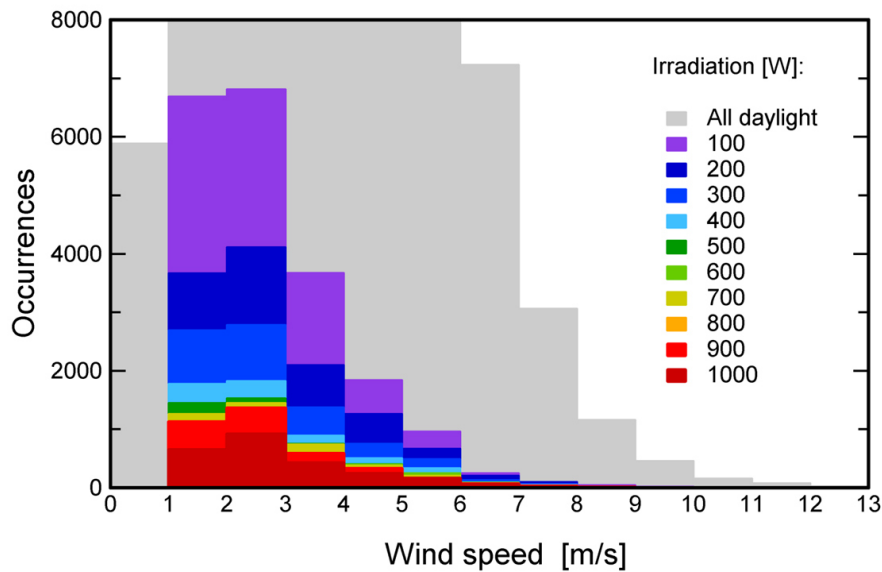t irradiation levels. Thus optimizing modules at low light intensity should be a major focus in the development of photovoltaic modules.

Figure 6.6: Histogram of wind speed at daylight over one year at the site near Cologne, Germany. Different colors indicate different levels of incoming irradiation in W/m^2. The most frequent occurrences are for the weakest irradiation levels.

However, our analysis shows that this distribution over wind speed varies only weakly with irradiance. At the site near Cologne, the wind speed is mainly below 4 m/s and hardly ever exceeds 8 m/s. Note that in Fig. 6.5, the largest temperature variation occurs in the slow wind range from 0 m/s to 3 m/s, which prevails in 65% of the daytime at the site near Cologne. At higher wind speeds than 3 m/s, only modest additional temperature reductions occur. Thus, one should optimize solar modules for slow wind conditions.

6.3.1 Model validation via field measurements

In the following, this model is validated by comparison with field measurements. For the heat sources in our simulation, the standard module in the top row from table 6.2 is selected and the heat sources are scaled linearly with the intensity of the incoming radiation.
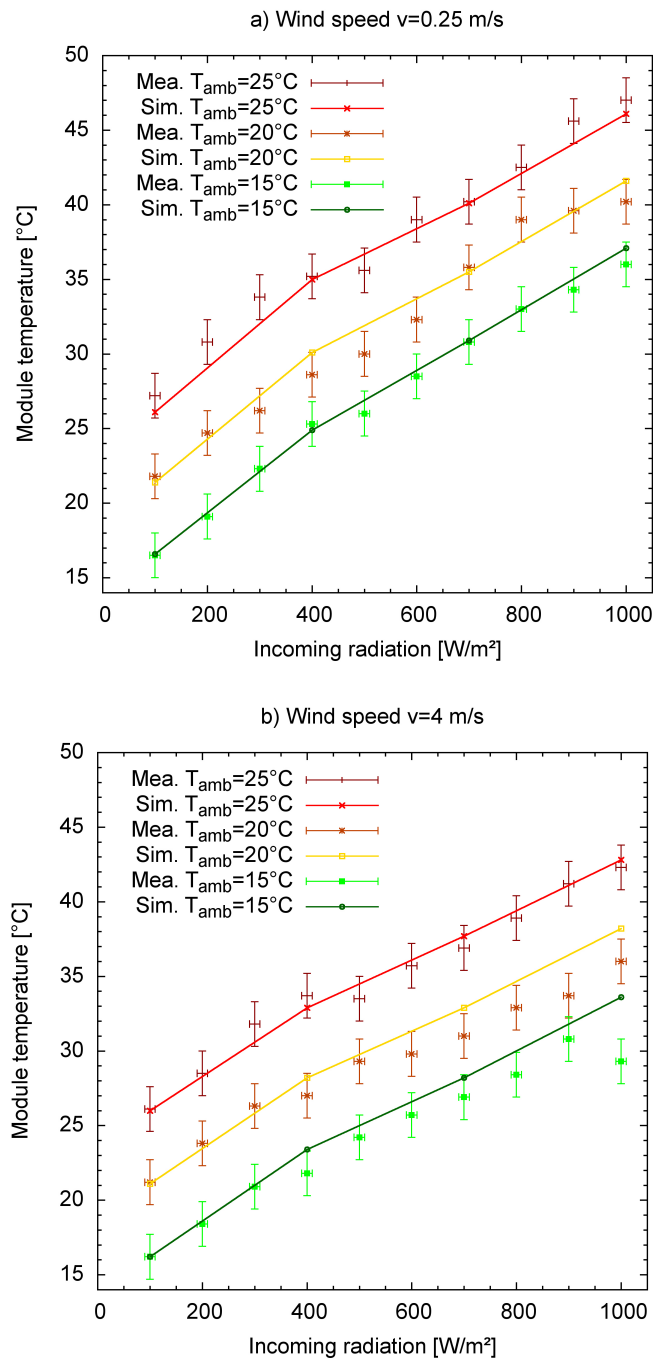
Figure 6.7: Comparison of simulated (lines) with measured (symbols) module temperature for different ambient temperatures and radiation levels. The error bars indicate the standard deviation of the measurement points from Fig. 6.5

Both graphs show the module backside temperature versus the incoming radiation for

three different ambient temperatures: 15°C, 20°C and 25°C. The simulations and the measurements show a nearly linear increase of module temperature with radiation for each given ambient temperature and wind speed. The average measured temperature increase by about (2 ± 0.8)°C per 100 W/m^2 irradiance, the simulated temperature by (2.2 ± 0.5)°C, which is within the standard deviation of the measurements (shown as error bars). Looking at the data more closely, one can see that the bigger $\Delta T = T_{\mathrm{mod}} - T_{\mathrm{amb}}$ the lower the temperature increase for the next 100 W/m^2 of additional radiation.

Considering the results for 0.25 m/s wind speed, there is very good agreement between the simulations and the field measurement data. For the 4 m/s scenario and for ambient temperatures of 15°C and 20°C, the simulations project a slightly higher module temperature than the field measurements. However, in the case with 25°C ambient temperature the agreement is quite good. It has been reported by Armstrong [Arm10] that the Nussuelt Relation which is used here to calculate the heat transfer coefficient h for forced convection 6.5, is to low. However, Armstrong also discussed ten other formulas for calculating the impact of wind speed on the solar module. After comparing all of them, the one (Eq. 6.4) is chosen that leads to the closest agreement between our simulations and the field measurement.

6.4 Results and discussion

Figure 6.8 shows the results of simulations with four different modules. All four are simulated in the following scenario: at 25 °C ambient temperature, with an impinging irradiance of 1000 W/m^2 with the am1.5g spectrum [Gue01], and 0 m/s wind speed. The same optical generation profile within the cells is chosen for all module types in order to clarify the impact of different thermal behaviors. This means that if each module operates at the ambient temperature of 25 °C, the cells' efficiencies would be 18.5% and each module would have an electrical power output of 262 W (blue bar). As described in section 6.1 the cells' efficiencies and modules' temperatures in Fig. 6.8(a) are the output of the thermal/semiconductor model and the module power in Fig. 6.8(b) results from an additional simulation step in LTSPICE taking all the interconnector resistances into account.

The module furthest to the right represents a standard module with EVA encapsulant and full-area Al back contact (black bar). At the assumed conditions, the simulation predicts that this module's back side temperature is 46.5°C and that it generates 12% less electrical power than it would if it operated at the ambient temperature (blue bar).

The module with silicone encapsulant (red bar) instead of EVA operates at a 0.9°C lower temperature, due to the lower parasitic absorption in the silicone.

Replacing the full-area back side metallization with an full area dielectric mirror (green bar) leads to more than 3.2 °C cooler operating temperature since it lowers the parasitic absorption from 18.9% to 11.7%.
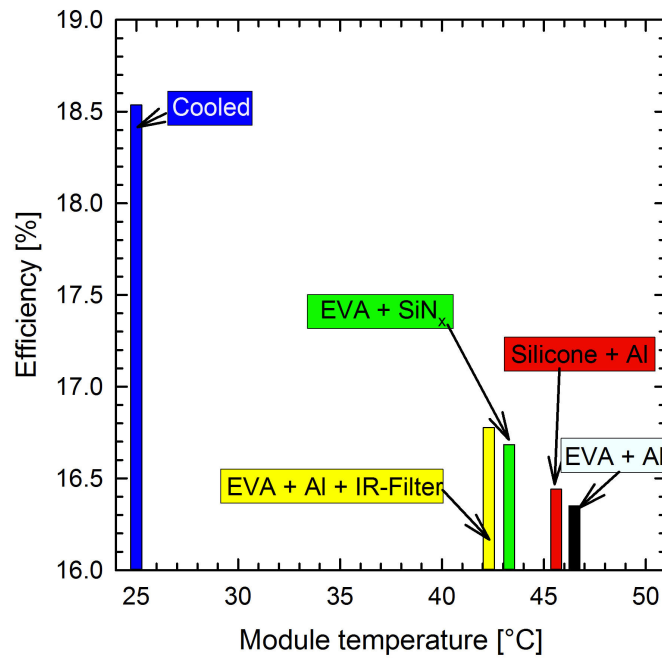
(a) Shows the cells' efficiencies.
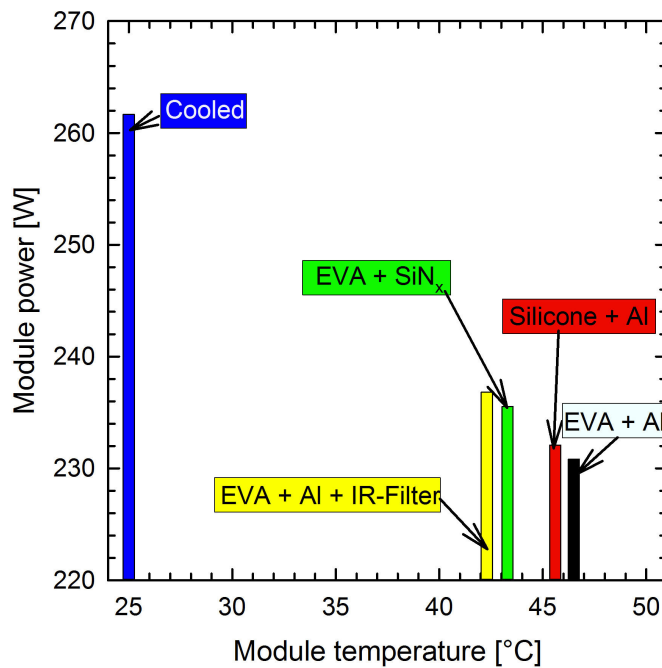
(b) Shows the module's electrical power output.

Figure 6.8: The effect of different module materials on the module's operating temperatures. This difference results in different cell efficiencies and module power output.

Covering the entire module with a 100% reflector (yellow bar) for light between 1205 nm and 2500 nm wavelength leads to an operating temperature 4.2°C lower than the standard module (with EVA encapsulant and full-area Al back contact (black bar)), provided that the reflector doesn't change the module's thermal behavior in any other way, but blocking those wavelengths from the spectrum.

Comparing those two improvements, one can see that most of the improvement can be achieved by eliminating parasitic absorption above 1205 nm wavelength. The next biggest absorbers in the relevant IR range between 1205 nm and 2500 nm are the glass and the backsheet. By reducing their absorbance to zero one could lower the solar module operating temperature by only another 1°C.

6.5 Conclusion

The simulation model reproduces the measurement data from an outdoor module test field very well. Looking at the field measurements, it becomes obvious that the vast majority of the time the wind speed is below 4 m/s, when there is at least 100 W/m^2 of incoming radiation. This reduces the cooling via forced convection (wind). Therefore it is even more important to prevent increased module operating temperatures due to parasitic absorption. The ray tracing analysis of different solar modules under the am1.5g spectrum between 300 nm and 2500 nm shows that about 18.9% of the irradiance becomes parasitically absorbed by a standard PV module with cells having a full-area rear metallization. Replacing it with PERC cells having a SiN$_x$ mirror lowers the parasitic absorbance to 11.7%, which leads to a 3.2 °C lower module operating temperature. This causes a 5 W higher electrical power output (when considering a module with 262 W). With a conventional simulation approach as in chapter 4, which does not take the IR radiation into account, those considerable advantages would not be noted. Therefore, it is advantageous to take also the module's thermal properties with wavelength resolution into account when optimizing solar cells and modules.

CHAPTER 7

Conclusion

In the experimental part I developed a data evaluation procedure for spectroscopic ellipsometry and transmission measurements as well as for reflection and transmission measurements in order to determine the complex refractive index $\hat{n}(\lambda)$ of optical materials. The first method has the higher accuracy, but also requires a very smooth sample surface so that changes to the phase of light can be detected. The second method is also capable of measuring samples with diffuse reflection characteristics.

With the second method, the reflectivity of back sheets of PV modules were measured that are covered with an EVA layer, as is the case in the module. The reflectivity at such an interface turned out to be higher than at the traditionally measured air/back sheet interface. The ray tracing analysis predicts that this traditional measurement approach leads to an underestimation of module peak power by around 0.2% compared to the more accurate measurement approach developed in this work.

A Monte-Carlo analysis was developed as a tool for quantifying measurement uncertainties of spectroscopic ellipsometry data. This method is utilized to systematically determine the optical properties of the most commonly used PV module components more specifically or, in case of new materials such as UV transmitting EVA_{UV-T}, for the first time. The results are all tabulated in the appendix B.

The iron concentration is known as the most important factor for the absorption in soda-lime glasses, and therefore such glasses with very low iron content are used for PV modules. In this thesis, special emphasis was given on characterizing the extinction coefficient k of soda-lime glass in dependence of iron content nearly two orders of magnitude lower than found in literature but widely used in the industry. Moreover, a semi-empirical model was developed for the extinction coefficient of soda-lime glasses as a function of iron concentration and wavelength.

In the simulation part, ray tracing is extended and utilized to predict the performance of various solar cell modules at standardized testing conditions (STC, am1.5g and T=25°C). The measurements obtained in the first part of this thesis were used as input. The losses

in a typical reference module producing 290.6 W are calculated in detail and potential improvements were discussed, as follows:

- The ray tracing analysis predicts that the use of UV-transparent EVA_{UV-T}, increases the output power of this typical solar cell module by 2 W compared to the traditionally used EVA_{UV-A},.

- Module output power declines with increasing iron content of the cover glass. Using the developed models the ray tracing analysis shows a decline between 1.5% (4 W) for an iron content equivalent to 0.1‰ Fe_2O_3 content and 13% (40 W) for 1‰ Fe_2O_3.

- Having an antireflective coating (ARC) on the front glass increases the module power output by about 5 W compared to a module with no ARC.

- Having a white back sheet with the measured reflectivity increases the module power output by about 8 W compared to a module with a perfectly black back sheet (reflectivity equal to zero).

- An investigation of colored PV modules reveals a decreased electrical power output compared to the traditional reference module with blue cell and white back sheet. The decrease in electrical power output amounts to 6 W for the completely blue and 11 W for the completely red module.

Despite all the improvements, however, the optical loss analysis conducted in this thesis predicts that the components with the biggest potential for future efficiency gain are:

- Lowering the absorption in the glass and the reflectivity of the ARC at its front surface.

- Improving the reflectivity and the scattering characteristics of the back sheet.

- Decreasing the amount of light that escapes the module after reflection at the front metalization.

- Improving the cell's rear side reflectivity with a scheme having a potential to exceed the lambertian limit, such as plasmonic nanoparticles.

For investigating nanoparticles, the Finite-Element-Method (FEM) was employed to characterize their scattering angles. Simulation results for differently shaped and sized nanoparticle were presented. Hemispherical particles with a diameter of (140 ± 20) nm are best suited for scattering at a Si-SiN_x interface at the simulated wavelengths of 1000 nm. Cylindrically and cone shaped particles have similar performance. Differently shaped nanoparticles react similarly to variations in the angle of incidence. However, there is a difference between the incoming s- and p-polarized light. A change in scattering characteristics occurs in the range between 12° and 18°.

However, module power output in field is lower than in STC due to the elevated operating temperatures influencing the semiconductor properties. In order to investigate module behavior in field conditions, a new FEM based model was developed that solves the thermal equations coupled with the semiconductor equations. This simulation model reproduces

the measurement data from an outdoor module test very well. In the field the vast majority of the time the wind speed is below 4 m/s, when there is at least 100 W/m^2 of incoming radiation. This reduces the cooling via forced convection (wind). Therefore, it is even more important to prevent increased module operating temperatures due to parasitic absorption.

The ray tracing analysis of different solar modules under the am1.5g spectrum between 300 nm and 2500 nm shows that about 18.9% of the irradiance becomes parasitically absorbed by a standard PV module with cells having a full-area rear metallization. Replacing it with PERC cells having a SiN$_x$ mirror lowers the parasitic absorbance to 11.7%, which leads to a 3.2 °C lower module operating temperature as calculated by this simulation model. This lower operating temperature causes a 5 W higher electrical power output (when considering a module with 262 W). With a conventional simulation approach that does not take the IR radiation into account, these considerable advantages would not have been noted. Therefore, it is advantageous to take also the module's thermal properties with wavelength resolution into account when optimizing solar cells and modules.

Bibliography

[Ade90]   ADES, C., T. TOGANIDIS, and J.P. TRAVERSE: 'High temperature optical spec-
           tra of soda-lime-silica glasses and modelization in view of energetic applications'.
           Journal of Non-Crystalline Solids (1990), vol. 125(3): pp. 272–279 (cit. on pp. 22,
           26).

[AT13]   AGILENT-TECHNOLOGIES: *Agilent diffuse reflectance accesories (DRAs) for the
           cary 4000/5000/6000i UV-VIS-NIR spectrometers.* 2013 (cit. on p. 14).

[Alt11]   ALTERMATT, PIETRO P.: 'Models for numerical device simulations of crystalline
           silicon solar cells - A review'. *Journal of Computational Electronics* (2011), vol.
           10(3): pp. 314–330 (cit. on pp. 74, 76).

[Alt97]   ALTERMATT, PIETRO P., PIETRO P. ALTERMATT, JAN SCHMIDT, JAN SCHMIDT,
           GERNOT HEISER, GERNOT HEISER, ARMIN G. ABERLE, and ARMIN G.
           ABERLE: 'Assessment and parameterisation of Coulomb-enhanced Auger recom-
           bination coefficients in lowly injected crystalline silicon'. *Journal of Applied
           Physics* (1997), vol. 82(10): p. 4938 (cit. on p. 76).

[Bel]   'April 25, 1954: Bell Labs Demonstrates the First Practical Silicon Solar Cell'.
           American Physical Society, This Month in Physics History (2009), vol. 18(4):
           p. 2 (cit. on p. 1).

[Arm10]   ARMSTRONG, S. and W. G. HURLEY: 'A thermal model for photovoltaic panels
           under varying atmospheric conditions'. *Applied Thermal Engineering* (2010),
           vol. 30(11-12): pp. 1488–1495 (cit. on pp. 78, 79, 86).

[Azz02]   AZZONI, C B, D D I MARTINO, C CHIAVARI, E SIBILIA, and M VANDINI:
           'Electron paramagentic resonance of mosaic glasses from the Mediterranean
           area'. *Archaeometry* (2002), vol. 4(May 2001): pp. 543–554 (cit. on p. 24).

[BF11]   BAKER-FINCH, SIMEON C. and KEITH R. MCINTOSH: 'Reflection of normally
           incident light from silicon solar cells with pyramidal texture'. *Progress in
           Photovoltaics: Research and Applications* (2011), vol. 19(4): pp. 406–416 (cit. on
           pp. 36, 46).

[Bas12]   BASCH, A., F. J. BECK, T. SÖDERSTRÖM, S. VARLAMOV, and K. R. CATCH-
           POLE: 'Combined plasmonic and dielectric rear reflectors for enhanced photocur-
           rent in solar cells'. *Applied Physics Letters* (2012), vol. 100(24): pp. 1–5 (cit. on
           pp. 60, 70).

[Bec11]   BECK, F J, E VERHAGEN, S MOKKAPATI, A POLMAN, and K R CATCHPOLE:
            'Resonant SPP modes supported by discrete metal nanoparticles on high-index
            substrates.' *Optics express* (2011), vol. 19 Suppl 2(March): A146–A156 (cit. on
            pp. 60, 65).

[Bej93]   BEJAN, ADRIAN: *Heat transfer.* John Wiley & Sons, Inc., 1993 (cit. on p. 79).

[Bin07]   BINGHAM, P. A., J. M. PARKER, T. M. SEARLE, and I. SMITH: 'Local structure
            and medium range ordering of tetrahedrally coordinated Fe3+ ions in alkali-
            alkaline earth-silica glasses'. *Journal of Non-Crystalline Solids* (2007), vol.
            353(24-25): pp. 2479–2494 (cit. on p. 22).

[Bin99]   BINGHAM, P. A., J. M. PARKER, T. SEARLE, J. M. WILLIAMS, and K. FYLES:
            'Redox and clustering of iron in silicate glasses'. *Journal of Non-Crystalline
            Solids* (1999), vol. 253(1-3): pp. 203–209 (cit. on p. 22).

[Bor99]   BORN, MAX and EMIL WOLF: *Principles of Optics.* 7th. Cambridge University
            Press, 1999 (cit. on pp. 7, 8).

[Bre93]   BRENDEL, ROLF: 'Simple prism pyramids: a new light trapping texture for
            silicon solar cells.' *Proc. 21st IEEE PV Specialists Conference.* Lousiville, 1993:
            pp. 252–255 (cit. on p. 45).

[Cat08]   CATCHPOLE, K. R. and A. POLMAN: 'Design principles for particle plasmon
            enhanced solar cells'. *Applied Physics Letters* (2008), vol. 93(19): pp. 1–4 (cit. on
            p. 64).

[Cat06]   CATCHPOLE, K. R. and S. PILLAI: 'Surface plasmons for enhanced silicon
            light-emitting diodes and solar cells'. *Journal of Luminescence* (2006), vol. 121(2
            SPEC. ISS.): pp. 315–318 (cit. on p. 60).

[Cat11]   CATCHPOLE, KYLIE R., SUDHA MOKKAPATI, FIONA BECK, ER-CHIEN WANG,
            ARNOLD MCKINLEY, ANGELIKA BASCH, and JARET LEE: 'Plasmonics and
            nanophotonics for photovoltaics'. *MRS Bulletin* (2011), vol. 36(06): pp. 461–467
            (cit. on p. 59).

[Che09]   CHEN, CHENG-YEN, JYH-YANG WANG, FU-JI TSAI, YEN-CHENG LU, YEAN-
            WOEI KIANG, and C C YANG: 'Fabrication of sphere-like Au nanoparticles on
            substrate with laser irradiation and their polarized localized surface plasmon
            behaviors.' *Optics express* (2009), vol. 17(16): pp. 14186–14198 (cit. on p. 60).

[Che12]   CHEN, YIFENG, YANG YANG, ZHIQIANG FENG, PIETRO. P. ALTERMATT, and
            HUI SHEN: 'Color modulation of c-Si solar cells without significant current-loss
            by means of a double-Layer anti-reflective coating'. *27th European Photovoltaic
            Solar Energy Conference and Exhibition.* 2012: pp. 2014–2016 (cit. on p. 54).

[Cle66]   CLEEK, G W: 'The optical constants of some oxide glasses in the strong
            absorption region.' *Applied optics* (1966), vol. 5(5): pp. 771–775 (cit. on p. 22).

[Dos97] DOSHI, P, G E JELLISON, and A ROHATGI: 'Characterization and optimization of absorbing plasma-enhanced chemical vapor deposited antireflection coatings for silicon photovoltaics.' *Applied optics* (1997), vol. 36(30): pp. 7826–7837 (cit. on pp. 36, 53).

[Dun12] DUNAEVA, E. S., E. BRUNET, S. MULLER, and I. A. USPENSKAYA: 'Thermodynamic modeling of redox equilibria in sodium silicate glasses with low iron content'. *Russian Journal of Inorganic Chemistry* (2012), vol. 57(10): pp. 1355–1361 (cit. on p. 21).

[Dup14] DUPRÉ, O. and R. VAILLON: 'Optimizations of photovoltaic cells including the minimization of internal heat sources'. *Journal of Renewable and Sustainable Energy* (2014), vol. 6(1) (cit. on p. 75).

[Dut12] DUTTAGUPTA, SHUBHAM, FAJUN MA, BRAM HOEX, THOMAS MUELLER, and ARMIN G. ABERLE: 'Optimised antireflection coatings using silicon nitride on textured silicon surfaces based on measurements and multidimensional modelling'. *Energy Procedia* (2012), vol. 15(2011): pp. 78–83 (cit. on pp. 36, 37, 53).

[Ess15] ESSIG, STEPHANIE, JAN BENICK, MICHAEL SCHACHTNER, ALEXANDER WEKKELI, MARTIN HERMLE, and FRANK DIMROTH: 'Wafer-Bonded GaInP / GaAs // Si Solar Cells With 30 % Efficiency Under Concentrated Sunlight'. *IEEE Journal of Photovoltaics* (2015), vol. 5(3): pp. 977–981 (cit. on p. 59).

[Far13] FARKAS, RÜDIGER: 'Plasmonische Kupfernanopartikel auf der Rückseite von Silizium'. Diplomarbeit. Leibniz Universität Hannover, 2013 (cit. on p. 63).

[Fuj03] FUJIWARA, H.: *Spectroscopic Ellipsometry*. Chicheser, UK: John Wiley & Sons, Ltd., 2003 (cit. on pp. 8, 9).

[Gra05] GRABOWSKI, A., M. NOWAK, and J. ŚLEZIONA: 'Optical and conductive properties of AlSi-alloy/SiCp composites: Application in modelling CO2 laser processing of composites'. *Optics and Lasers in Engineering* (2005), vol. 43(2): pp. 233–246 (cit. on p. 38).

[Gre08] GREEN, MARTIN A.: 'Self-consistent optical parameters of intrinsic silicon at 300 K including temperature coefficients'. *Solar Energy Materials and Solar Cells* (2008), vol. 92(11): pp. 1305–1310 (cit. on pp. 34, 63).

[Gre92] GREEN, MARTIN A.: *Solar Cells Operating Principles, technology and System Applications*. 2nd ed. Kensington: The University of New South Wales, 1992 (cit. on p. 73).

[Gue01] GUEYMARD, CHRISTIAN A.: 'Parameterized transmittance model for direct beam and circumsolar spectral irradiance'. *Solar Energy* (2001), vol. 71(5): pp. 325–346 (cit. on pp. 47, 48, 73, 81, 86, 115).

[Hau75] HAUGE, P.S. and F.H. DILL: 'A rotating-compensator fourier ellipsometer'. *Optics Communications* (1975), vol. 14(4): pp. 431–437 (cit. on p. 9).

[Her98]   HERZINGER, C.M., B. JOHS, W.A. MCGAHAN, J.A. WOOLLAM, and W. PAUL-
           SON: 'Ellipsometric determination of optical constants for silicon and thermally
           grown silicon dioxide via a investigation'. *Journal of Applied Physics* (1998),
           vol. 83(6): pp. 3323–3336 (cit. on pp. 34, 35).

[Hoa14]   HOANG, P., V. BOURDIN, Q. LIU, G. CARUSO, and V. ARCHAMBAULT: 'Cou-
           pling optical and thermal models to accurately predict PV panel electricity
           production'. *Solar Energy Materials and Solar Cells* (2014), vol. 125: pp. 325–
           338 (cit. on pp. 75, 78).

[Hol13]   HOLST, HENDRIK, MATTHIAS WINTER, MALTE R. VOGT, KARSTEN BOTHE,
           MARC KÖNTGES, ROLF BRENDEL, and PIETRO P. ALTERMATT: 'Application
           of a new ray tracing framework to the analysis of extended regions in Si solar
           cell modules'. *Energy Procedia* (2013), vol. 38: pp. 86–93 (cit. on pp. 1, 45, 79).

[ISE14]   ISE FRAUNHOFER: *Photovoltaics Report*. 2014 (cit. on p. 1).

[Jac11]   JACAK, W., J. KRASNYJ, J. JACAK, and L. JACAK: 'Plasmons in metallic
           nanospheres: Towards efficiency enhancement of metallic nano-modified solar
           cells'. *Optical Materials* (2011), vol. 33(9): pp. 1449–1452 (cit. on p. 60).

[Jag10]   JAGLARZ, JANUSZ and ANDRZEJ GRABOWSKI: 'Optical investigations of AlSi–SiC
           composites subjected to laser CO2 annealing'. *Optics and Lasers in Engineering*
           (2010), vol. 48(10): pp. 1038–1044 (cit. on p. 38).

[Jel96]   JELLISON, G. E. and F. A. MODINE: 'Parameterization of the optical functions
           of amorphous materials in the interband region'. *Applied Physics Letters* (1996),
           vol. 69(3): p. 371 (cit. on pp. 36, 37).

[Jel92]   JELLISON, G.E.: 'Optical functions of silicon determined by two-channel polar-
           ization modulation ellipsometry'. *Optical Materials* (1992), vol. 1(1): pp. 41–47
           (cit. on pp. 34, 35).

[Jin02]   JIN, JIAN-MING: *The finite element method in electromagnetics*. Wiley, 2002
           (cit. on p. 61).

[Joi08]   JOINT COMMITTEE FOR GUIDES IN METROLOGY.: 'Evaluation of measure-
           ment data — Supplement 1 to the "Guide to the expression of uncertainty in
           measurement" — Propagation of distributions using a Monte Carlo method'.
           Evaluation (2008), vol. JCGM 101:2(September) (cit. on p. 12).

[Ket08]   KETOLA, BARRY, KEITH R. MCINTOSH, ANN NORRIS, and MARY KAY TOMA-
           LIA: 'Silicones for Photovoltaic Encapsulation'. *23rd European Photovoltaic
           Solar Energy Conference*. Valencia, Spain, 2008: pp. 2969–2973 (cit. on pp. 30,
           52).

[Kho12]   KHOO, YONG SHENG, TIMOTHY M. WALSH, FEI LU, and ARMIN G. ABERLE:
           'Method for quantifying optical parasitic absorptance loss of glass and encap-
           sulant materials of silicon wafer based photovoltaic modules'. *Solar Energy
           Materials and Solar Cells* (2012), vol. 102: pp. 153–158 (cit. on p. 51).

[Kla92] KLAASSEN, D B M: 'Simulation–I . Model Equations and Concentration Dependence'. *Solid-State Electronics* (1992), vol. 35(7) (cit. on p. 76).

[Kra96] KRAUTER, S and R HANITSCH: 'Actual optical and thermal performance of PV-modules'. *Fuel and Energy Abstracts* (1996), vol. 37(6): p. 436 (cit. on pp. 75, 109, 113).

[Kra06] KRAUTER, S. and P. GRUNOW: 'Optical simulation to enhance PV module encapsulation'. *Proc. 4th World Conference on Photovoltaic Energy Conversion.* Waikoloa, Hawai, 2006: p. 2152 (cit. on pp. 46, 109).

[Kra93] KRAUTER, STEFAN: *Betriebsmodel der optischen, thermischen und elektrischen parameter von photovoltaischen Modulen.* 1993 (cit. on pp. 75, 78, 111).

[Lam60] LAMBERT, JOHANN HEINRICH: *Photometria, sive de Mensura et gradibus luminis, colorum et umbrae.* 1760 (cit. on p. 17).

[Lim07] LIM, S. H., W. MAR, P. MATHEU, D. DERKACS, and E. T. YU: 'Photocurrent spectroscopy of optical absorption enhancement in silicon photodiodes via scattering from surface plasmon polaritons in gold nanoparticles'. *Journal of Applied Physics* (2007), vol. 101(10) (cit. on p. 60).

[Mac01] MACLEOD, H. A.: *Thin-Film Opticla Filters.* 2001st ed. Bristol and Philadelphia: Institute of Physics Publishing, 2001 (cit. on p. 7).

[Mas14] MASUKO, K., M. SHIGEMATSU, T. HASHIGUCHI, D. FUJISHIMA, M. KAI, N. YOSHIMURA, T. YAMAGUCHI, Y. ICHIHASHI, T. MISHIMA, N. MATSUBARA, T. YAMANISHI, T. TAKAHAMA, M. TAGUCHI, E. MARUYAMA, and S. OKAMOTO: 'Achievement of more than 25% conversion efficiency with crystalline silicon heterojunction solar cell'. *IEEE Journal of Photovoltaics* (2014), vol. 4(6): pp. 1433–1435 (cit. on p. 1).

[McI09] McINTOSH, K. R., G. LAU, J. COTSELL, K. HANTON, D. BATZNER, F. BETTIOL, and B. RICHARDS: 'Increase in external quantum efficiency of encapsulated silicon solar cells from a luminescent down-shifting layer'. *Progress in Photovoltaics: Research and Applications* (2009), vol. (17): pp. 191–197 (cit. on p. 116).

[Mci09] MCINTOSH, KEITH R, JAMES N COTSELL, JEFF S CUMPSTON, ANN W NORRIS, NICK E POWELL, and BARRY M KETOLA: 'An optical comparison of silicone and EVA encapsulants for conventional silicon PV modules: A ray-tracing study'. *34th IEEE Photovoltaic Specialists Conference.* Philadelphia, 2009: pp. 544–549 (cit. on pp. 1, 31–33, 45, 52, 54, 82, 109, 116).

[Mcl10] MCLNTOSH, KEITH R., JAMES N. COTSELL, ANN W. NORRIS, NICK E. POWELL, and BARRY M. KETOLA: 'An optical comparison of silicone and EVA encapsulants under various spectra'. *Conference Record of the IEEE Photovoltaic Specialists Conference* (2010), vol.: pp. 269–274 (cit. on pp. 45, 82).

[Mok11] MOKKAPATI, S, F J BECK, R de WAELE, a POLMAN, and K R CATCHPOLE: 'Resonant nano-antennas for light trapping in plasmonic solar cells'. *Journal of Physics D: Applied Physics* (2011), vol. 44(18): p. 185101 (cit. on pp. 60, 67).

[Nag99]   NAGEL, H., A. G. ABERLE, and R HEZEL: 'Optimised antireflection coatings
          for planar silicon solar cells using remote PECVD silicon nitride and porous
          silicon dioxide.' *Progress in Photovoltaics: Research and Applications* (1999),
          vol. 4(7): pp. 245–260 (cit. on pp. 32, 36, 53).

[Nag02]   NAGEL, HENNING: 'Analyse und Reduktion der optischen und elektrischen Ver-
          luste in multikristallinen Silizium-Solarzellen'. PhD thesis. Universität Hannover,
          2002 (cit. on p. 38).

[Ngu14]   NGUYEN, HIEU T., FIACRE E. ROUGIEUX, BERNHARD MITCHELL, and DANIEL
          MACDONALD: 'Temperature dependence of the band-band absorption coefficient
          in crystalline silicon from photoluminescence'. *Journal of Applied Physics* (2014),
          vol. 115(4): p. 043710 (cit. on p. 76).

[Not05]   NOTTON, G., C. CRISTOFARI, M. MATTEI, and P. POGGI: 'Modelling of a
          double-glass photovoltaic module using finite differences'. *Applied Thermal
          Engineering* (2005), vol. 25(17-18): pp. 2854–2877 (cit. on p. 78).

[NRE15]   NREL: *Best research cell efficiencies.* 2015 (cit. on p. 1).

[Pal85]   PALIK, E. D.: *Handbook of Optical Constants of Solids.* Academic Press Inc.,
          1985 (cit. on pp. 29, 30, 48, 63, 119, 131).

[Pee14]   PEEST, CHRISTIAN P.: 'Bestimmung der Messunsicherheit eines Photospektrom-
          eters für Reflexions- und Transmissionsmessungen an planaren Siliziumwafern'.
          Master thesis. Leibniz Universität Hannover, 2014 (cit. on pp. 14, 15, 35).

[Pil07]   PILLAI, S., K. R. CATCHPOLE, T. TRUPKE, and M. A. GREEN: 'Surface
          plasmon enhanced silicon solar cells'. *Journal of Applied Physics* (2007), vol.
          101(9): pp. 1–8 (cit. on p. 60).

[Sin]   *Plasma-deposited SiNx (elipsometric measurments including T data) measured
          by A. Wolf (ISFH) and data analysis by P. P. Altermatt (LUH)* (cit. on p. 63).

[Pre92]   PRESS, W. H., B. P. FLANNERY, S. A. TEUKOLSKY, and W. T. VETTERLING:
          Numerical Recipes in C. 2nd. Cambridge University Press, 1992 (cit. on pp. 11,
          12).

[Pvm]   *PV Module Anatomy* (cit. on p. 3).

[RG07]   ROEKENS-GUIBERT, HILDE: *Next Generation Tedlar PVF Film for Photovoltaic
          Module Backsheets.* 2007 (cit. on pp. 40, 41).

[Rub85]   RUBIN, M.: 'Optical properties of soda lime silica glasses'. *Solar Energy Materials*
          (1985), vol. 12(4): pp. 275–288 (cit. on pp. 1, 21, 22, 27).

[Sch98]   SCHENK, ANDREAS and ANDREAS SCHENK: 'Finite-temperature full random-
          phase approximation model of band gap narrowing for silicon device simulation'.
          Journal of Applied Physics (1998), vol. 84(7): pp. 3684–3695 (cit. on p. 76).

[Sch15]   SCHINKE, CARSTEN, P. CHRISTIAN PEEST, JAN SCHMIDT, ROLF BRENDEL, KARSTEN BOTHE, MALTE R VOGT, INGO KRÖGER, STEFAN WINTER, ALFRED SCHIRMACHER, SIEW LIM, HIEU T. NGUYEN, and DANIEL MACDONALD: 'Uncertainty analysis for the coefficient of band-to-band absorption of crystalline silicon'. *AIP Advances* (2015), vol. 5(6): p. 067168 (cit. on pp. 13, 34, 36, 139).

[She80]   SHELBY, J.E. and J. VITKO: 'Surface characterization of weathered low-iron float glass'. *Journal of Non-Crystalline Solids* (1980), vol. 38(39): pp. 631–636 (cit. on p. 22).

[Shi80]   SHILES, E., TAIZO SASAKI, MITIO INOKUTI, and D. Y. SMITH: 'Self-consistency and sum-rule tests in the Kramers-Kronig analysis of optical data: Applications to aluminum'. *Physical Review B* (1980), vol. 22(4): pp. 1612–1628 (cit. on pp. 40, 48, 119, 144).

[Sho61]   SHOCKLEY, WILLIAM and HANS J. QUEISSER: 'Detailed balance limit of efficiency of p-n junction solar cells'. *Journal of Applied Physics* (1961), vol. 32(3): pp. 510–519 (cit. on p. 59).

[Sko09]   SKOPLAKI, E. and J. A. PALYVOS: 'On the temperature dependence of photovoltaic module electrical performance: A review of efficiency/power correlations'. *Solar Energy* (2009), vol. 83(5): pp. 614–624 (cit. on pp. 73, 76).

[Soi14]   SOITEC, CEA-LETI, and FRAUNHOFER ISE: *New world record for solar cell efficiency at 46%.* 2014 (cit. on p. 1).

[Stu96]   STUART, HOWARD R and DENNIS G HALL: 'Absorption enhancement in silicon-on-insulator waveguides using metal island films'. *Applied Physics Letters* (1996), vol. 69(16): pp. 2327–2329 (cit. on pp. 59, 60).

[Syn11]   SYNOWICKI, RON A., BLAINE D. JOHS, and ANDREW C. MARTIN: 'Optical properties of soda-lime float glass from spectroscopic ellipsometry'. *Thin Solid Films* (2011), vol. 519(9): pp. 2907–2913 (cit. on pp. 22, 29).

[The02]   THEODORE L. BERGMAN, ADRIENNE S. LAVINE, FRANK P. INCROPERA, DAVID P. DEWITT: *Fundamentals of Heat and Mass Transfer.* 5th. John Wiley & Sons, 2002 (cit. on p. 79).

[Tom05]   TOMPKINS, HARLAND G. and EUGENE A. IRENE: *Handbook of ellipsometry.* Ed. by TOMPKINS, HARLAND G. and EUGENE A. IRENE. William Andrew, 2005 (cit. on pp. 8, 9).

[Tra92]   TRAVERSE, J-P., T. TOGANIDIS, and C. ADES: 'Spectrophotometric analysis of ferrous, ferric and total iron content in soda-lime-silica glass'. *Glastechnische Berichte* (1992), vol. 65(8): pp. 201–206 (cit. on pp. 22, 25).

[Uch00]   UCHINO, TAKASHI, KUNIO NAKAGUCHI, YUKIHITO NAGASHIMA, and TOSHIKAZU KONDO: 'Prediction of optical properties of commercial soda-lime-silicate glasses containing iron'. *Journal of Non-Crystalline Solids* (2000), vol. 261(1): pp. 72–78 (cit. on p. 22).

[Vog11]   VOGT, M. R.: 'Simulation der streuenden Reflexion an Nanotröpfchen auf der Rückseite von Silizium-Solarzellen'. Master. Leibniz Universität Hannover, 2011 (cit. on pp. 7, 63).

[Vog14]   VOGT, M R, H HOLST, M WINTER, S KNOC, A RUPPENTHAL, R BRENDEL, and P P ALTERMATT: 'Optical loss analysis of colored PV modules'. *The 6th World Conference on Photovoltaic Energy Conversion.* Kyoto (Japan), 2014: pp. 1115–1116 (cit. on pp. 32, 54, 55, 82).

[Vog15a] VOGT, MALTE R., HENDRIK HOLST, MATTHIAS WINTER, ROLF BRENDEL, and PIETRO P. ALTERMAT: 'Numerical modeling of c-Si PV modules by coupling the semiconductor with the thermal conduction , convection and radiation equations'. *Energy Procedia* (2015), vol. Accepted (cit. on p. 74).

[Vog12]   VOGT, MALTE R., PIETRO P. ALTERMATT, and ROLF BRENDEL: 'Optimization of metallic nanoparticles for plasmon-enhanced scattering at the rear of c-Si solar cells'. *27th EUPVSEV 2012* (2012), vol. (May): pp. 9–11 (cit. on pp. 63, 67).

[Vog15b] VOGT, MALTE RUBEN, HARALD HAHN, HENDRIK HOLST, MATTHIAS WINTER, CARSTEN SCHINKE, MARC KONTGES, ROLF BRENDEL, and PIETRO P ALTERMATT: 'Measurement of the Optical Constants of Soda-Lime Glasses in Dependence of Iron Content and Modeling of Iron-Related Power Losses in Crystalline Si Solar Cell Modules'. *IEEE Journal of Photovoltaics* (2015), vol. (99): pp. 1–8 (cit. on pp. 13, 22, 50, 123).

[Whi67]   WHILLER, A.: *Design Factors Influencing Solar Collectors Low Temperature Engineering Applications for Solar Energy.* New York: ASHRAE, 1967 (cit. on p. 78).

[Win15]   WINTER, MATTHIAS, MALTE R VOGT, HENDRIK HOLST, and PIETRO P ALTERMATT: 'Combining structures on different length scales in ray tracing: analysis of optical losses in solar cell modules'. *Optical and Quantum Electronics* (2015), vol. 47(6): pp. 1373–1379 (cit. on pp. 45, 46, 56).

[Wol05]   WOLF, A., P. POHL, and R. BRENDEL: 'Determination of thermophysical properties of thin films for photovoltaic applications'. *Conference Record of the Thirty-first IEEE Photovoltaic Specialists Conference, 2005.* (2005), vol.: pp. 1749–1752 (cit. on p. 78).

[Woo10]   WOOLLAM, J. A. and CO.: *Manual for WVASE32.* J. A. Woollam Co. Inc., 2010 (cit. on pp. 8–11, 13, 22, 31).

[Wö05]   WÜRFEL, P: *Physics of Solar Cells.* Weinheim: WILEY-VCH, 2005 (cit. on p. 73).

[Yab82]   YABLONOVITCH, ELI: 'Statistical ray optics'. *Journal of the Optical Society of America* (1982), vol. 72(7): p. 899 (cit. on p. 56).

List of Figures

List of Tables

APPENDIX A

Characterizing the encapsulation material between two glass slabs

In the following the theory and measurement of encapsulant materials between two glass slabs is discussed. This is technique is a common evaluation technique for encapsulation material [Kra06; Mci09].

A.1 Theory

Analyzing the encapsulation material used in solar modules is challenging since the material is designed to be laminated in between the cells and the glass or the cells and the back sheet. Separating the materials after lamination can damage the materials surfaces, thereby impacting the results of the optical measurements. Moreover, during lamination the encapsulation materials are often in liquid phase, which potentially changes the optical properties so that one cannot measure the materials before lamination and expect them to have the same optical properties as afterwards. Therefore, the encapsulation materials are measured laminated in between two slabs of glass.

In the following the equations necessary to describe the reflection and transmission of such a system of three planar slabs are derived. For the transmission $\tau_{123}(\hat{n}_1, \hat{n}_2, \hat{n}_3, d_1, d_2, d_3, \theta_0)$ this can be found in [Kra96], but for reflection $\rho_{123}(\hat{n}_1, \hat{n}_2, \hat{n}_3, d_1, d_2, d_3, \theta_0)$ was derived for these experiments.

Reflection and transmission of two planar slabs

The situation for two planar slabs is illustrated in fig. A.1. The reflection ρ_{12} of this system of two slabs can be described as follows,

$$\rho_{12} = \rho_1 + \frac{\tau_1(\rho_2 - R_{12})\overline{\tau}_1}{T_{12}} + \frac{\tau_1(\rho_2 - R_{12})\overline{\tau}_1}{T_{12}} \frac{(\rho_2 - R_{12})\overline{\rho}_1}{T_{12}} + ... \tag{A.1a}$$

$$= \rho_1 + \frac{\tau_1(\rho_2 - R_{12})\overline{\tau}_1}{T_{12}} \times (1 + \frac{(\rho_2 - R_{12})\overline{\rho}_1}{T_{12}} + (\frac{(\rho_2 - R_{12})\overline{\rho}_1}{T_{12}})^2 + ...) \tag{A.1b}$$

$$= \rho_1 + \frac{\tau_1(\rho_2 - R_{12})\overline{\tau}_1}{T_{12}} \times \sum_{i=0}^{\infty} (\frac{(\rho_2 - R_{12})\overline{\rho}_1}{T_{12}})^i \tag{A.1c}$$

$$= \rho_1 + \frac{\tau_1(\rho_2 - R_{12})\overline{\tau}_1}{T_{12} - (\rho_2 - R_{12})\overline{\rho}_1} \tag{A.1d}$$

where $\overline{\tau}_1$ is the internal transmission from light that just entered the first slab coming from the second slab (see eq. A.2) and $\overline{\rho}_1$ internal reflexion from light that just entered the first slab coming from the second slab (see eq. A.3). Comparing ρ_{12} to ρ_1, one can see a similar pattern: ρ_1 replaces the surface reflection, one term which describes entry and exit from the system $\frac{\tau_1(\rho_2 - R_{12})\overline{\tau}_1}{T_{12}}$ and another term $\frac{(\rho_2 - R_{12})\overline{\rho}_1}{T_{12}}$ which describes the multiple reflections. It is necessary to divide through T_{12} to prevent the interface between slabs one and two from being included too often.
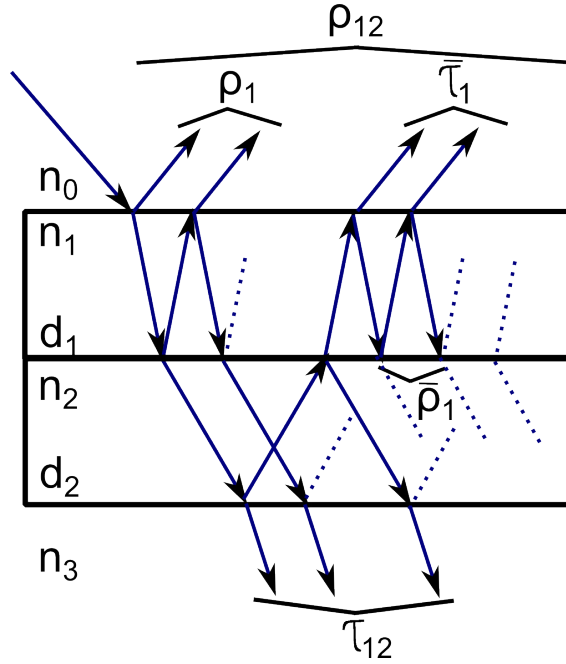
Figure A.1: The light is incoming and interacting with a system of two planar slabs. Here various light paths to reflection and transmission are illustrated considering multiple internal reflections.

The internal transmission $\overline{\tau}_1$ from light that just entered the first slab coming from the second slab is,

$$\overline{\tau}_1 = T_{10}e^{-\alpha_1\breve{d}_1} \times (1 + R_{10}e^{-2\alpha_1\breve{d}_1}R_{12} + (R_{12}e^{-2\alpha_1\breve{d}_1}R_{10})^2 + ...) \tag{A.2a}$$

$$= T_{10}e^{-\alpha_1\breve{d}_1} \times \sum_{i=0}^{\infty}(R_{10}e^{-2\alpha_1\breve{d}_1}R_{12})^i \tag{A.2b}$$

$$= \frac{T_{10}e^{-\alpha_1\breve{d}_1}}{1 - R_{10}e^{-2\alpha_1\breve{d}_1}R_{12}} \tag{A.2c}$$

and the internal reflexion $\overline{\rho}_1$ from light that just entered the first slab coming from the second slab is,

$$\overline{\rho}_1 = R_{10}e^{-2\alpha_1\breve{d}_1}T_{12} \times (1 + R_{12}e^{-2\alpha_1\breve{d}_1}R_{10} + (R_{12}e^{-2\alpha_1\breve{d}_1}R_{10})^2 + ...) \tag{A.3a}$$

$$= R_{10}e^{-2\alpha_1\breve{d}_1}T_{12} \times \sum_{i=0}^{\infty}(R_{12}e^{-2\alpha_1\breve{d}_1}R_{10})^i \tag{A.3b}$$

$$= \frac{R_{10}e^{-2\alpha_1\breve{d}_1}T_{12}}{1 - R_{12}e^{-2\alpha_1\breve{d}_1}R_{10}} \tag{A.3c}$$

with all the symbols having the same meaning as before. The transmission τ_{12} of the two slab system is as follows,

$$\tau_{12} = \frac{\tau_1\tau_2}{T_{12}} \times (1 + \frac{(\rho_2 - R_{12})\overline{\rho}_1}{T_{12}} + (\frac{(\rho_2 - R_{12})\overline{\rho}_1}{T_{12}})^2 + ...) \tag{A.4a}$$

$$= \frac{\tau_1\tau_2}{T_{12}} \times \sum_{i=0}^{\infty}(\frac{(\rho_2 - R_{12})\overline{\rho}_1}{T_{12}})^i \tag{A.4b}$$

$$= \frac{\tau_1\tau_2}{T_{12} - (\rho_2 - R_{12})\overline{\rho}_1} \tag{A.4c}$$

again the term $\frac{\tau_1\tau_2}{T_{12}}$ describe the entry and exit, while $\frac{(\rho_2-R_{12})\overline{\rho}_1}{T_{12}}$ describes the multiple reflexion between both slabs. These equations for τ_{12} and ρ_{12} (including $\overline{\rho}_1$ and $\overline{\tau}_1$) were derived by [Kra93, p.72-75].

Reflection and transmission of three planar slabs

The situation for three planar slabs is illustrated in fig. A.2. The reflection ρ_{123} of this system of three slabs can be described as follows,

$$\rho_{123} = \rho_{12} + \frac{\tau_{12}(\rho_3 - R_{23})\overline{\tau}_{21}}{T_{23}} + \frac{\tau_{12}(\rho_3 - R_{23})\overline{\tau}_{21}}{T_{23}} \times \frac{(\rho_3 - R_{23})\overline{\rho}_{21}}{T_{23}} + ... \tag{A.5a}$$

$$= \rho_{12} + \frac{\tau_{12}(\rho_3 - R_{23})\overline{\tau}_{21}}{T_{23}} \times (1 + \frac{(\rho_3 - R_{23})\overline{\rho}_{21}}{T_{23}} + (\frac{(\rho_3 - R_{23})\overline{\rho}_{21}}{T_{23}})^2 + ...)$$
$$\tag{A.5b}$$

$$= \rho_{12} + \frac{\tau_{12}(\rho_3 - R_{23})\overline{\tau}_{21}}{T_{23}} \times \sum_{i=0}^{\infty} (\frac{(\rho_3 - R_{23})\overline{\rho}_{21}}{T_{23}})^i \tag{A.5c}$$

$$= \rho_{12} + \frac{\tau_{12}(\rho_3 - R_{23})\overline{\tau}_{12}}{T_{23} - (\rho_3 - R_{23})\overline{\rho}_{21}} \tag{A.5d}$$

where $\overline{\tau}_{21}$ is the internal transmission from light that just entered the second slab coming from the third slab (see eq. A.6) and $\overline{\rho}_{21}$ internal reflexion from light that just entered the second slab coming from the third slab (see eq. A.7).
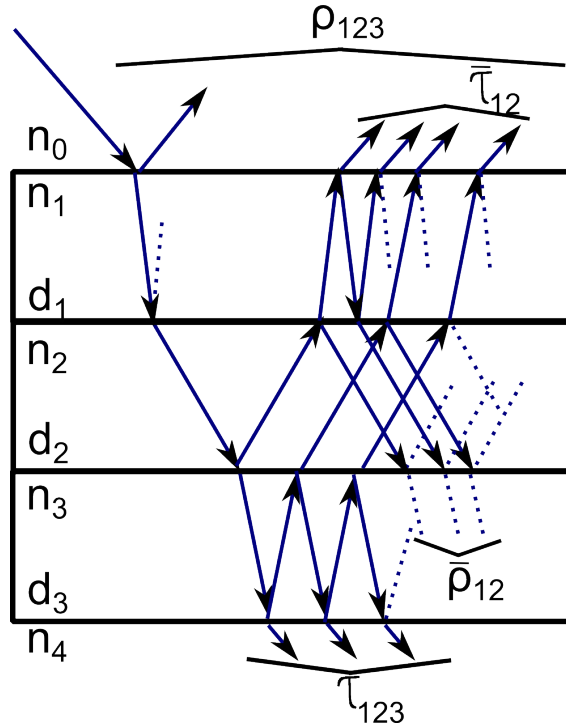
Figure A.2: The light is incoming and interacting with a system of three planar slabs. Here various light paths to reflection and transmission are illustrated considering multiple internal reflections.

The internal transmission $\overline{\tau}_{21}$ from light that just entered the second slab coming from the third slab is,

$$\overline{\tau}_{21} = \overline{\tau}_2\overline{\tau}_1 \times (1 + \frac{\overline{\rho}_1(\rho_2 - R_{12})}{T_{12}} + (\frac{\overline{\rho}_1(\rho_2 - R_{12})}{T_{12}})^2 + ...) \tag{A.6a}$$

$$= \overline{\tau}_2\overline{\tau}_1 \times \sum_{i=0}^{\infty}(\frac{\overline{\rho}_1(\rho_2 - R_{12})}{T_{12}})^i \tag{A.6b}$$

$$= \frac{\overline{\tau}_2\overline{\tau}_1 T_{12}}{T_{12} - \overline{\rho}_1(\rho_2 - R_{12})} \tag{A.6c}$$

and the internal reflexion $\overline{\rho}_{21}$ from light that just entered the second slab coming from the third slab is,

$$\overline{\rho}_{21} = \overline{\rho}_2 + \frac{\overline{\tau}_2\overline{\rho}_1\tau_2}{T_{12}} \times (1 + \frac{\overline{\rho}_1(\rho_2 - R_{12})}{T_{12}} + (\frac{\overline{\rho}_1(\rho_2 - R_{12})}{T_{12}})^2 + ...) \tag{A.7a}$$

$$= \overline{\rho}_2 + \frac{\overline{\tau}_2\overline{\rho}_1\tau_2}{T_{12}} \times \sum_{i=0}^{\infty}(\frac{\overline{\rho}_1(\rho_2 - R_{12})}{T_{12}})^i \tag{A.7b}$$

$$= \overline{\rho}_2 + \frac{\overline{\tau}_2\overline{\rho}_1\tau_2}{T_{12} - \overline{\rho}_1(\rho_2 - R_{12})} \tag{A.7c}$$

where $\overline{\tau}_2$ and $\overline{\rho}_2$ can be expressed via equations A.2 and A.3. The transmission τ_{123} of the three slab system is as follows,

$$\tau_{123} = \frac{\tau_{12}\tau_3}{T_{23}} \times \left(1 + \frac{(\rho_3 - R_{23})\overline{\rho}_{21}}{T_{23}} + (\frac{(\rho_3 - R_{23})\overline{\rho}_{21}}{T_{23}})^2 + ...\right) \tag{A.8a}$$

$$= \frac{\tau_{12}\tau_3}{T_{23}} \times \sum_{i=0}^{\infty}\left(\frac{(\rho_3 - R_{23})\overline{\rho}_{21}}{T_{23}}\right)^i \tag{A.8b}$$

$$= \frac{\tau_{12}\tau_3}{T_{23} - (\rho_3 - R_{23})\overline{\rho}_{21}} \tag{A.8c}$$

again the term $\frac{\tau_{12}\tau_3}{T_{23}}$ describes the entry and exit, while $\frac{(\rho_3-R_{23})\overline{\rho}_{21}}{T_{23}}$ describes the multiple reflexion between three slabs. Note when the third slab has the same material as the surroundings ($\hat{n}_3 = \hat{n}_4$), then the equations simplify to $\tau_{123} = \tau_{12}$ and $\rho_{123} = \rho_{12}$. The equations for τ_{123} and $\overline{\rho}_{21}$ were derived by [Kra96], while equations A.5 for ρ_{123} and for A.6 $\overline{\tau}_{21}$ were derived in this work.

Fitting reflection and transmission to determine optical properties

To describe a material in the optical simulation models in part II we need to know its refractive index $\hat{n}$. To simplify the dependency on n and k the following assumptions are

made, first that the light hits orthogonal to the sample's surface and second that $n >> k$, which leads to a simplification of the Fresnel equations:

$$R_{01} = \left(\frac{n_0 - n_1}{n_0 + n_1} \right)^2 \tag{A.9a}$$

$$T_{01} = \left(\frac{2n_0 n_1}{n_0 + n_1} \right)^2 \tag{A.9b}$$

For the one slab system equations 2.11 and 2.12 can just be solved for n_1 and k_1 analytically. Since sample preparation in case of encapsulation materials didn't allow for one slab systems, they are only analyzed as two and three slab systems. The equations describing those systems are to complicated to be solved for n_2 and k_2. Therefore, a fitting technique is used to determine n_2 and k_2 of the unknown layer. The fit's goal is,

$$\Delta\rho(\lambda) = |\rho_{mea}(\lambda) - \rho_{123}(n_2(\lambda), k_2(\lambda))| \tag{A.10a}$$

$$\Delta\tau(\lambda) = |\tau_{mea}(\lambda) - \tau_{123}(n_2(\lambda), k_2(\lambda))| \tag{A.10b}$$

to minimize $\Delta\rho(\lambda)$ and $\Delta\tau(\lambda)$ for each wavelength by adjusting $n_2(\lambda)$ and $k_2(\lambda)$. While the other slabs consist of glass, therefore their $n(\lambda)$ and $k(\lambda)$ are known from measurements of the glasses with spectroscopic ellipsometry.

The fitting process is automated and carried out in EXCEL after fitting the quotient of $\frac{\Delta\rho(\lambda)}{u(\rho_{mea}(\lambda))}$ and $\frac{\Delta\tau(\lambda)}{u(\tau_{mea}(\lambda))}$ are typically well below 0.01, which means that the fitting procedure is several orders of magnitude more accurate than the measurement with the uncertainty $u(\rho_{mea}(\lambda))$ and $u(\tau_{mea}(\lambda))$.

A.2 Measurements

In this section we are comparing the optical properties of four different materials with one sample each. For both EVA and silicone we have two samples, one sample with high absorption in the UV wavelength range (UV-A) and another sample with high transmission in the UV wavelength range (UV-T).

The encapsulation material before and after lamination looks already different to the human eye, therefore the sample preparation includes the lamination process. The sample with silicone$_{UV-T}$ consists of the UV-transparent silicone layer and a borosilicate glass below. All three others samples consists of the encapsulation material between two layers of glass.

The glasses are borosilicate glass with a surface of 5 cm $\times$ 5 cm and a thickness of 1.1 mm. These glasses were chosen, because they offer higher transmission in the UV than the
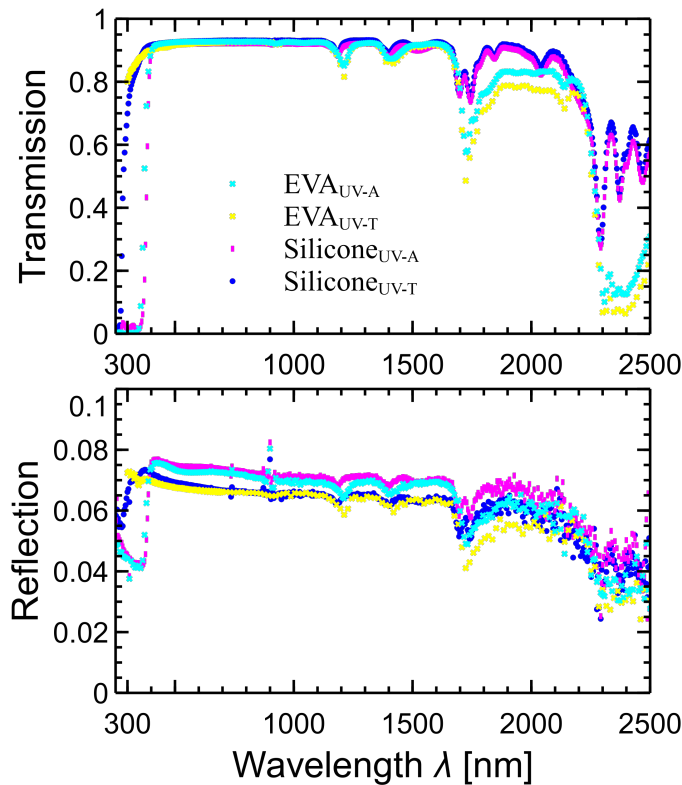
Figure A.3: The results of the transmission and reflection measurements conducted on the four different samples. The most relevant difference is the transmission in the wavelength range between 300 nm and 400 nm.

soda-lime glasses from Sec. 3.1. However, these borosilicate glasses are available as bigger flat glasses, which are necessary for 60 cell solar modules.

The surfaces of the encapsulation material are not smooth enough to allow for ellipsometry measurement, which require very smooth surfaces for the phase information to be preserved. Therefore reflection and transmission measurements as explained in Sec. 2.2 are conducted.

The results of these measurements are shown in Fig. A.3. All four samples have transmission above 90% between 400 nm and 1500 nm except for small absorption peaks at 1200 nm and 1400 nm. The most relevant difference is the transmission in the wavelength range between 250 nm and 400 nm. Both EVA_{UV-A} and $silicone_{UV-A}$ have a fast decline going from above 90% at 400 nm to essentially zero at 380 nm. While the EVA_{UV-T} and $silicone_{UV-T}$ also decline, they are both still above 70% in transmission at 300 nm, which corresponds to the lowest wavelengths still present in the suns spectrum at the earths surface [Gue01]. Note that both types of silicone are more transparent than the EVAs in the NIR between 1700 nm and 2500 nm.

In a separate step we measure τ_1 and ρ_1 of single layer borosilicate glass of the same type,

which is used for the samples. From this the we determine the borosilicate glasses optical
constants, by allying the data analysis from section A.1. With the glasses optical constants
determined we extract the n and k data from the measurements of τ_{123} and ρ_{123} of the
multilayer samples with different encapsulation material. Again making use of the data
analysis from section A.1.

A.2.1 Refractive index data and comparison with literature

Since n-values of glass and the encapsulation material are very similar, the reflection mostly
depends of the interfaces with air. Consequently, we are only able to obtain the n-value of
the silicone$_{UV-T}$, which is the only sample with an air/encapsulation material interface.
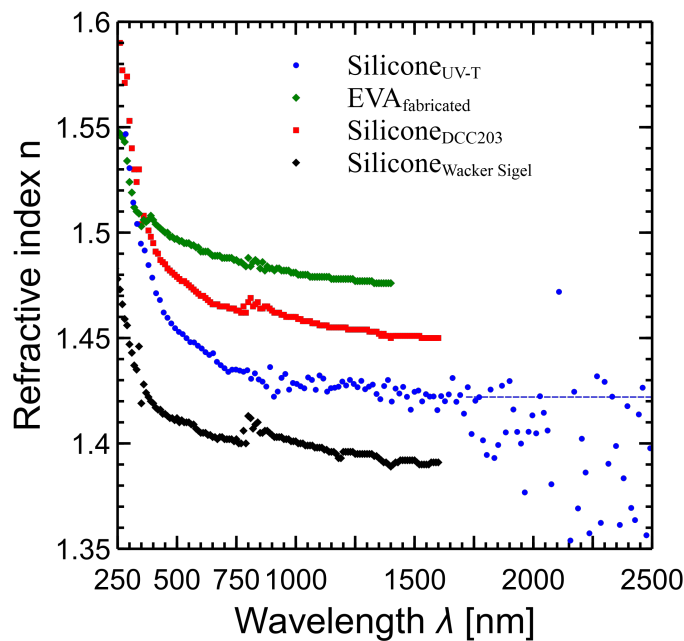
Figure A.4: The n-value of the silicone$_{UV-T}$, which is the only sample with the necessary
air/encapsulation material interface. In comparison with literature [McI09; Mci09] values for
other types of EVA and silicone.

Figure A.4 shows the n-value of the silicone$_{UV-T}$ in comparison with literature [McI09;
Mci09] values for other types of EVA and silicone. Our refractive index $n(\lambda)$ is between
the two curves for the silicone materials shown here. Due to the increased scattering the
reflection measurement above 1700 nm our refractive index data scatters considerably.
However, we assume that the real value is close to 1.42 as indicated by the dashed line. The
EVAs refractive index is closer to the one of glass around 1.5 in the relevant wavelength
range.
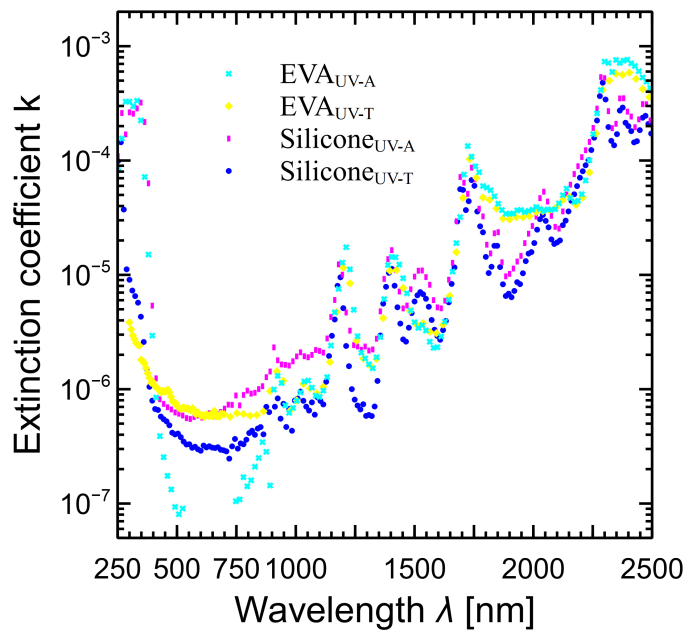
Figure A.5: Both UV absorbing materials have a strong increase in extinction coefficient for wavelength below about 400 nm. The position of the absorption peaks in the NIR appears to be independent of the UV transmittance of the materials.

A.2.2 Extinction coefficient of measured materials

Figure A.5 shows the k-value of encapsulation materials calculated from the reflexion and transmission measurements discussed around Fig. A.3. Both UV absorbing materials have a strong increase in extinction coefficient for wavelength below about 400 nm. The position of the absorption peaks in the NIR appears to be independent of the UV transmittance of the materials. The lowest extinction coefficients are reached in the visible part of the spectrum. In contrast to the results in Sec. 3.3 EVA_{UV-T} has higher extinction coefficients than Sil_{UV-T} and EVA_{UV-A}. This maybe caused by overestimation of one of the glasses transmittance.

APPENDIX B

Tables of the optical constants determined

The best values measured or available in literature are given in the following in tabulated form for further use. For descriptions of the measurements and discussions of the results please see Chapter 3.

For a modern high efficiency module with about 290 W at STC, this author uses the materials as listed in the table below. For results and discussions of these simulations please see Chapter 4.

Component	Material	Description	Table
Glass ARC	100 nm porose glass layer	Sec. 3.2	Tab. B.1
Glass	M1: Fe_2O_3 wt = 0.01‰	Sec. 3.1	Tab. B.2
Encapsulant	EVA_{UVT}	Sec. 3.3	Tab. B.3
Cell ARC	75 nm $SiN_{2.09}$	Sec. 3.5	Tab. B.5
Front metalization	Silver	[Pal85, p. 350-357]	Tab. B.4
Wafer	Silicon	Sec. 3.4	Tab. B.6
Cell rear side	Al-Si-eutectic	Sec.3.6	Tab. B.7
Frame	Aluminum	[Shi80]	Tab. B.8
Back sheet	EVA/Back sheet interface	Sec. 3.7	Tab. B.9

B.1 Glass ARC

Table B.1: Refractive index values of the ARC on soda-lime glass for PV modules. Measured on October 17, 2013 by the author of this work at ISFH using a Wollam 2000UI as described in Section 2.1.1. The extinction coefficient is assumed to be zero, which is an accurate assumption since no absorption was measured, for further details see Section 3.2.

λ [nm]	n	λ [nm]	n	λ [nm]	n	λ [nm]	n
250	1.504	620	1.414	990	1.405	1350	1.403
260	1.494	630	1.413	1000	1.405	1360	1.403
270	1.486	640	1.413	1010	1.405	1370	1.403
280	1.478	650	1.413	1020	1.405	1380	1.403
290	1.472	660	1.412	1030	1.405	1390	1.403
300	1.467	670	1.412	1040	1.405	1400	1.403
310	1.462	680	1.411	1050	1.405	1410	1.403
320	1.457	690	1.411	1060	1.405	1420	1.403
330	1.453	700	1.411	1070	1.405	1430	1.403
340	1.450	710	1.411	1080	1.405	1440	1.403
350	1.447	720	1.410	1090	1.404	1450	1.403
360	1.444	730	1.410	1100	1.404	1460	1.403
370	1.441	740	1.410	1110	1.404	1470	1.402
380	1.439	750	1.409	1120	1.404	1480	1.402
390	1.437	760	1.409	1130	1.404	1490	1.402
400	1.435	770	1.409	1140	1.404	1500	1.402
410	1.433	780	1.409	1150	1.404	1510	1.402
420	1.431	790	1.408	1160	1.404	1520	1.402
430	1.430	800	1.408	1170	1.404	1530	1.402
440	1.428	810	1.408	1180	1.404	1540	1.402
450	1.427	820	1.408	1190	1.404	1550	1.402
460	1.426	830	1.408	1200	1.404	1560	1.402
470	1.425	840	1.407	1210	1.404	1570	1.402
480	1.424	850	1.407	1220	1.404	1580	1.402
490	1.423	860	1.407	1230	1.404	1590	1.402
500	1.422	870	1.407	1240	1.403	1600	1.402
510	1.421	880	1.407	1250	1.403	1610	1.402
520	1.420	890	1.407	1260	1.403	1620	1.402

λ [nm]	n	λ [nm]	n	λ [nm]	n	λ [nm]	n
530	1.419	900	1.407	1270	1.403	1630	1.402
540	1.418	910	1.406	1280	1.403	1640	1.402
550	1.418	920	1.406	1290	1.403	1650	1.402
560	1.417	930	1.406	1300	1.403	1660	1.402
570	1.417	940	1.406	1310	1.403	1670	1.402
580	1.416	950	1.406	1320	1.403	1680	1.402
590	1.415	960	1.406	1330	1.403	1690	1.402
600	1.415	970	1.406	1340	1.403	1700	1.402
610	1.414	980	1.405				

B.2 Soda-lime glass

Table B.2: The n-value is the model-fit from Fig. 3.3 and the k-value is $k_{\mathrm{avg}}(\lambda)$ with an average iron content of $x_{\mathrm{avg}} \approx 0.7\permil$ intended for calculation according to the models described by equation 3.3, for further details see Section 3.1.

λ [nm]	n	k [10^{-6}]	λ [nm]	n	k [10^{-6}]	λ [nm]	n	k [10^{-6}]
300	1.557	57.9	770	1.508	1.61	1240	1.504	3.87
310	1.553	44.2	780	1.508	1.72	1250	1.504	3.85
320	1.549	25.3	790	1.508	1.81	1260	1.503	3.84
330	1.546	11.2	800	1.508	1.89	1270	1.503	3.82
340	1.543	4.19	810	1.507	1.99	1280	1.503	3.8
350	1.540	1.58	820	1.507	2.09	1290	1.503	3.78
360	1.538	0.822	830	1.507	2.19	1300	1.503	3.75
370	1.536	0.644	840	1.507	2.29	1310	1.503	3.73
380	1.534	0.607	850	1.507	2.38	1320	1.503	3.70
390	1.532	0.524	860	1.507	2.48	1330	1.503	3.67
400	1.530	0.396	870	1.507	2.57	1340	1.503	3.64
410	1.529	0.328	880	1.506	2.65	1350	1.503	3.61
420	1.527	0.318	890	1.506	2.73	1360	1.503	3.58
430	1.526	0.338	900	1.506	2.8	1370	1.503	3.55
440	1.525	0.350	910	1.506	2.87	1380	1.503	3.52
450	1.524	0.343	920	1.506	2.94	1390	1.503	3.49
460	1.523	0.330	930	1.506	3	1400	1.503	3.46

λ [nm]	n	k [10^{-6}]	λ [nm]	n	k [10^{-6}]	λ [nm]	n	k [10^{-6}]
470	1.522	0.301	940	1.506	3.06	1410	1.503	3.42
480	1.521	0.262	950	1.506	3.12	1420	1.503	3.38
490	1.520	0.239	960	1.506	3.17	1430	1.503	3.33
500	1.519	0.236	970	1.505	3.22	1440	1.503	3.28
510	1.518	0.236	980	1.505	3.27	1450	1.503	3.23
520	1.518	0.237	990	1.505	3.31	1460	1.503	3.18
530	1.517	0.235	1000	1.505	3.36	1470	1.503	3.12
540	1.516	0.233	1010	1.505	3.41	1480	1.503	3.08
550	1.516	0.243	1020	1.505	3.46	1490	1.503	3.03
560	1.515	0.266	1030	1.505	3.51	1500	1.503	2.99
570	1.515	0.311	1040	1.505	3.56	1510	1.503	2.95
580	1.514	0.355	1050	1.505	3.6	1520	1.503	2.92
590	1.514	0.381	1060	1.505	3.64	1530	1.503	2.89
600	1.513	0.406	1070	1.505	3.68	1540	1.503	2.85
610	1.513	0.447	1080	1.504	3.71	1550	1.503	2.82
620	1.512	0.494	1090	1.504	3.74	1560	1.502	2.77
630	1.512	0.537	1100	1.504	3.77	1570	1.502	2.73
640	1.512	0.578	1110	1.504	3.79	1580	1.502	2.69
650	1.511	0.652	1120	1.504	3.81	1590	1.502	2.65
660	1.511	0.735	1130	1.504	3.83	1600	1.502	2.61
670	1.511	0.78	1140	1.504	3.85	1610	1.502	2.57
680	1.510	0.821	1150	1.504	3.87	1620	1.502	2.55
690	1.510	0.888	1160	1.504	3.88	1630	1.502	2.53
700	1.510	0.975	1170	1.504	3.89	1640	1.502	2.53
710	1.510	1.05	1180	1.504	3.9	1650	1.502	2.55
720	1.509	1.11	1190	1.504	3.9	1660	1.502	2.60
730	1.509	1.21	1200	1.504	3.9	1670	1.502	2.66
740	1.509	1.32	1210	1.504	3.9	1680	1.502	2.73
750	1.509	1.41	1220	1.504	3.89	1690	1.502	2.81
760	1.508	1.50	1230	1.504	3.88			

Table B.3: The refractive index of a soda-lime glass according to model 1 with Fe_2O_3=0.01‰ from [Vog15b], for further details see [Vog15b] or Section 3.1. This data is used as standard front glass for PV modules.

λ [nm]	n	k [10^{-6}]	λ [nm]	n	k [10^{-6}]	λ [nm]	n	k [10^{-6}]
250	1.589	5.97	750	1.509	0.152	1250	1.504	0.415
260	1.582	6.12	760	1.508	0.162	1260	1.504	0.414
270	1.574	6.22	770	1.508	0.174	1270	1.503	0.412
280	1.568	6.42	780	1.508	0.185	1280	1.503	0.41
290	1.562	6.59	790	1.508	0.195	1290	1.503	0.408
300	1.557	6.24	800	1.508	0.204	1300	1.503	0.404
310	1.553	4.77	810	1.508	0.215	1310	1.503	0.402
320	1.549	2.73	820	1.507	0.225	1320	1.503	0.399
330	1.546	1.21	830	1.507	0.236	1330	1.503	0.396
340	1.543	0.452	840	1.507	0.247	1340	1.503	0.392
350	1.54	0.17	850	1.507	0.257	1350	1.503	0.389
360	1.538	0.089	860	1.507	0.267	1360	1.503	0.386
370	1.536	0.069	870	1.507	0.277	1370	1.503	0.383
380	1.534	0.066	880	1.506	0.286	1380	1.503	0.38
390	1.532	0.057	890	1.506	0.294	1390	1.503	0.376
400	1.53	0.043	900	1.506	0.302	1400	1.503	0.373
410	1.529	0.035	910	1.506	0.309	1410	1.503	0.369
420	1.527	0.034	920	1.506	0.317	1420	1.503	0.364
430	1.526	0.036	930	1.506	0.323	1430	1.503	0.359
440	1.525	0.038	940	1.506	0.33	1440	1.503	0.354
450	1.524	0.037	950	1.506	0.336	1450	1.503	0.348
460	1.523	0.036	960	1.506	0.342	1460	1.503	0.343
470	1.522	0.033	970	1.505	0.347	1470	1.503	0.336
480	1.521	0.028	980	1.505	0.353	1480	1.503	0.332
490	1.52	0.026	990	1.505	0.357	1490	1.503	0.327
500	1.519	0.025	1000	1.505	0.362	1500	1.503	0.322
510	1.518	0.025	1010	1.505	0.368	1510	1.503	0.318
520	1.518	0.026	1020	1.505	0.373	1520	1.503	0.315
530	1.517	0.025	1030	1.505	0.378	1530	1.503	0.312
540	1.516	0.025	1040	1.505	0.384	1540	1.503	0.307

λ [nm]	n	k [10^{-6}]	λ [nm]	n	k [10^{-6}]	λ [nm]	n	k [10^{-6}]
550	1.516	0.026	1050	1.505	0.388	1550	1.503	0.304
560	1.515	0.029	1060	1.505	0.392	1560	1.503	0.299
570	1.515	0.034	1070	1.505	0.397	1570	1.503	0.294
580	1.514	0.038	1080	1.505	0.4	1580	1.502	0.29
590	1.514	0.041	1090	1.504	0.403	1590	1.502	0.286
600	1.513	0.044	1100	1.504	0.407	1600	1.502	0.281
610	1.513	0.048	1110	1.504	0.409	1610	1.502	0.277
620	1.512	0.053	1120	1.504	0.411	1620	1.502	0.275
630	1.512	0.058	1130	1.504	0.413	1630	1.502	0.273
640	1.512	0.062	1140	1.504	0.415	1640	1.502	0.273
650	1.511	0.07	1150	1.504	0.417	1650	1.502	0.275
660	1.511	0.079	1160	1.504	0.418	1660	1.502	0.28
670	1.511	0.084	1170	1.504	0.419	1670	1.502	0.287
680	1.51	0.089	1180	1.504	0.421	1680	1.502	0.294
690	1.51	0.096	1190	1.504	0.421	1690	1.502	0.303
700	1.51	0.105	1200	1.504	0.421	1700	1.502	0.313
710	1.51	0.113	1210	1.504	0.421			
720	1.509	0.12	1220	1.504	0.419			
730	1.509	0.13	1230	1.504	0.418			
740	1.509	0.142	1240	1.504	0.417			

B.3 Encapsulatant materials

Table B.4: Refractive index values of UV-transmiiting EVA_{UV-T}, conventional EVA_{UV-A} and UV-transmiiting silicone for PV modules. Measured on June 19, 2015 by the author of this work at ISFH using a Wollam 2000UI and a a Varian Carry as described in Sections 2.1.1 and 2.2. For discussion of the measurements results see Section 3.3.

λ [nm]	n EVA_{UV-T}	k EVA_{UV-T} [10^{-6}]	n EVA_{UV-A}	k EVA_{UV-A} [10^{-6}]	n Sil_{UV-T}	k Sil_{UV-T} [10^{-6}]
250	1.557	9.86	1.562	11.27	1.505	10.80
260	1.551	9.70	1.555	11.59	1.493	11.40
270	1.545	8.20	1.549	16.36	1.482	13.73
280	1.540	6.64	1.543	19.95	1.473	12.56
290	1.536	5.31	1.538	21.31	1.466	8.81

λ [nm]	n EVA$_{\text{UV-T}}$	k EVA$_{\text{UV-T}}$ [10^{-6}]	n EVA$_{\text{UV-A}}$	k EVA$_{\text{UV-A}}$ [10^{-6}]	n Sil$_{\text{UV-T}}$	k Sil$_{\text{UV-T}}$ [10^{-6}]
300	1.532	3.89	1.533	22.29	1.461	6.79
310	1.528	3.11	1.529	25.93	1.456	5.66
320	1.525	2.64	1.525	29.04	1.452	4.69
330	1.522	2.28	1.522	27.49	1.449	3.77
340	1.519	1.95	1.519	29.44	1.446	3.15
350	1.517	1.56	1.517	31.36	1.444	2.63
360	1.515	1.27	1.514	30.69	1.442	2.34
370	1.513	1.07	1.512	28.21	1.440	2.06
380	1.511	0.95	1.510	13.64	1.438	1.84
390	1.510	0.86	1.508	5.52	1.437	1.66
400	1.508	0.78	1.507	2.50	1.435	1.52
410	1.507	0.74	1.505	1.51	1.434	1.43
420	1.506	0.70	1.504	1.11	1.433	1.34
430	1.505	0.66	1.503	0.95	1.432	1.28
440	1.504	0.63	1.502	0.88	1.431	1.22
450	1.503	0.60	1.501	0.83	1.430	1.17
460	1.502	0.58	1.500	0.79	1.429	1.13
470	1.501	0.55	1.499	0.76	1.429	1.10
480	1.500	0.53	1.498	0.73	1.428	1.08
490	1.499	0.51	1.497	0.71	1.427	1.06
500	1.499	0.49	1.496	0.68	1.427	1.03
510	1.498	0.47	1.496	0.66	1.426	1.01
520	1.497	0.45	1.495	0.64	1.426	1.00
530	1.497	0.43	1.494	0.61	1.425	0.98
540	1.496	0.42	1.494	0.60	1.425	0.96
550	1.496	0.40	1.493	0.58	1.424	0.95
560	1.495	0.39	1.493	0.56	1.424	0.93
570	1.495	0.37	1.492	0.54	1.424	0.92
580	1.494	0.36	1.492	0.53	1.423	0.91
590	1.494	0.35	1.491	0.51	1.423	0.90
600	1.493	0.33	1.491	0.50	1.423	0.88
610	1.493	0.32	1.490	0.48	1.423	0.87
620	1.493	0.31	1.490	0.47	1.422	0.86

λ [nm]	n EVA$_{\mathrm{UV-T}}$	k EVA$_{\mathrm{UV-T}}$ $[10^{-6}]$	n EVA$_{\mathrm{UV-A}}$	k EVA$_{\mathrm{UV-A}}$ $[10^{-6}]$	n Sil$_{\mathrm{UV-T}}$	k Sil$_{\mathrm{UV-T}}$ $[10^{-6}]$
630	1.492	0.30	1.490	0.46	1.422	0.86
640	1.492	0.30	1.489	0.45	1.422	0.84
650	1.492	0.29	1.489	0.43	1.422	0.83
660	1.491	0.27	1.489	0.42	1.421	0.82
670	1.491	0.26	1.488	0.40	1.421	0.81
680	1.491	0.26	1.488	0.39	1.421	0.81
690	1.491	0.25	1.488	0.38	1.421	0.80
700	1.490	0.24	1.488	0.37	1.421	0.79
710	1.490	0.24	1.487	0.36	1.420	0.78
720	1.490	0.23	1.487	0.36	1.420	0.78
730	1.490	0.23	1.487	0.35	1.420	0.79
740	1.490	0.24	1.487	0.36	1.420	0.79
750	1.489	0.25	1.487	0.37	1.420	0.77
760	1.489	0.26	1.486	0.37	1.420	0.75
770	1.489	0.24	1.486	0.35	1.420	0.73
780	1.489	0.21	1.486	0.32	1.419	0.73
790	1.489	0.19	1.486	0.30	1.419	0.72
800	1.488	0.19	1.486	0.29	1.419	0.72
810	1.488	0.19	1.486	0.29	1.419	0.72
820	1.488	0.20	1.485	0.30	1.419	0.71
830	1.488	0.20	1.485	0.30	1.419	0.71
840	1.488	0.20	1.485	0.30	1.419	0.71
850	1.488	0.19	1.485	0.29	1.419	0.71
860	1.488	0.19	1.485	0.29	1.419	0.72
870	1.487	0.19	1.485	0.29	1.418	0.72
880	1.487	0.22	1.485	0.31	1.418	0.75
890	1.487	0.29	1.484	0.38	1.418	0.84
900	1.487	0.39	1.484	0.47	1.418	1.02
910	1.487	0.56	1.484	0.63	1.418	1.18
920	1.487	0.84	1.484	0.88	1.418	1.04
930	1.487	1.05	1.484	1.07	1.418	0.76
940	1.487	0.93	1.484	0.96	1.418	0.74
950	1.487	0.53	1.484	0.58	1.418	0.64

λ [nm]	n EVA$_{\mathrm{UV-T}}$	k EVA$_{\mathrm{UV-T}}$ $[10^{-6}]$	n EVA$_{\mathrm{UV-A}}$	k EVA$_{\mathrm{UV-A}}$ $[10^{-6}]$	n Sil$_{\mathrm{UV-T}}$	k Sil$_{\mathrm{UV-T}}$ $[10^{-6}]$
960	1.487	0.27	1.484	0.34	1.418	0.64
970	1.486	0.22	1.484	0.29	1.418	0.64
980	1.486	0.20	1.483	0.28	1.418	0.65
990	1.486	0.23	1.483	0.30	1.418	0.71
1000	1.486	0.30	1.483	0.37	1.418	0.80
1010	1.486	0.40	1.483	0.46	1.418	0.92
1020	1.486	0.50	1.483	0.55	1.417	0.97
1030	1.486	0.60	1.483	0.64	1.417	0.89
1040	1.486	0.67	1.483	0.71	1.417	0.78
1050	1.486	0.63	1.483	0.67	1.417	0.72
1060	1.486	0.53	1.483	0.58	1.417	0.72
1070	1.486	0.44	1.483	0.49	1.417	0.76
1080	1.486	0.37	1.483	0.42	1.417	0.83
1090	1.486	0.33	1.483	0.38	1.417	0.87
1100	1.486	0.31	1.483	0.36	1.417	0.82
1110	1.485	0.34	1.483	0.39	1.417	0.76
1120	1.485	0.43	1.482	0.48	1.417	0.83
1130	1.485	0.64	1.482	0.67	1.417	1.19
1140	1.485	1.08	1.482	1.10	1.417	1.92
1150	1.485	1.99	1.482	1.96	1.417	2.75
1160	1.485	3.31	1.482	3.22	1.417	3.49
1170	1.485	4.83	1.482	4.65	1.417	5.34
1180	1.485	6.59	1.482	6.32	1.417	8.49
1190	1.485	9.23	1.482	8.83	1.417	8.27
1200	1.485	13.05	1.482	12.45	1.417	4.84
1210	1.485	15.88	1.482	15.09	1.417	2.86
1220	1.485	13.42	1.482	12.81	1.417	2.10
1230	1.485	8.47	1.482	8.13	1.417	1.51
1240	1.485	5.03	1.482	4.83	1.417	1.11
1250	1.485	3.26	1.482	3.15	1.417	0.99
1260	1.485	2.32	1.482	2.25	1.417	0.97
1270	1.485	1.82	1.482	1.78	1.417	1.00
1280	1.485	1.53	1.482	1.51	1.417	1.02

λ [nm]	n EVA$_{UV-T}$	k EVA$_{UV-T}$ [10^{-6}]	n EVA$_{UV-A}$	k EVA$_{UV-A}$ [10^{-6}]	n Sil$_{UV-T}$	k Sil$_{UV-T}$ [10^{-6}]
1290	1.485	1.35	1.482	1.33	1.416	0.99
1300	1.485	1.21	1.482	1.20	1.416	0.94
1310	1.485	1.08	1.482	1.08	1.416	0.91
1320	1.485	1.00	1.482	1.00	1.416	0.92
1330	1.484	1.04	1.482	1.04	1.416	1.03
1340	1.484	1.26	1.481	1.25	1.416	1.26
1350	1.484	1.79	1.481	1.76	1.416	2.02
1360	1.484	2.66	1.481	2.59	1.416	3.68
1370	1.484	4.44	1.481	4.31	1.416	5.95
1380	1.484	7.21	1.481	6.94	1.416	7.40
1390	1.484	10.37	1.481	9.93	1.416	9.30
1400	1.484	11.57	1.481	11.06	1.416	10.60
1410	1.484	12.01	1.481	11.47	1.416	9.02
1420	1.484	12.27	1.481	11.71	1.416	6.38
1430	1.484	11.53	1.481	11.01	1.416	4.69
1440	1.484	10.17	1.481	9.71	1.416	3.65
1450	1.484	8.63	1.481	8.25	1.416	3.02
1460	1.484	7.16	1.481	6.86	1.416	2.89
1470	1.484	5.80	1.481	5.57	1.416	3.22
1480	1.484	4.66	1.481	4.48	1.416	4.07
1490	1.484	3.89	1.481	3.74	1.416	5.30
1500	1.484	3.40	1.481	3.27	1.416	6.35
1510	1.484	3.19	1.481	3.07	1.416	7.09
1520	1.484	3.18	1.481	3.07	1.416	7.58
1530	1.484	3.29	1.481	3.17	1.416	7.60
1540	1.484	3.24	1.481	3.11	1.416	7.26
1550	1.484	2.86	1.481	2.76	1.416	6.66
1560	1.484	2.47	1.481	2.39	1.416	5.82
1570	1.484	2.25	1.481	2.19	1.416	4.77
1580	1.484	2.15	1.481	2.09	1.416	3.89
1590	1.484	2.18	1.481	2.12	1.416	3.46
1600	1.484	2.30	1.481	2.23	1.416	3.32
1610	1.484	2.56	1.481	2.48	1.416	3.37

λ [nm]	n EVA$_{\text{UV-T}}$	k EVA$_{\text{UV-T}}$ [10^{-6}]	n EVA$_{\text{UV-A}}$	k EVA$_{\text{UV-A}}$ [10^{-6}]	n Sil$_{\text{UV-T}}$	k Sil$_{\text{UV-T}}$ [10^{-6}]
1620	1.484	3.01	1.481	2.91	1.416	3.67
1630	1.484	3.78	1.481	3.65	1.416	4.50
1640	1.484	4.94	1.481	4.77	1.416	5.98
1650	1.484	6.79	1.481	6.54	1.416	7.80
1660	1.484	9.65	1.481	9.31	1.416	9.50
1670	1.484	13.85	1.481	13.33	1.416	12.74
1680	1.484	18.89	1.481	18.14	1.416	20.64
1690	1.484	24.96	1.481	23.96	1.416	37.02
1700	1.484	34.57	1.481	33.43	1.416	48.30
1710	1.484	52.86	1.481	51.60	1.416	36.44
1720	1.484	86.09	1.481	86.97	1.416	32.52
1730	1.484	98.02	1.481	98.85	1.416	40.48
1740	1.484	86.94	1.481	80.62	1.416	58.26
1750	1.484	81.21	1.481	78.18	1.416	52.16
1760	1.484	82.05	1.481	79.62	1.416	35.33
1770	1.484	72.28	1.481	68.54	1.416	28.46
1780	1.484	61.48	1.481	58.23	1.416	26.57
1790	1.483	57.19	1.481	54.20	1.416	21.42
1800	1.483	56.43	1.480	53.45	1.416	14.45
1810	1.483	55.82	1.480	52.92	1.416	10.68
1820	1.483	53.17	1.480	50.66	1.416	10.68
1830	1.483	49.97	1.480	47.39	1.416	14.03
1840	1.483	45.59	1.480	43.26	1.416	18.28
1850	1.483	41.28	1.480	39.21	1.416	17.64
1860	1.483	37.79	1.480	35.84	1.416	12.52
1870	1.483	35.04	1.480	33.31	1.416	8.22
1880	1.483	33.73	1.480	32.23	1.416	6.63
1890	1.483	34.11	1.480	32.67	1.416	6.66
1900	1.483	34.57	1.480	33.21	1.416	7.06
1910	1.483	34.55	1.480	33.33	1.416	7.59
1920	1.483	34.66	1.480	33.26	1.416	8.15
1930	1.483	35.51	1.480	33.84	1.416	8.79
1940	1.483	36.19	1.480	34.49	1.416	9.42

λ [nm]	n EVA$_{\text{UV}-\text{T}}$	k EVA$_{\text{UV}-\text{T}}$ [10^{-6}]	n EVA$_{\text{UV}-\text{A}}$	k EVA$_{\text{UV}-\text{A}}$ [10^{-6}]	n Sil$_{\text{UV}-\text{T}}$	k Sil$_{\text{UV}-\text{T}}$ [10^{-6}]
1950	1.483	35.53	1.480	33.75	1.416	10.25
1960	1.483	34.49	1.480	32.71	1.416	11.76
1970	1.483	33.91	1.480	32.26	1.416	13.67
1980	1.483	33.91	1.480	32.31	1.416	15.14
1990	1.483	34.70	1.480	32.95	1.416	16.56
2000	1.483	36.09	1.480	34.38	1.416	17.89
2010	1.483	36.65	1.480	34.88	1.416	20.20
2020	1.483	35.75	1.480	33.74	1.416	25.04
2030	1.483	34.56	1.480	32.72	1.416	31.42
2040	1.483	34.52	1.480	32.76	1.416	34.65
2050	1.483	34.62	1.480	32.83	1.416	31.92
2060	1.483	34.30	1.480	32.82	1.416	26.31
2070	1.483	33.84	1.480	32.19	1.416	21.18
2080	1.483	33.83	1.480	32.18	1.416	17.74
2090	1.483	35.29	1.480	33.70	1.416	16.44
2100	1.483	37.37	1.480	35.34	1.416	16.73
2110	1.483	39.04	1.480	37.10	1.415	18.24
2120	1.483	41.47	1.480	39.72	1.415	20.66
2130	1.483	47.17	1.480	44.82	1.415	24.66
2140	1.483	51.04	1.480	48.18	1.415	29.69
2150	1.483	45.38	1.480	43.18	1.415	35.43
2160	1.483	41.01	1.480	39.18	1.415	42.24
2170	1.483	40.08	1.480	38.00	1.415	49.32
2180	1.483	40.21	1.480	38.57	1.415	57.43
2190	1.483	41.26	1.480	39.49	1.415	64.42
2200	1.483	43.96	1.480	42.06	1.415	70.71
2210	1.483	49.94	1.480	47.58	1.415	79.22
2220	1.483	58.10	1.480	55.46	1.415	87.47
2230	1.483	71.85	1.480	69.07	1.415	98.84
2240	1.483	90.11	1.480	88.88	1.415	116.07
2250	1.483	157.40	1.480	157.40	1.415	137.24
2260	1.483	210.64	1.480	210.64	1.415	174.39
2270	1.483	269.98	1.480	269.98	1.415	237.00

λ [nm]	n EVA$_{UV-T}$	k EVA$_{UV-T}$ [10^{-6}]	n EVA$_{UV-A}$	k EVA$_{UV-A}$ [10^{-6}]	n Sil$_{UV-T}$	k Sil$_{UV-T}$ [10^{-6}]
2280	1.483	358.59	1.480	358.59	1.415	365.83
2290	1.483	517.80	1.480	517.80	1.415	468.77
2300	1.483	733.92	1.480	733.92	1.415	400.41
2310	1.483	811.95	1.480	811.95	1.415	256.71
2320	1.483	654.15	1.480	654.15	1.415	173.59
2330	1.483	594.92	1.480	594.92	1.415	143.37
2340	1.483	668.72	1.480	668.72	1.415	135.91
2350	1.483	758.16	1.480	758.16	1.415	162.11
2360	1.483	734.99	1.480	734.99	1.415	235.17
2370	1.483	706.42	1.480	706.42	1.415	299.82
2380	1.483	746.97	1.480	746.97	1.415	263.00
2390	1.483	755.67	1.480	755.67	1.415	208.68
2400	1.483	750.47	1.480	750.47	1.415	200.03
2410	1.483	714.21	1.480	714.21	1.415	187.52
2420	1.483	684.04	1.480	684.04	1.415	153.53
2430	1.483	662.68	1.480	662.68	1.415	144.01
2440	1.483	621.17	1.480	621.17	1.415	158.08
2450	1.483	577.93	1.480	577.93	1.415	193.53
2460	1.483	532.66	1.480	532.66	1.415	236.71
2470	1.483	503.06	1.480	503.06	1.415	246.71
2480	1.483	465.08	1.480	465.08	1.415	221.44
2490	1.483	444.59	1.480	444.59	1.415	191.09
2500	1.483	418.79	1.480	418.79	1.415	169.96

B.4 Cell front side metalization (Ag)

Table B.5: Refractive index of Ag derived from [Pal85, p. 350-357].

λ [nm]	n Si	k Si	λ [nm]	n Si	k Si
250	1.307	1.350	1050	0.231	7.113
260	1.352	1.350	1060	0.233	7.185
270	1.407	1.328	1070	0.236	7.258
280	1.466	1.274	1080	0.239	7.330

λ [nm]	n Si	k Si	λ [nm]	n Si	k Si
290	1.506	1.163	1090	0.241	7.402
300	1.513	0.955	1100	0.244	7.475
310	1.323	0.647	1110	0.246	7.547
320	0.794	0.534	1120	0.249	7.619
330	0.393	0.792	1130	0.253	7.692
340	0.258	1.128	1140	0.260	7.764
350	0.221	1.354	1150	0.267	7.837
360	0.196	1.534	1160	0.274	7.909
370	0.193	1.639	1170	0.281	7.982
380	0.197	1.721	1180	0.288	8.055
390	0.188	1.838	1190	0.294	8.127
400	0.173	1.950	1200	0.301	8.200
410	0.173	2.070	1210	0.308	8.272
420	0.167	2.181	1220	0.315	8.345
430	0.160	2.283	1230	0.322	8.417
440	0.158	2.374	1240	0.329	8.490
450	0.151	2.470	1250	0.347	8.206
460	0.143	2.567	1260	0.366	7.922
470	0.137	2.658	1270	0.377	7.807
480	0.132	2.746	1280	0.380	7.861
490	0.131	2.830	1290	0.383	7.915
500	0.130	2.918	1300	0.367	8.582
510	0.130	3.009	1310	0.370	8.632
520	0.130	3.097	1320	0.392	8.065
530	0.129	3.177	1330	0.395	8.117
540	0.129	3.257	1340	0.399	8.169
550	0.125	3.339	1350	0.402	8.221
560	0.121	3.421	1360	0.405	8.274
570	0.120	3.500	1370	0.408	8.327
580	0.121	3.579	1380	0.412	8.370
590	0.121	3.657	1390	0.415	8.370
600	0.124	3.732	1400	0.418	8.370
610	0.128	3.806	1410	0.421	8.380
620	0.131	3.881	1420	0.424	8.480

λ [nm]	n Si	k Si	λ [nm]	n Si	k Si
630	0.134	3.963	1430	0.427	8.580
640	0.137	4.046	1440	0.430	8.680
650	0.139	4.129	1450	0.438	9.359
660	0.140	4.209	1460	0.446	10.028
670	0.140	4.289	1470	0.443	9.311
680	0.140	4.370	1480	0.443	8.902
690	0.140	4.449	1490	0.447	8.958
700	0.142	4.523	1500	0.451	9.013
710	0.144	4.597	1510	0.454	9.069
720	0.146	4.671	1520	0.458	9.131
730	0.148	4.745	1530	0.462	9.194
740	0.147	4.822	1540	0.465	9.257
750	0.146	4.899	1550	0.469	9.320
760	0.145	4.976	1560	0.473	9.383
770	0.144	5.052	1570	0.477	9.445
780	0.143	5.130	1580	0.481	9.508
790	0.144	5.210	1590	0.485	9.570
800	0.144	5.289	1600	0.489	9.636
810	0.144	5.368	1610	0.493	9.702
820	0.145	5.448	1620	0.497	9.768
830	0.146	5.526	1630	0.501	9.833
840	0.149	5.602	1640	0.551	10.519
850	0.152	5.678	1650	0.607	11.274
860	0.155	5.755	1660	0.591	11.055
870	0.158	5.831	1670	0.543	10.418
880	0.161	5.907	1680	0.521	10.132
890	0.165	5.981	1690	0.525	10.196
900	0.170	6.051	1700	0.529	10.260
910	0.176	6.122			
920	0.181	6.192			
930	0.186	6.263			
940	0.191	6.333			
950	0.196	6.404			
960	0.200	6.474			

λ [nm]	n Si	k Si	λ [nm]	n Si	k Si
970	0.204	6.545			
980	0.207	6.616			
990	0.211	6.686			
1000	0.214	6.757			
1010	0.218	6.828			
1020	0.221	6.898			
1030	0.225	6.969			
1040	0.228	7.041			

B.5 Cell ARC (SiN)

Table B.6: Refractive index values of SiN as ARC for solar cells. Measured on June 30, 2014 by the author of this work at ISFH using a Wollam 2000UI as described in Section 2.1.1. The SiN samples are named for their their refractive index at 633 nm, for further discussions of the measurements results see Section 3.5.

λ [nm]	n SiN$_{1.91}$	k SiN$_{1.91}$ $[10^{-3}]$	n SiN$_{2.09}$	k SiN$_{2.09}$ $[10^{-3}]$	n SiN$_{2.13}$	k SiN$_{2.13}$ $[10^{-3}]$
250	2.191	89.1	2.459	246.5	2.515	350.0
260	2.157	69.3	2.426	203.1	2.510	304.8
270	2.129	54.7	2.396	168.7	2.497	261.8
280	2.105	43.7	2.369	141.1	2.479	223.4
290	2.085	35.2	2.345	118.6	2.458	190.3
300	2.067	28.5	2.323	100.1	2.437	162.2
310	2.051	23.2	2.303	84.6	2.416	138.4
320	2.037	18.8	2.285	71.6	2.395	118.4
330	2.025	15.3	2.269	60.6	2.376	101.5
340	2.014	12.4	2.254	51.2	2.358	87.1
350	2.004	10.0	2.241	43.2	2.340	74.9
360	1.995	8.0	2.228	36.3	2.324	64.4
370	1.987	6.3	2.217	30.3	2.310	55.4
380	1.980	4.9	2.206	25.2	2.296	47.6
390	1.973	3.8	2.196	20.8	2.283	40.9
400	1.967	2.8	2.187	17.0	2.271	35.0
410	1.961	2.0	2.179	13.7	2.260	29.9

λ [nm]	n SiN$_{1.91}$	k SiN$_{1.91}$ [10^{-3}]	n SiN$_{2.09}$	k SiN$_{2.09}$ [10^{-3}]	n SiN$_{2.13}$	k SiN$_{2.13}$ [10^{-3}]
420	1.956	1.4	2.171	10.9	2.249	25.5
430	1.952	0.9	2.163	8.5	2.239	21.6
440	1.947	0.6	2.156	6.5	2.230	18.2
450	1.943	0.3	2.150	4.8	2.222	15.2
460	1.939	0.1	2.144	3.4	2.214	12.7
470	1.936	0.0	2.138	2.3	2.206	10.4
480	1.933	0	2.133	1.4	2.199	8.4
490	1.930	0	2.128	0.8	2.193	6.8
500	1.927	0	2.124	0.3	2.186	5.3
510	1.925	0	2.119	0.1	2.181	4.1
520	1.923	0	2.115	0	2.175	3.0
530	1.921	0	2.112	0	2.170	2.2
540	1.919	0	2.109	0	2.165	1.5
550	1.917	0	2.106	0	2.160	0.9
560	1.915	0	2.103	0	2.156	0.5
570	1.913	0	2.101	0	2.152	0.2
580	1.912	0	2.099	0	2.148	0.1
590	1.910	0	2.096	0	2.145	0
600	1.909	0	2.094	0	2.141	0
610	1.908	0	2.092	0	2.138	0
620	1.907	0	2.091	0	2.136	0
630	1.905	0	2.089	0	2.133	0
640	1.904	0	2.087	0	2.131	0
650	1.903	0	2.086	0	2.128	0
660	1.902	0	2.084	0	2.126	0
670	1.901	0	2.083	0	2.124	0
680	1.900	0	2.082	0	2.122	0
690	1.900	0	2.081	0	2.120	0
700	1.899	0	2.079	0	2.118	0
710	1.898	0	2.078	0	2.117	0
720	1.897	0	2.077	0	2.115	0
730	1.897	0	2.076	0	2.114	0
740	1.896	0	2.075	0	2.112	0

λ [nm]	n SiN$_{1.91}$	k SiN$_{1.91}$ [10^{-3}]	n SiN$_{2.09}$	k SiN$_{2.09}$ [10^{-3}]	n SiN$_{2.13}$	k SiN$_{2.13}$ [10^{-3}]
750	1.895	0	2.074	0	2.111	0
760	1.895	0	2.074	0	2.109	0
770	1.894	0	2.073	0	2.108	0
780	1.893	0	2.072	0	2.107	0
790	1.893	0	2.071	0	2.106	0
800	1.892	0	2.070	0	2.105	0
810	1.892	0	2.070	0	2.104	0
820	1.891	0	2.069	0	2.103	0
830	1.891	0	2.068	0	2.102	0
840	1.890	0	2.068	0	2.101	0
850	1.890	0	2.067	0	2.100	0
860	1.889	0	2.067	0	2.099	0
870	1.889	0	2.066	0	2.098	0
880	1.889	0	2.066	0	2.097	0
890	1.888	0	2.065	0	2.097	0
900	1.888	0	2.065	0	2.096	0
910	1.888	0	2.064	0	2.095	0
920	1.887	0	2.064	0	2.094	0
930	1.887	0	2.063	0	2.094	0
940	1.887	0	2.063	0	2.093	0
950	1.886	0	2.062	0	2.092	0
960	1.886	0	2.062	0	2.092	0
970	1.886	0	2.062	0	2.091	0
980	1.885	0	2.061	0	2.091	0
990	1.885	0	2.061	0	2.090	0
1000	1.885	0	2.060	0	2.090	0
1010	1.885	0	2.060	0	2.089	0
1020	1.884	0	2.060	0	2.089	0
1030	1.884	0	2.059	0	2.088	0
1040	1.884	0	2.059	0	2.088	0
1050	1.884	0	2.059	0	2.087	0
1060	1.883	0	2.059	0	2.087	0
1070	1.883	0	2.058	0	2.086	0

λ [nm]	n SiN$_{1.91}$	k SiN$_{1.91}$ [10^{-3}]	n SiN$_{2.09}$	k SiN$_{2.09}$ [10^{-3}]	n SiN$_{2.13}$	k SiN$_{2.13}$ [10^{-3}]
1080	1.883	0	2.058	0	2.086	0
1090	1.883	0	2.058	0	2.085	0
1100	1.882	0	2.057	0	2.085	0
1110	1.882	0	2.057	0	2.085	0
1120	1.882	0	2.057	0	2.084	0
1130	1.882	0	2.057	0	2.084	0
1140	1.882	0	2.056	0	2.084	0
1150	1.881	0	2.056	0	2.083	0
1160	1.881	0	2.056	0	2.083	0
1170	1.881	0	2.056	0	2.083	0
1180	1.881	0	2.056	0	2.082	0
1190	1.881	0	2.055	0	2.082	0
1200	1.881	0	2.055	0	2.082	0
1210	1.880	0	2.055	0	2.081	0
1220	1.880	0	2.055	0	2.081	0
1230	1.880	0	2.055	0	2.081	0
1240	1.880	0	2.054	0	2.080	0
1250	1.880	0	2.054	0	2.080	0
1260	1.880	0	2.054	0	2.080	0
1270	1.879	0	2.054	0	2.080	0
1280	1.879	0	2.054	0	2.079	0
1290	1.879	0	2.054	0	2.079	0
1300	1.879	0	2.053	0	2.079	0
1310	1.879	0	2.053	0	2.079	0
1320	1.879	0	2.053	0	2.079	0
1330	1.879	0	2.053	0	2.078	0
1340	1.879	0	2.053	0	2.078	0
1350	1.878	0	2.053	0	2.078	0
1360	1.878	0	2.053	0	2.078	0
1370	1.878	0	2.052	0	2.078	0
1380	1.878	0	2.052	0	2.077	0
1390	1.878	0	2.052	0	2.077	0
1400	1.878	0	2.052	0	2.077	0

λ [nm]	n SiN$_{1.91}$	k SiN$_{1.91}$ [10^{-3}]	n SiN$_{2.09}$	k SiN$_{2.09}$ [10^{-3}]	n SiN$_{2.13}$	k SiN$_{2.13}$ [10^{-3}]
1410	1.878	0	2.052	0	2.077	0
1420	1.878	0	2.052	0	2.077	0
1430	1.877	0	2.052	0	2.076	0
1440	1.877	0	2.052	0	2.076	0
1450	1.877	0	2.052	0	2.076	0
1460	1.877	0	2.051	0	2.076	0
1470	1.877	0	2.051	0	2.076	0
1480	1.877	0	2.051	0	2.076	0
1490	1.877	0	2.051	0	2.075	0
1500	1.877	0	2.051	0	2.075	0
1510	1.877	0	2.051	0	2.075	0
1520	1.877	0	2.051	0	2.075	0
1530	1.876	0	2.051	0	2.075	0
1540	1.876	0	2.051	0	2.075	0
1550	1.876	0	2.051	0	2.075	0
1560	1.876	0	2.050	0	2.074	0
1570	1.876	0	2.050	0	2.074	0
1580	1.876	0	2.050	0	2.074	0
1590	1.876	0	2.050	0	2.074	0
1600	1.876	0	2.050	0	2.074	0
1610	1.876	0	2.050	0	2.074	0
1620	1.876	0	2.050	0	2.074	0
1630	1.876	0	2.050	0	2.074	0
1640	1.875	0	2.050	0	2.073	0
1650	1.875	0	2.050	0	2.073	0
1660	1.875	0	2.050	0	2.073	0
1670	1.875	0	2.050	0	2.073	0
1680	1.875	0	2.050	0	2.073	0
1690	1.875	0	2.049	0	2.073	0
1700	1.875	0	2.049	0	2.073	0

B.6 Silicon

Table B.7: Si extinction coefficient derived from the absorption coefficient as published in [Sch15]. Real part of the refractive index as determined in this work, for further details see Section 3.4.

λ [nm]	n Si	k Si	λ [nm]	n Si	k Si
250	1.637	3.589E+00	1050	3.559	1.305E-04
260	1.737	3.993E+00	1060	3.556	9.230E-05
270	2.030	4.596E+00	1070	3.553	6.780E-05
280	2.840	5.197E+00	1080	3.549	5.210E-05
290	4.185	5.312E+00	1090	3.547	3.970E-05
300	5.049	4.290E+00	1100	3.545	3.020E-05
310	5.091	3.625E+00	1110	3.542	2.290E-05
320	5.085	3.282E+00	1120	3.540	1.700E-05
330	5.135	3.092E+00	1130	3.537	1.240E-05
340	5.245	2.959E+00	1140	3.534	8.620E-06
350	5.423	2.908E+00	1150	3.533	5.680E-06
360	5.914	2.914E+00	1160	3.530	3.420E-06
370	6.820	2.140E+00	1170	3.527	1.760E-06
380	6.587	9.840E-01	1180	3.526	5.550E-07
390	6.025	5.031E-01	1190	3.524	2.310E-07
400	5.623	3.264E-01	1200	3.522	1.390E-07
410	5.341	2.413E-01	1210	3.520	8.080E-08
420	5.110	1.770E-01	1220	3.518	4.790E-08
430	4.932	1.377E-01	1230	3.517	2.710E-08
440	4.790	1.120E-01	1240	3.515	1.430E-08
450	4.673	9.536E-02	1250	3.513	5.870E-09
460	4.572	7.910E-02	1260	3.512	2.330E-09
470	4.485	7.025E-02	1270	3.509	1.270E-09
480	4.412	5.981E-02	1280	3.509	7.520E-10
490	4.349	5.380E-02	1290	3.506	4.480E-10
500	4.289	4.855E-02	1300	3.505	2.720E-10
510	4.235	4.385E-02	1310	3.503	1.580E-10
520	4.187	3.953E-02	1320	3.502	8.710E-11

λ [nm]	n Si	k Si	λ [nm]	n Si	k Si
530	4.145	3.481E-02	1330	3.501	4.200E-11
540	4.103	2.990E-02	1340	3.500	1.810E-11
550	4.073	2.804E-02	1350	3.499	1.040E-11
560	4.038	2.655E-02	1360	3.497	6.280E-12
570	4.006	2.374E-02	1370	3.496	3.900E-12
580	3.977	2.190E-02	1380	3.496	2.630E-12
590	3.954	2.008E-02	1390	3.496	1.740E-12
600	3.931	1.852E-02	1400	3.493	1.040E-12
610	3.908	1.726E-02	1410	3.492	6.040E-13
620	3.888	1.681E-02	1420	3.492	0
630	3.869	1.627E-02	1430	3.490	0
640	3.851	1.469E-02	1440	3.488	0
650	3.835	1.445E-02	1450	3.487	0
660	3.817	1.361E-02	1460	3.486	0
670	3.805	1.281E-02	1470	3.486	0
680	3.791	1.205E-02	1480	3.485	0
690	3.776	1.132E-02	1490	3.483	0
700	3.765	1.062E-02	1500	3.483	0
710	3.753	9.963E-03	1510	3.482	0
720	3.741	9.332E-03	1520	3.480	0
730	3.730	8.732E-03	1530	3.479	0
740	3.719	8.159E-03	1540	3.480	0
750	3.712	7.614E-03	1550	3.479	0
760	3.701	7.096E-03	1560	3.477	0
770	3.693	6.603E-03	1570	3.476	0
780	3.684	6.134E-03	1580	3.476	0
790	3.677	5.688E-03	1590	3.476	0
800	3.669	5.265E-03	1600	3.475	0
810	3.662	4.864E-03	1610	3.474	0
820	3.655	4.484E-03	1620	3.472	0
830	3.646	4.123E-03	1630	3.472	0
840	3.641	3.783E-03	1640	3.471	0
850	3.636	3.460E-03	1650	3.470	0

λ [nm]	n Si	k Si	λ [nm]	n Si	k Si
860	3.628	3.156E-03	1660	3.471	0
870	3.622	2.870E-03	1670	3.471	0
880	3.617	2.600E-03	1680	3.470	0
890	3.613	2.347E-03	1690	3.477	0
900	3.610	2.109E-03	1700	3.483	0
910	3.604	1.886E-03			
920	3.598	1.679E-03			
930	3.597	1.481E-03			
940	3.590	1.311E-03			
950	3.584	1.144E-03			
960	3.584	9.867E-04			
970	3.578	8.438E-04			
980	3.582	7.152E-04			
990	3.579	5.995E-04			
1000	3.575	4.923E-04			
1010	3.572	3.982E-04			
1020	3.568	3.150E-04			
1030	3.565	2.415E-04			
1040	3.562	1.799E-04			

B.7 Cell rear side metalization (Al-Si)

Table B.8: Refractive index of Al-Si eutectic as determined and used in this work for further details see Section 3.6.

λ [nm]	n Al-Si	k Al-Si	λ [nm]	n Al-Si	k Al-Si
250	0.386	2.992	1050	1.532	8.629
260	0.411	3.157	1060	1.522	8.742
270	0.465	3.349	1070	1.512	8.855
280	0.589	3.541	1080	1.504	8.966
290	0.787	3.666	1090	1.502	9.069
300	0.920	3.630	1100	1.500	9.172
310	0.941	3.650	1110	1.497	9.276
320	0.957	3.711	1120	1.495	9.379

λ [nm]	n Al-Si	k Al-Si	λ [nm]	n Al-Si	k Al-Si
330	0.980	3.794	1130	1.494	9.480
340	1.013	3.878	1140	1.495	9.574
350	1.054	3.974	1150	1.497	9.669
360	1.140	4.086	1160	1.498	9.763
370	1.281	4.083	1170	1.499	9.857
380	1.269	4.029	1180	1.501	9.952
390	1.213	4.069	1190	1.500	10.039
400	1.178	4.147	1200	1.500	10.126
410	1.161	4.236	1210	1.500	10.232
420	1.150	4.333	1220	1.500	10.339
430	1.147	4.432	1230	1.499	10.445
440	1.150	4.528	1240	1.499	10.551
450	1.157	4.629	1250	1.502	10.642
460	1.167	4.729	1260	1.504	10.733
470	1.180	4.833	1270	1.506	10.823
480	1.195	4.935	1280	1.509	10.914
490	1.213	5.036	1290	1.511	11.004
500	1.232	5.139	1300	1.513	11.095
510	1.254	5.238	1310	1.516	11.186
520	1.277	5.342	1320	1.520	11.280
530	1.303	5.446	1330	1.523	11.373
540	1.331	5.542	1340	1.526	11.466
550	1.362	5.649	1350	1.530	11.559
560	1.396	5.749	1360	1.533	11.652
570	1.431	5.847	1370	1.536	11.745
580	1.467	5.942	1380	1.541	11.838
590	1.507	6.034	1390	1.548	11.932
600	1.547	6.129	1400	1.555	12.026
610	1.584	6.221	1410	1.562	12.120
620	1.626	6.316	1420	1.569	12.213
630	1.672	6.406	1430	1.576	12.307
640	1.717	6.494	1440	1.583	12.401
650	1.763	6.578	1450	1.590	12.495
660	1.816	6.670	1460	1.598	12.590

λ [nm]	n Al-Si	k Al-Si	λ [nm]	n Al-Si	k Al-Si
670	1.867	6.761	1470	1.608	12.692
680	1.928	6.851	1480	1.618	12.794
690	1.990	6.940	1490	1.628	12.896
700	2.056	7.014	1500	1.638	12.998
710	2.137	7.094	1510	1.649	13.100
720	2.228	7.166	1520	1.658	13.201
730	2.321	7.236	1530	1.668	13.303
740	2.425	7.256	1540	1.679	13.404
750	2.530	7.276	1550	1.689	13.506
760	2.605	7.270	1560	1.701	13.596
770	2.683	7.263	1570	1.713	13.685
780	2.750	7.233	1580	1.725	13.775
790	2.806	7.183	1590	1.737	13.865
800	2.862	7.132	1600	1.749	13.955
810	2.844	7.085	1610	1.762	14.045
820	2.826	7.037	1620	1.774	14.135
830	2.792	7.003	1630	1.786	14.225
840	2.744	6.970	1640	1.798	14.314
850	2.696	6.938	1650	1.810	14.404
860	2.629	6.923	1660	1.823	14.491
870	2.543	6.911	1670	1.836	14.577
880	2.445	6.916	1680	1.848	14.663
890	2.335	6.953	1690	1.862	14.749
900	2.227	7.007	1700	1.876	14.834
910	2.136	7.070			
920	2.041	7.133			
930	1.938	7.229			
940	1.842	7.361			
950	1.746	7.494			
960	1.714	7.629			
970	1.691	7.748			
980	1.670	7.868			
990	1.647	7.987			
1000	1.625	8.087			

λ [nm]	n Al-Si	k Al-Si	λ [nm]	n Al-Si	k Al-Si
1010	1.602	8.193			
1020	1.579	8.300			
1030	1.556	8.406			
1040	1.541	8.517			

B.8 Module frame (Al)

Table B.9: Refractive index of Al derived from [Shi80] used as material for simulating the module's frame and for deriving the optical properties of Al-Si eutectic at the rear of solar cells, for further details see Section 3.6.

λ [nm]	n Al	k Al	λ [nm]	n Al	k Al
250	0.193	2.966	1050	1.241	10.224
260	0.208	3.097	1060	1.230	10.358
270	0.224	3.228	1070	1.219	10.492
280	0.241	3.358	1080	1.210	10.623
290	0.258	3.488	1090	1.208	10.745
300	0.276	3.610	1100	1.206	10.868
310	0.294	3.740	1110	1.203	10.990
320	0.314	3.868	1120	1.201	11.113
330	0.334	3.996	1130	1.201	11.232
340	0.355	4.118	1140	1.202	11.344
350	0.375	4.240	1150	1.204	11.456
360	0.397	4.372	1160	1.206	11.567
370	0.419	4.493	1170	1.208	11.679
380	0.442	4.615	1180	1.210	11.791
390	0.466	4.741	1190	1.210	11.895
400	0.490	4.861	1200	1.210	11.998
410	0.515	4.981	1210	1.210	12.123
420	0.540	5.105	1220	1.210	12.250
430	0.564	5.229	1230	1.210	12.376
440	0.591	5.347	1240	1.210	12.502
450	0.618	5.470	1250	1.213	12.609
460	0.646	5.590	1260	1.216	12.716

continued on next page . . .

λ [nm]	n Al	k Al	λ [nm]	n Al	k Al
470	0.675	5.715	1270	1.219	12.824
480	0.705	5.838	1280	1.222	12.931
490	0.736	5.958	1290	1.225	13.038
500	0.769	6.081	1300	1.228	13.145
510	0.803	6.199	1310	1.232	13.254
520	0.839	6.323	1320	1.236	13.364
530	0.876	6.447	1330	1.240	13.475
540	0.916	6.562	1340	1.244	13.585
550	0.958	6.689	1350	1.249	13.695
560	1.004	6.807	1360	1.253	13.806
570	1.049	6.924	1370	1.257	13.916
580	1.097	7.036	1380	1.262	14.027
590	1.148	7.146	1390	1.271	14.138
600	1.199	7.259	1400	1.279	14.249
610	1.248	7.368	1410	1.288	14.360
620	1.300	7.481	1420	1.297	14.471
630	1.357	7.588	1430	1.305	14.582
640	1.414	7.692	1440	1.314	14.693
650	1.471	7.792	1450	1.323	14.804
660	1.536	7.900	1460	1.332	14.916
670	1.599	8.008	1470	1.344	15.038
680	1.674	8.115	1480	1.356	15.159
690	1.750	8.221	1490	1.368	15.280
700	1.829	8.309	1500	1.380	15.401
710	1.927	8.403	1510	1.392	15.521
720	2.037	8.490	1520	1.404	15.641
730	2.149	8.572	1530	1.416	15.762
740	2.274	8.596	1540	1.428	15.882
750	2.399	8.620	1550	1.440	16.002
760	2.490	8.613	1560	1.455	16.109
770	2.584	8.604	1570	1.469	16.215
780	2.665	8.569	1580	1.484	16.322
790	2.733	8.509	1590	1.498	16.428
800	2.800	8.449	1600	1.513	16.534

λ [nm]	n Al	k Al	λ [nm]	n Al	k Al
810	2.780	8.393	1610	1.527	16.641
820	2.760	8.337	1620	1.542	16.747
830	2.721	8.297	1630	1.556	16.854
840	2.665	8.258	1640	1.571	16.960
850	2.609	8.220	1650	1.585	17.067
860	2.530	8.203	1660	1.600	17.170
870	2.430	8.187	1670	1.616	17.272
880	2.314	8.194	1680	1.631	17.373
890	2.184	8.238	1690	1.646	17.475
900	2.057	8.302	1700	1.661	17.576
910	1.950	8.377			
920	1.839	8.452			
930	1.716	8.565			
940	1.604	8.722			
950	1.491	8.879			
960	1.454	9.039			
970	1.427	9.180			
980	1.401	9.322			
990	1.375	9.463			
1000	1.350	9.582			
1010	1.323	9.708			
1020	1.296	9.834			
1030	1.269	9.960			
1040	1.252	10.091			

B.9 Back sheet

Table B.10: Diffuse refrectivity of a back sheet for PV modules, once at an interface with conventional EVA_{UV-A} and once at an interface with Air. Measured on Febuary 26, 2013 by the author of this work at ISFH using a Varian Carry as described in Section 2.2.1. The reflectivity at the air/back sheet interface was measured directly, while the reflectivity at the EVA/back sheet interface was calculated from an measurement via theory derived in this work, for further details see Section 3.7.

λ [nm]	R Air/Back sheet	R EVA/Back sheet	λ [nm]	R Air/Back sheet	R EVA/Back sheet
300	0.06	0.00	800	0.83	0.84
310	0.06	0.00	810	0.82	0.84
320	0.06	0.00	820	0.82	0.84
330	0.06	0.00	830	0.82	0.84
340	0.06	0.00	840	0.82	0.83
350	0.07	0.00	850	0.81	0.83
360	0.08	0.00	860	0.81	0.83
370	0.10	0.00	870	0.81	0.83
380	0.15	0.17	880	0.80	0.82
390	0.25	0.27	890	0.80	0.82
400	0.48	0.51	900	0.80	0.82
410	0.75	0.78	910	0.80	0.81
420	0.85	0.89	920	0.79	0.80
430	0.87	0.91	930	0.79	0.79
440	0.88	0.91	940	0.78	0.79
450	0.88	0.91	950	0.79	0.80
460	0.88	0.91	960	0.79	0.80
470	0.88	0.91	970	0.78	0.80
480	0.88	0.91	980	0.78	0.80
490	0.88	0.91	990	0.77	0.79
500	0.88	0.91	1000	0.77	0.79
510	0.88	0.91	1010	0.77	0.79
520	0.88	0.91	1020	0.76	0.78
530	0.88	0.91	1030	0.76	0.78
540	0.88	0.91	1040	0.76	0.77
550	0.88	0.90	1050	0.76	0.77

λ [nm]	R Air/Back sheet	R EVA/Back sheet	λ [nm]	R Air/Back sheet	R EVA/Back sheet
560	0.88	0.90	1060	0.76	0.77
570	0.87	0.90	1070	0.76	0.77
580	0.87	0.90	1080	0.76	0.77
590	0.87	0.89	1090	0.75	0.77
600	0.87	0.89	1100	0.75	0.76
610	0.86	0.89	1110	0.74	0.76
620	0.86	0.88	1120	0.72	0.74
630	0.86	0.88	1130	0.71	0.73
640	0.86	0.88	1140	0.72	0.73
650	0.86	0.88	1150	0.71	0.72
660	0.85	0.87	1160	0.71	0.70
670	0.85	0.87	1170	0.69	0.68
680	0.85	0.87	1180	0.68	0.67
690	0.84	0.86	1190	0.67	0.65
700	0.85	0.87	1200	0.65	0.62
710	0.84	0.86			
720	0.84	0.86			
730	0.84	0.86			
740	0.84	0.86			
750	0.84	0.85			
760	0.83	0.85			
770	0.83	0.85			
780	0.83	0.85			
790	0.83	0.85			

Publications

Journal publications

Hendrik Holst, Matthias Winter, Malte R. Vogt, Karsten Bothe, Marc Köntges, Rolf Brendel, and Pietro P. Altermatt: *Application of a new ray tracing framework to the analysis of extended regions in Si solar cell modules.* Energy Procedia (2013), vol. 38: pp. 86-93.

Matthias Winter, Hendrik Holst, Malte R. Vogt and Pietro P. Altermatt: *Combining structures on different length scales in ray tracing: Analysis of optical losses in solar cell modules.* Optical and Quantum Electronics (2015), vol. 47(6): pp. 1373-1379.

Malte R. Vogt, Hendrik Holst, Matthias Winter, Rolf Brendel, and Pietro P. Altermatt: *Numerical modeling of c-Si PV modules by coupling the semiconductor with the thermal conduction, convection and radiation equations.* Energy Procedia (2015), vol. 77: pp. 215-224.

Carsten Schinke, Christian P. Peest, Jan Schmidt, Rolf Brendel, Karsten Bothe, Malte R. Vogt, Ingo Kröger, Stefan Winter, Alfred Schirmacher, Siew Lim, Hieu T. Nguyen and Daniel MacDonald: *Experimental Determination of the Uncertainty of the Absorption Coefficient of Crystalline Silicon.* Energy Procedia (2015), vol. 77: pp. 170-178.

Carsten Schinke, Christian P. Peest, Jan Schmidt, Rolf Brendel, Karsten Bothe, Malte R. Vogt, Ingo Kröger, Stefan Winter, Alfred Schirmacher, Siew Lim, Hieu T. Nguyen and Daniel MacDonald: *Uncertainty analysis for the coefficient of band-to-band absorption of crystalline silicon.* AIP Advances (2015), vol. 5(6): pp. 067168.

Malte R. Vogt, Harald Hahn, Hendrik Holst, Matthias Winter, Carsten Schinke, Rolf Brendel, and Pietro P. Altermatt: *Measurement of the optical constants of soda-lime glasses in dependence of iron content , and modeling of iron-related power losses in crystalline Si solar cell modules.* IEEE J. Photovolt. (2015), no.99: pp.1-8.

Robert Witteck, David Hinken, Malte R. Vogt, Jens Müller, Susanne Blankemeyer, Henning Schulte-Huxel, Karsten Bothe and Rolf Brendel: *Simulation of optimized cell interconnection for PERC-modules.* IEEE J. Photovolt. (2015), to be published.

Proceedings of international conferences

Malte R. Vogt, Pietro P. Altermatt and Rolf Brendel: *Optimization of metallic nanoparticles for plasmon-enhanced scattering at the rear of c-Si solar cells.* Proc. 27th EUPVSEC (2012), Frankfurt, Germany, pp. 86-88.

Matthias Winter, Hendrik Holst, Malte R. Vogt and Pietro P. Altermatt: *Combining structures on different length scales in ray tracing: Analysis of optical losses in solar cell modules.* Proc. 14th NUSOD (2014), Mallorca, Spain, pp. 167-168.

Malte R. Vogt, Hendrik Holst, Matthias Winter, Sebmen Knoc, Andrea Ruppenthal, Marc Köntges, Rolf Brendel, and Pietro P. Altermatt: *Optical loss analysis of colored PV modules.* Proc. 6th WCPEC (2014), Kyoto, Japan, pp. 1115-1116.

Matthias Winter, Hendrik Holst, Malte R. Vogt and Pietro P. Altermatt: *Impact of realistic illumination on optical losses in Si solar cell modules compared to standard testing conditions.* 31th EUPVSEC (2015), Hamburg, Germany, accepted for Oral presentation.

Curriculum Vitae

Name	**Malte Ruben Vogt**
Birth	November 7, 1986 in Langenhagen, Germany

University Studies

10/2006 - present	Leibniz Universität Hannover (LUH)
10/2011	Master of Science in physics
	Master thesis: 'Simulation of plasmonic nanoparticles at the rear side of Si solar cells'
10/2011	Bachelor of Science in physics
	Bachelor thesis: 'Investigation of a heterodyne polarizing interferometer for spaceborne missions'

School

06/2006	Abitur, IGS Mühlenberg (Hannover, Germany)
06/2004	High School Diploma, Redlands East Valley High School (USA, CA)

Work

12/2011 - present	Research fellow at Institute for Solar Energy Research Hamelin (ISFH) and LUH

Acknowledgments